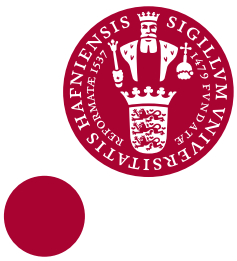

High Intrarenal Lactate Production Inhibits the Renal Pseudohypoxic Response to Acutely Induced Hypoxia in Diabetes

Laustsen, Christoffer; Lipsø, Kasper; Østergaard, Jakob Appel; Nielsen, Per Mose; Bertelsen, Lotte Bonde; Flyvbjerg, Allan; Pedersen, Michael; Palm, Fredrik; Ardenkjær-Larsen, Jan Henrik

Published in:
Tomography

DOI:
10.18383/j.tom.2019.00003

Publication date:
2019

Document version
Publisher's PDF, also known as Version of record

TOMOGRAPHY®

WWW.TOMOGRAPHY.ORG | VOLUME 5 NUMBER 2 | JUNE 2019

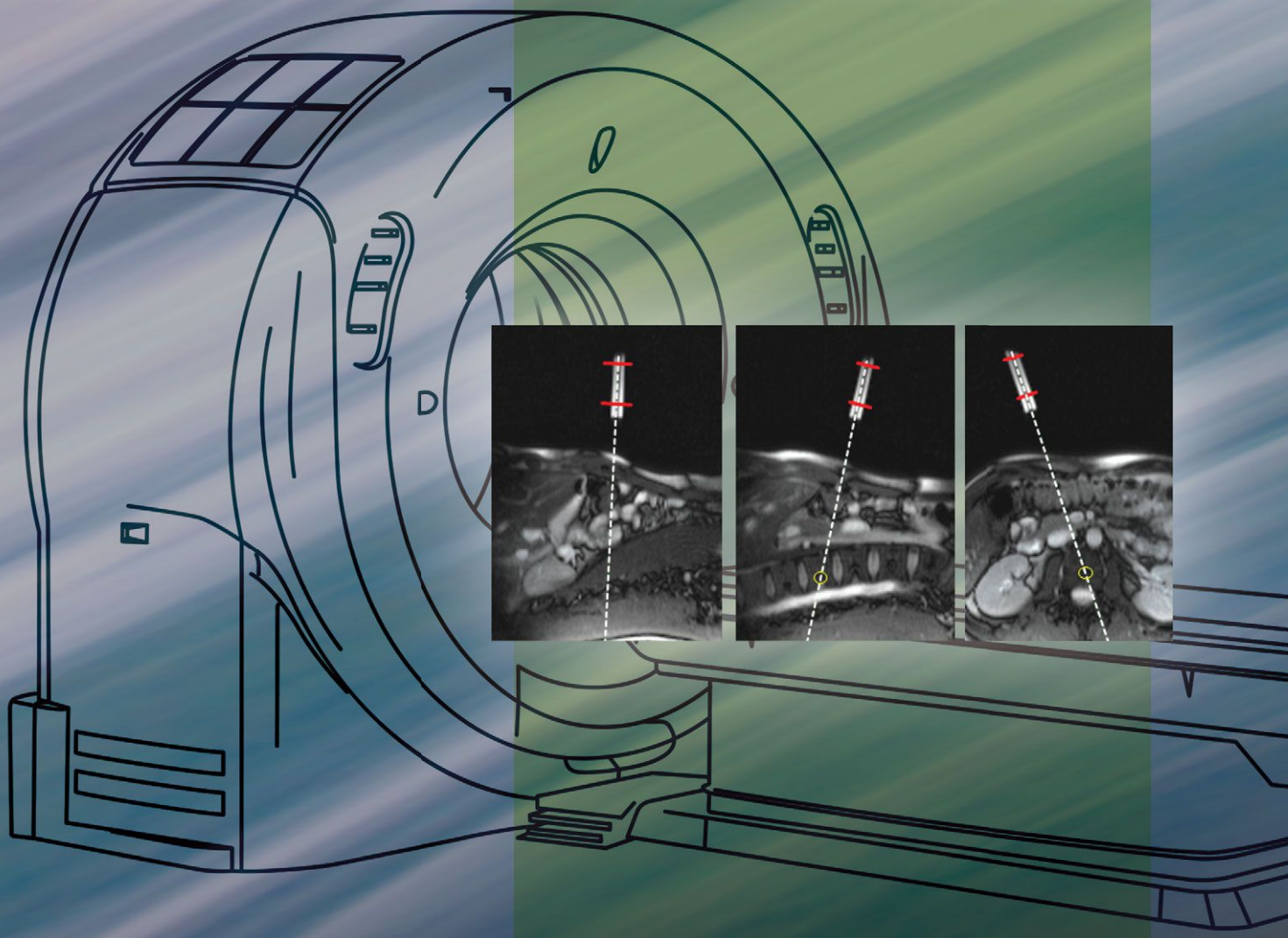

MR-guided needle intervention

GRAPHO

MR SOLUTIONS

Imaging INNOVATION

The Future of Preclinical Imaging

The next generation of superconducting 7T, 4.7T and 3T cryogen free MRI.

- Up to 12 hour power protection
- No quenching due to power loss
- No cooling water required
- 1500 mT/m gradients

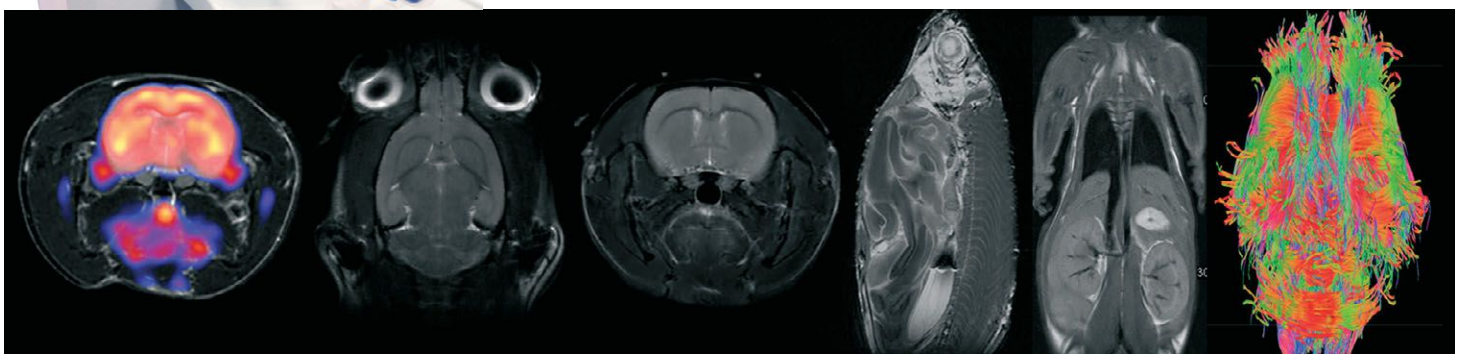

Multi-modality Imaging

PET/MR
Simultaneous & sequential acquisition of PET & MR
MRS-PET

SPECT/MR
Sequential & simultaneous acquisition of SPECT & MR
MRS-SPECT

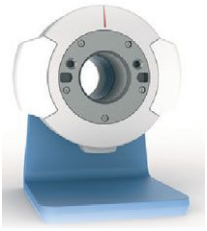

Upgrades
Bring your MRI back to life
MRS Upgrade

Clinical Kit
Clinical to preclinical conversion kit
C2P

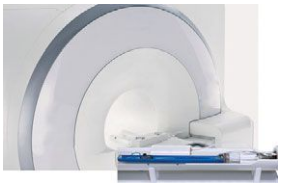

Confocal
In vivo optical imaging
MRS CellLIVE

For more information contact us at:
information@mrsolutions.com
www.mrsolutions.com

TOMOGRAPHY®
AN INTERNATIONAL JOURNAL FOR IMAGING RESEARCH

Tomography® is published quarterly. Tomography publishes basic (technical and pre-clinical) and clinical scientific articles which involve the advancement of imaging technologies. Tomography encompasses studies that use single or multiple imaging modalities including for example CT, US, PET, SPECT, MR and hyperpolarization technologies, as well as optical modalities (i.e. bioluminescence, photoacoustic, endomicroscopy, fiber optic imaging and optical computed tomography) in basic sciences, engineering, preclinical and clinical medicine. Tomography also welcomes studies involving exploration and refinement of contrast mechanisms and image-derived metrics within and across modalities toward the development of novel imaging probes for image-based feedback and intervention. The use of imaging in biology and medicine provides unparalleled opportunities to noninvasively interrogate tissues to obtain real-time dynamic and quantitative information required for diagnosis and response to interventions and to follow evolving pathological conditions. As multi-modal studies and the complexities of imaging technologies themselves are ever increasing to provide advanced information to scientists and clinicians, Tomography provides a unique publication venue allowing investigators the opportunity to more precisely communicate integrated findings related to the diverse and heterogeneous features associated with underlying anatomical, physiological, functional, metabolic and molecular genetic activities of normal and diseased tissue. Thus Tomography publishes peer-reviewed articles which involve the broad use of imaging of any tissue and disease type including both preclinical and clinical investigations. In addition, hardware/software along with chemical and molecular probe advances are welcome as they are deemed to significantly contribute towards the long-term goal of improving the overall impact of imaging on scientific and clinical discovery. Tomography provides a comprehensive venue for integration of imaging modalities to address biologically important and clinically relevant questions in order to facilitate more rapid and seamless scientific and clinical advancements. Analysis of simultaneous multidimensional (e.g. content, space and time) and multivariate computational data extraction of features which support unique identification of different pathologic tissue phenotypes for advancing imaging is welcomed by Tomography. Types of articles include regular Research Articles, Brief Reports, Reviews, Image Reports and Consensus Papers sponsored from national meetings or government funding agencies.

This journal is available on-line and can be accessed at www.Tomography.org. The journal is an Open Access journal and can be freely downloaded for personal use.

Publication Information: Tomography (ISSN: 2379-1381) is published quarterly by Grapho Publications, 3000 Green Road, #131281, Ann Arbor, MI 48105, USA. Periodicals postage paid at Ann Arbor, MI and additional mailing offices.

USA POSTMASTER: Send address changes to Tomography, Grapho Publications, Customer Service Department, 3000 Green Road, #131281, Ann Arbor, MI 48105, USA.

Advertising Information: Advertising and classified advertising orders and inquiries can be sent to: e-mail: info@tomography.org.

Guide for Authors: For a full and complete Guide for Authors, please go to: http://www.tomography.org.
Author Inquiries: For inquiries relating to the submission of articles (including electronic submission) please visit this journal's homepage at http://www.tomography.org.
Contact details for questions arising after acceptance of an article, including those relating to proofs, will be provided by the publisher.


The paper meets the requirements of ANSI/NISO Z39.48-1992 (Permanence of Paper).

Reprints: To order reprints for educational, commercial, or promotional use, contact Cadmus Reprints, P.O. Box 822942, Philadelphia, PA 19182-2942; E-mail: cjsreprints@cadmus.com; Phone: 866-487-5625; FAX: 877-705-1373

Funding Body Agreements and Policies: Grapho Publications has established agreements and policies to allow authors whose articles appear in journals published by Grapho Publications, to comply with potential manuscript archiving requirements as specified as conditions of their grant awards. Tomography is an open access journal which complies with NIH funding guidelines and all articles can be archived by authors in PubMed Central http://www.nihms.nih.gov or other international data bases to be in compliance with granting agency requirements.

Notice: No responsibility is assumed by the Publisher for any injury and/or damage to persons or property as a matter of products liability, negligence or otherwise, or from any use or operation of any methods, products, instructions or ideas contained in the material herein. Because of rapid advances in the medical sciences, in particular, independent verification of diagnoses and drug dosages should be made. Although all advertising material is expected to conform to ethical (medical) standards, inclusion in this publication does not constitute a guarantee or endorsement of the quality or value of such product or of the claims made of it by its manufacturer.

Orders, Claims, and Journal Inquiries: Please contact the Grapho Publications Customer Service Department, Grapho Publications, 3000 Green Road, #131281, Ann Arbor, MI 48105, USA; phone: (+1) 734-221-0126 e-mail: info@tomography.org.

TOMOGRAPHY.ORG
VOLUME 5 NUMBER 2
JUNE 2019

TOMOGRAPHY®
AN INTERNATIONAL JOURNAL FOR IMAGING RESEARCH

COVER ILLUSTRATION

Andreas Reichert and colleagues report the development of GantryMate, a modular MR-compatible image-guided needle intervention assistance system.

The Analysis & Collaboration Platform for Data-Intensive Research

Make your data & algorithms accessible, shareable, & reproducible.

INCREASED UTILIZATION

Easy to implement on-premise or in the cloud. Easy to use for all researchers.

FAST LANE TO DISCOVERY

Free up your time to do research, not IT.

FUNDED TO PUBLISHED

Simplify your processes from receiving funding to publishing your reproducibile data.

FLYWHEEL

Request a demo at flywheel.io

@Flywheel_io

Regional Ultrahigh-Resolution Rescan in a Clinical Whole-Body CT Scanner Using a Contact Detector Insert

Thomas C. Larsen[1], Eric E. Bennett[1], Dumitru Mazilu[1], Marcus Y. Chen[2], and Han Wen[1]

[1]Imaging Physics Laboratory, Biochemistry and Biophysics Center and [2]Cardiovascular Branch, National Heart, Lung and Blood Institute, National Institutes of Health, Bethesda, MA

Corresponding Author:
Han Wen, PhD
Imaging Physics Laboratory, Biochemistry and Biophysics Center, National Heart, Lung and Blood Institute, NIH, Bethesda, MD 20892-1061;
E-mail: wenh@nhlbi.nih.gov

Key Words: CT re-scan, ultrahigh resolution, ultralow dose, contact detector insert, tomosynthesis, hybrid CT

Abbreviations: Computed tomography (CT), contact detector inserts (CDIs), high-resolution CT (HRCT), axial HRCT (a-HRCT)

ABSTRACT

Ultrahigh-resolution, low-dose rescans in a region of interest following a general screening computed tomography (CT) scan is motivated by the need to reduce invasive tissue biopsy procedures in cancer screening. We describe a new method to meet the conflicting demands of ultrahigh resolution, high-speed and ultralow-dose, and the first proof-of-concept experiment. With improving detector resolution, the limiting factor for the system resolution of whole-body CT scanners shifts to the penumbra of the source focal spot. The penumbra unsharpness is minimized by inserting flat-panel detector(s) that are in direct contact with the body. In the hybrid system, the detector insert and the CT detector acquire data simultaneously, whereby the standard CT images give the position and orientation of the detector insert(s) as needed for tomosynthesis reconstruction. Imaging tests were performed with a compact photon-counting detector insert on resolution targets of both high- and low-contrast as well as a mouse specimen, all inside a body phantom. Detector insert tomosynthesis provided twice the resolution of the CT scanner alone at the same dose concentration. The short 2-cm beam collimation of the tomosynthesis rescan gave an effective dose equivalent to 6% of an average CT scan in the chest or abdomen.

INTRODUCTION

Driven by the desire to reduce invasive biopsy procedures in cancer screening, technologies are being rapidly developed to provide ultrahigh resolution in a limited region of interest, which allows a detailed rescan of a suspect area revealed by a standard scan while the patient is still in the computed tomography (CT) scanner (1-3). The CT system resolution is influenced by the detector resolution, the size of the x-ray tube focal spot and the local dose concentration (CTDIvol). To realize a high-resolution rescan in standard whole-body CT scanners, protocols have been developed to increase the CTDIvol by multiple fold in a short Z length to provide high-resolution locally (3); further improvement comes with the recent implementation of ultrahigh-resolution multirole detectors in whole-body CT scanners (1) and high-resolution photon-counting detectors (2). With such detectors, the limiting factor of resolution becomes the focal spot penumbra, namely, blurring of the images by the finite size of the x-ray source spot. One approach to overcome the focal spot limit is a system design that includes a micro focus source on an inner ring inside the scanner bore. But it has yet to be realized owing to major engineering changes to the CT system.

On the other hand, because the focal spot penumbra is proportional to the distance between the object and the image plane, contact radiography and mammography minimize the distance to achieve excellent resolution with relatively large focal spots. Based on this idea, we describe an alternative method to break the focal spot limitation in clinical whole-body CT scanners, and the first experimental demonstration. The general idea is to add detector inserts inside the CT bore which are in direct contact with the body, for example, on the patient bed (Figure 1A). In this configuration, the focal spot penumbra on the detector insert is reduced by several fold when compared to the existing CT detector in the rotating gantry (Figure 1B). In operation, the detector inserts are mechanically shifted out of view during the standard CT scan, and shifted into the bore for the high-resolution rescan. A unique synergy of this hybrid system is the simultaneous data acquisition by the detector insert and the CT detector during the high-resolution rescan: images from the CT detector show the position and orientation of the detector insert inside the bore, which is necessary information for the tomosynthesis reconstruction of the data collected by the Detector Insert.

ISSN 2379-1381 https://doi.org/10.18383/j.tom.2019.00002

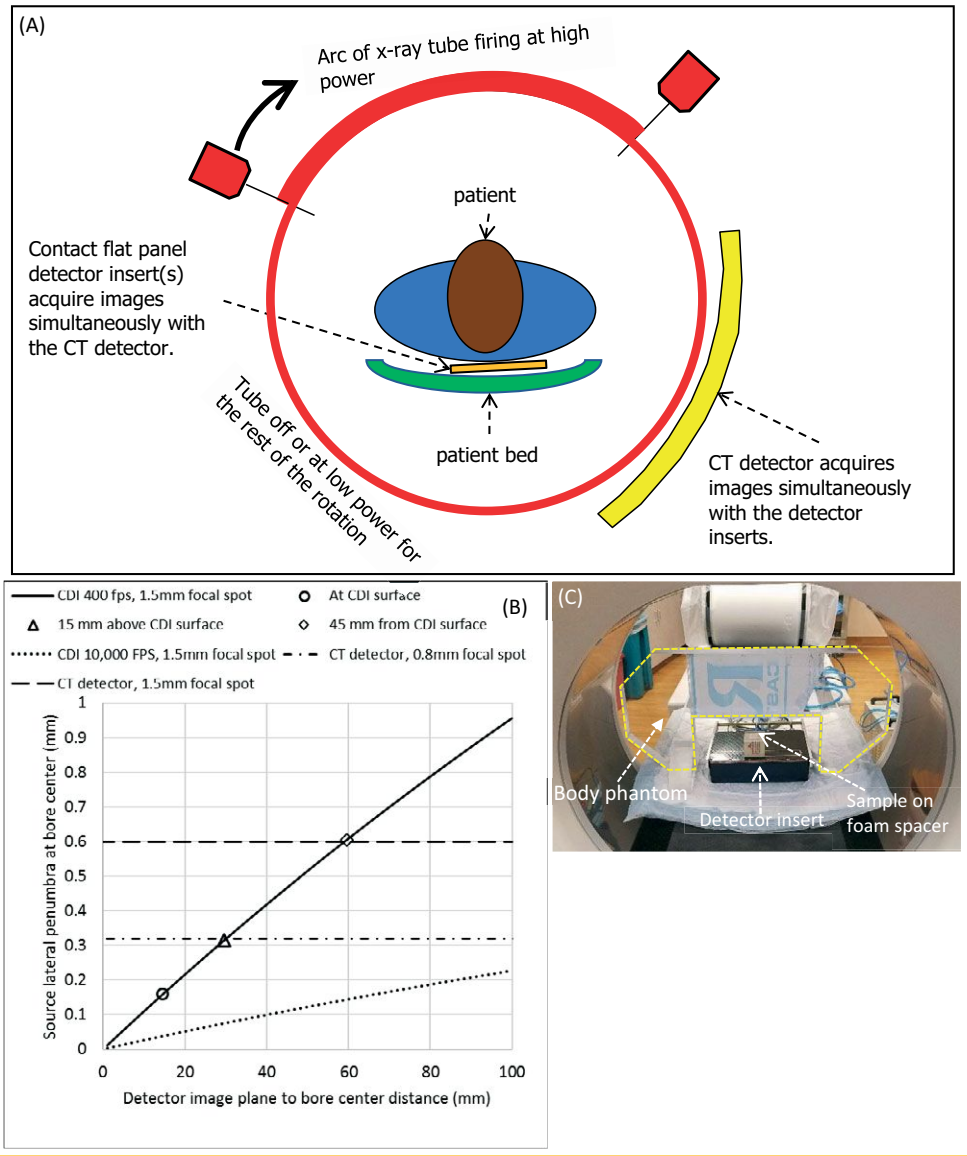

Figure 1. Concept of the contact detector insert (CDI) and experimental setup. In the schematic of a hybrid computed tomography (CT) system, the x-ray tube is switched on over part of the gantry rotation for tomosythesis by the CDI. The CT detector simultaneously acquires data to provide positional information of the CDI (A). Estimated x-ray tube focal spot penumbras at the bore center for the CDI and the CT detector, for the Toshiba Aquilion One Genesis scanner, accounting for gantry rotation (B). The circle, triangle and diamond mark actual experiments. Dotted line is for a hypothetical high-speed detector insert. Dashed line is for the detector of the CT scanner operating at high-power/large focal spot mode. Dash-dotted line is for the CT scanner operating at low-power/small focal spot mode, which is the mode that provided the best resolution in standard HRCT scans. The experimental setup includes an acrylic body phantom outlined in dashed line, the photon-counting detector insert, and various resolution phantoms and samples (C).

The method was tested in a clinical whole-body CT scanner (Figure 1C). The detector insert was a flat-panel photon-counting detector placed on the patient bed. An acrylic body phantom that simulated the attenuation of an adult torso was used in all imaging tests to provide realistic signal levels. Images of resolution targets inside the body phantom resolved 0.2-mm-diameter holes in a square matrix of 0.4-mm pitch in a 0.30-second scan, in comparison to the 0.5-mm holes/1.0-mm pitch by the CT scanner alone at the same dose concentration CTDIvol in a 0.6-second scan. Images of a mouse specimen inside the body phantom were also compared.

Regarding the limitations of this approach, a technical bottleneck is the 400 FPS imaging speed of the flat-panel photon-counting detector, which is $<1/20$th the speed of a clinical CT detector. It meant that image blurring in the lateral direction is dominated by the movement of the x-ray focal spot. This is because as the gantry rotates, the travel distance of the focal spot during the acquisition of a single projection image is several times the size of the spot. This point was verified experimentally. Other limitations are inherent to tomosynthesis, including out-of-plane shadowing artifacts, an-isotropic image resolution, and lack of a measure of the absolute CT density in Hounsfield units.

Looking into the future, while clinical whole-body CT scanners continually achieve smaller focal spot size and better detector resolution, focal spot size penumbra continues to be a limiting factor in system resolution. For example, the latest photon-counting detectors provide resolutions better than 50 μm (4), while the progress of focal spot size lags behind, reaching 0.4–0.5 mm, currently at low power settings (https://www.itnonline.com/content/canon-medical-systems-aquilion-precision-ct-receives-fda-clearance). Therefore, contact detector inserts (CDIs) should continue to provide an extra boost of resolution in a targeted rescan of a region of interest in future whole-body scanners. Future development directions include more sophisticated and customized image reconstruction methods for the tomosynthesis rescan, and faster photon-counting detector inserts to reduce blurring

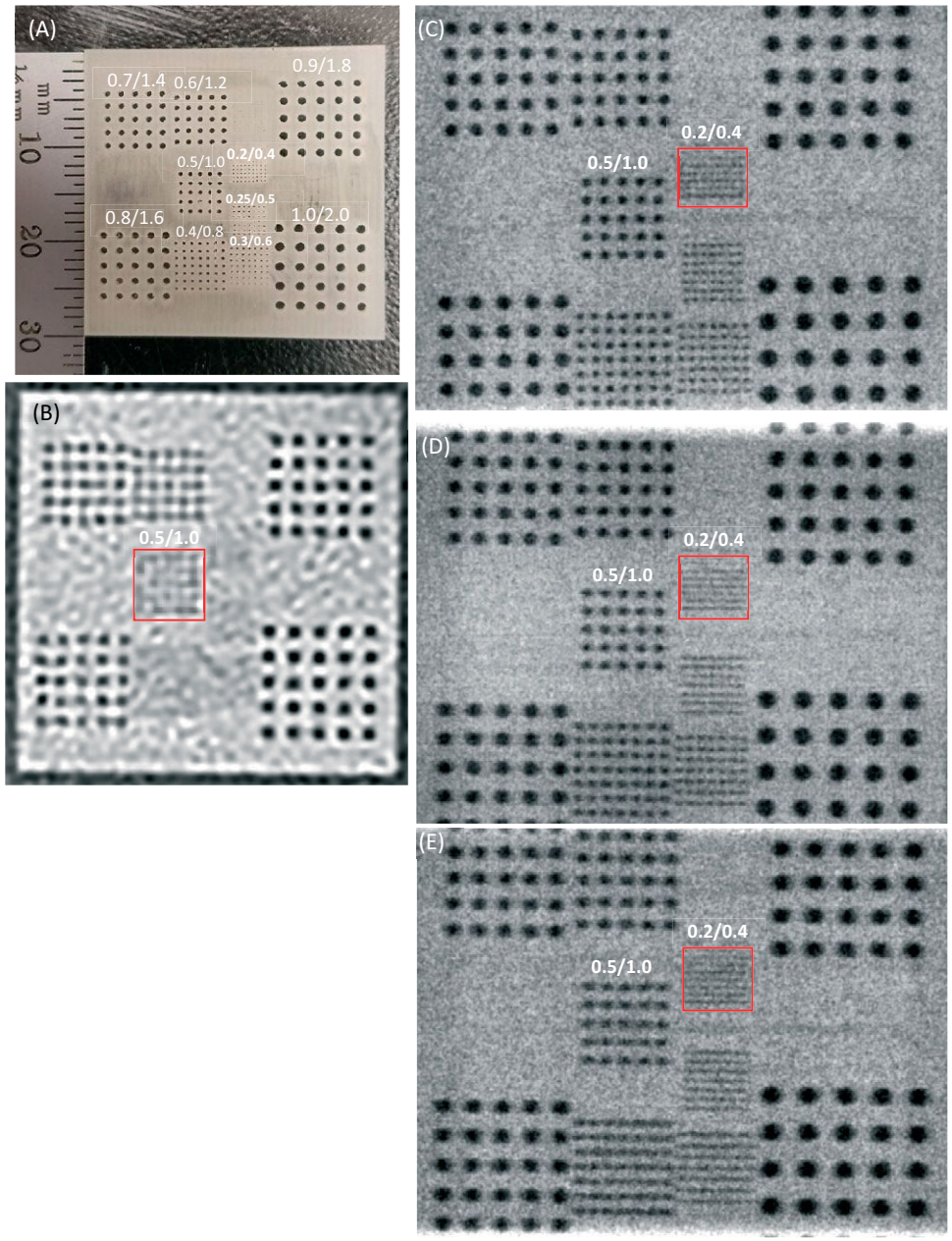

Figure 2. Comparison of the CT image and CDI tomosynthesis images of a resolution card, taken at the same CTDIvol inside the body phantom. The tomosynthesis images were taken at various sample-to-detector distances. A picture of the 3D printed resolution card of 1.0 mm of thickness, consisting of matrices of air holes (A). The labels denote the hole diameter/center-to-center spacing of the hole matrices. The CT scan resolved the 0.5-mm hole matrix (red box) (B). The CDI tomosythesis scan resolved the 0.2-mm hole matrix (red box) when the card was place on the surface of the detector (15 mm from the image plane within the detector) (C). When the resolution card was elevated to 15 mm above the detector surface (30 mm from the image plane) with a foam spacer, the CDI image was blurred in the horizontal direction due to focal spot travel over the image acquisition time, and resolved only the 0.2-mm hole matrix vertically (red box) (D). The resolution card was further elevated to 45 mm above the detector surface (60 mm from the image plane), and further horizontal blurring was seen due to focal spot travel (E).

due to gantry rotation. These will be elaborated in the Discussion section.

METHODOLOGY

The body phantom was made of solid acrylic (Figure 1C). It provided a ≥15-cm path length of attenuation through the acrylic material for all scans to simulate that of an adult body.

Two resolution phantoms were imaged inside the body phantom (Figure 1C). The first was a 3D printed polymer card of 1 mm thickness (Figure 2A) that contained matrices of air holes of decreasing diameter and increasing density. The CT attenuation coefficient of the polymer material was 130 HU at 120 kV. The second, a low-contrast card, was also 3D printed to the same dimensions, but with the holes filled with wax. The CT attenuation coefficient of the wax was −105 HU, or a 235 HU contrast from the surrounding polymer.

A mouse specimen was also imaged. The specimen was fixed in 10% formalin in a centrifuge tube, and the tube was placed horizontally on the surface of the detector insert, inside the body phantom.

Both the CDI tomosynthesis scan and the high-resolution CT scan used the axial (cone beam) mode of the scanner with a static patient bed, to provide the highest dose concentration for a given beam collimation and scan time, which maximizes the signal-to-noise ratio (3).

The contact detector insert was a photon-counting detector (Xcounter Thor Model, Direct Conversion AB, Danderyd, Sweden) of 256 × 2048 pixel matrix and 0.1-mm pixel pitch, 400 frames/s acquisition rate in a 16-bit mode, and single energy threshold of 25 keV. The CT scanner parameters for the tomosynthesis scan were axial (cone beam) mode 120 kV/700 mA (large focal spot mode), 1.5 s/turn rotation speed, data acquisition over the top 72° arc of

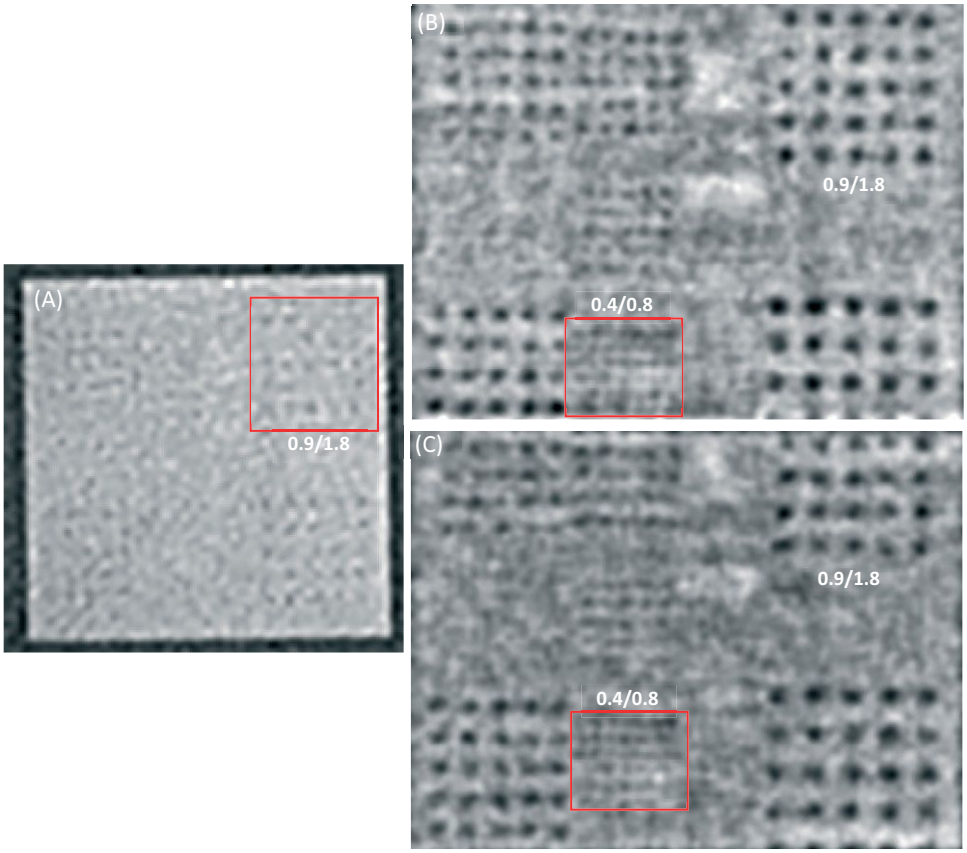

Figure 3. Comparing CT and CDI tomosynthesis images of a low-contrast resolution card acquired at the same CTDIvol inside the body phantom. The phantom was a 1.0-mm-thick 3D printed polymer card with an identical pattern to the card in Figure 2, but with the holes filled with wax to provide a 235 HU contrast between the polymer and the wax. The CT image detected some of the 0.9-mm diameter holes (red box). The label is hole diameter/center-to-center spacing (A). The CDI tomosynthesis image resolved the 0.4-mm hole array (red box) when the card was placed on the surface of the detector (sample-to-image distance of 15 mm) (B). In the CDI tomosynthesis image of the card which was placed at 45 mm above the detector surface with a foam spacer (sample-to-image distance of 60 mm), the same resolution was retained (C).

gantry rotation in 0.3 seconds and 210 mAs, beam collimation of 2 cm and CTDIvol of 15.2 mGy. The image plane within the detector, which is the semiconductor conversion layer, lies at 14.6 mm below the surface of the detector. The resolution cards were placed either directly on the surface of the detector, corresponding to a distance of 14.6 mm to the image plane, or on 15- and 45-mm-thick foam spacers, corresponding to a distance of 29.6 mm and 59.6 mm to the image plane. A basic filtered back-projection tomosynthesis image reconstruction was used to reconstruct images at 0.05-mm pixel size at various depths from the surface of the detector.

For the axial high-resolution CT (HRCT) image acquisition, the CDI was removed. The resolution cards were positioned in the axial plane inside the body phantom for best resolution. The mouse sample was placed directly on the bed of the scanner. All samples were positioned at the isocenter of the bore. Scan parameters were axial cone beam mode of 120 kV/350 mA (small focal spot mode) and 210 mAs (0.6 seconds of rotation time), beam collimation of 20 × 0.5 mm (3), and CTDIvol of 15.2 mGy. Images were reconstructed with the FC52 kernel, in-plane pixel size of 0.25 mm, slice center-to-center spacing of 0.25 mm, and slice thickness of 0.5 mm. This reconstruction setting was found to provide the best resolution.

RESULTS

Figure 2, B–E compares the axial HRCT (a-HRCT) and CDI tomosynthesis images of the high-contrast (1130 HU) resolution card inside the body phantom, which were acquired at the same dose concentration (CTDIvol). For the a-HRCT image (Figure 2B), the reconstruction pixel size of 0.25 mm was found visually to give the best resolution. The smallest resolved features were the matrix of 0.5 mm holes. The CDI tomosynthesis image of the resolution card resolved the 0.2-mm hole matrix when the card was placed directly on the detector (Figure 2C). When the card was placed at 15 mm and 45 mm above the detector surface, CDI tomosynthesis could only resolve the 0.2-mm holes vertically while they were horizontally burred (Figure 2, D and E). This was caused by the 6.3-mm travel of the x-ray focal spot over the acquisition time per frame, which led to a growing lateral penumbra of the focal spot with increasing distance from the detector, as illustrated in Figure 1B.

Figure 3 compares the a-HRCT and CDI tomosynthesis images of the low-contrast (235 HU) resolution card at the same CTDIvol level. The a-HRCT image showed some of the 0.9-mm wax dots (Figure 3A); the CDI tomosynthesis images resolved the matrix of 0.4-mm wax dots (Figure 3B) when the card was placed on the detector surface or elevated at 45 mm from the surface.

Figure 4 compares the a-HRCT and CDI tomosynthesis images of the mouse specimen, again at the same dose concentration level. Two different horizontal sections are shown. The CDI image resolved the bone structures at higher resolution such as the individual ribs, and also visualized structures in the nose and head and the abdominal cavity which were not visible by a-HRCT.

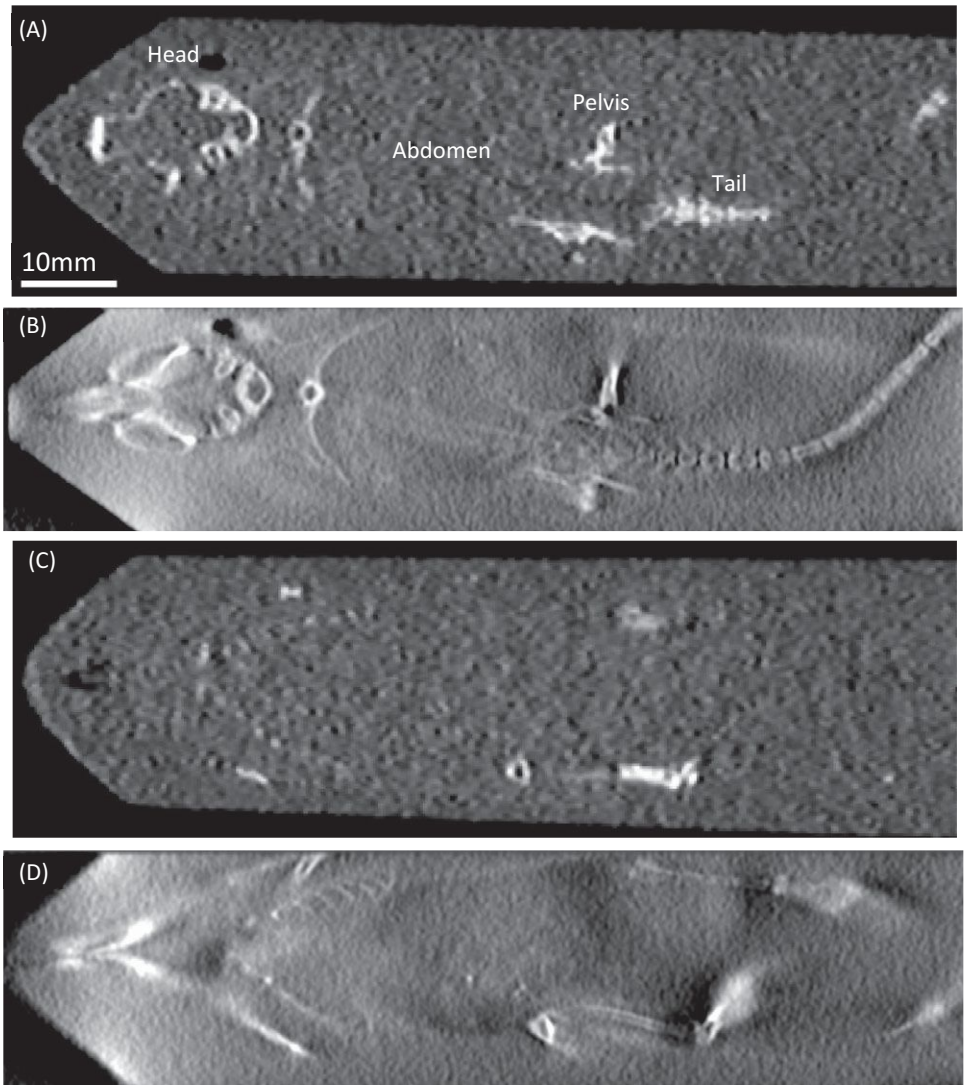

Figure 4. Comparing CT and CDI tomosythesis images of a formalin-fixed mouse specimen placed in the body phantom. The specimen is fixed in formalin in a centrifuge tube. The same CTDIvol of 15.2 mGy was used. (A) and (C) are CT scan coronal sections. (B) and (D) are the CDI images of the same locations. The resolution of the bone structures is higher in the CDI images; structures in the nose and head and the abdominal cavity become visible in the CDI images.

DISCUSSION

As a first test, this study shows that a contact detector insert in a whole-body CT scanner achieves ultrahigh resolution in a 0.3-second scan under a realistic level of attenuation by an adult body, in a zone near the detector. The depth of the zone is currently limited by the frame rate of the detector. The principle for high resolution is similar to that of contact radiography, and the concept in general is similar to surface coils in body MRI, which provide high sensitivity and resolution near the coils. When comparing the results of the high- versus low-contrast resolution cards in the presence of the body phantom attenuation, it was clear that the resolution decreases with lower contrast, although the CDI tomosynthesis scan maintains a factor of two resolution relative to the CT scanner itself at the same dose.

For comparison, a recent Toshiba Aquilion family CT scanner has an ultrahigh resolution mode of 0.25-mm pixel pitch at the bore center, which was shown to resolve 0.12-mm-wide slits (1). However, this was shown in a resolution target alone without the attenuation of a body phantom, and at 2.4 times the dose concentration of this study (CTDIvol of 36.6 mGy vs 15.2 mGy). More significantly, it required low power output of the x-ray tube to maintain a smaller focal spot size, leading to scan times of several seconds compared to the 0.3-second scan of this study. Scan time is a significant factor for ultrahigh resolution, as subtle motion and drift of the body blur the images over time. Radiation dose is also a significant factor for rescans, as it adds dose onto the standard scan. Using the dose-length-product (DLP = 30.3 mGy*cm) reported by the scanner in this study, we estimate that the added effective dose of the CDI tomosynthesis rescan in the chest and abdomen to be 0.42 mSv and 0.45 mSv on average (5), which is equivalent to 6% of a standard chest or abdomen CT scan (https://www.radiologyinfo.org/en/info.cfm?pg=safety-xray). This level of added dose should not impose significant burden on the patient, and it should also allow rescans of several regions in certain cases. The weakness of the CDI method, as mentioned in the Introduction section, involves inherent limitations of tomosynthesis, including out-of-plane shadows, anisotropic resolution, and lack of absolute CT density measurements.

The mass of the body phantom was mostly on 3 sides of the resolution targets to simulate the position of the body above the contact detector insert. This asymmetric disposition did not have adverse effects on the image quality of the standard CT scans as long as the resolution targets were positioned at the center of the bore: the same image quality and resolution were attained when

compared with the same a-HRCT scans on a standard body phantom with resolution inserts from a previous study (3).

Further developments are envisioned in both hardware and software. For software, this study used basic reconstruction procedures without any artifact reduction measures. A significant part of the on-going work is the improvement of the reconstruction methods in both algorithms and computation speed. Advanced tomosynthesis reconstruction methods that are being developed for other applications such as digital breast tomosynthesis [see reference (7) for a review] may be considered to see whether they are suitable for this application. Depending on the location of the region of interest within the body for the rescan, the influence of strongly attenuating structures such as bone and implanted devices may vary widely. Therefore, the reconstruction method and the placement of the contact detector insert should be adaptable to the location of the rescan.

For hardware, multiple detectors can be inserted to conform to the surface of the body for optimal coverage of a targeted internal region or several regions. The speed of compact photon-counting detectors is improving and can be expected to match that of CT detectors in a few years, thereby increasing the depth of the high-resolution zone as illustrated by the dotted line in Figure 1B of a hypothetical detector insert of 10,000 fps speed. A recent development is flexible x-ray detectors of high sensitivity using hybrid organic–inorganic materials (6), which may lead to contact detector inserts that can bend and conform to the shape of the body, much like the surface coils of MRI scanners. Whether using multiple detectors or bendable detectors, the exact geometry of the detector inserts during each scan need to be determined for tomosynthesis reconstruction. Therefore, the simultaneous image acquisition by the CT scanner itself becomes indispensable for this purpose.

ACKNOWLEDGMENTS

We are grateful to Joel Moss of NHLBI for discussions, to Shirley Rollison and Xi Tao of NHLBI for their assistance with the scans, and to the NHLBI Animal Surgery and Resource Core for the specimen. We are grateful to Christer Ullberg and Hamdan Amin of Xcounter for their assistance with the detector insert. This work is supported by the Intramural Research Program of NIH, National Heart, Lung, and Blood Institute.

Disclosures: Han Wen is the inventor of a patent application for this technology by the National Institutes of Health.

Conflict of Interest: The authors have no conflict of interest to declare.

REFERENCES

1. Kakinuma R, Moriyama N, Muramatsu Y, Gomi S, Suzuki M, Nagasawa H, Kusumoto M, Aso T, Muramatsu Y, Tsuchida T, Tsuta K, Maeshima AM, Tochigi N, Watanabe S, Sugihara N, Tsukagoshi S, Saito Y, Kazama M, Ashizawa K, Awai K, Honda O, Ishikawa H, Koizumi N, Komoto D, Moriya H, Oda S, Oshiro Y, Yanagawa M, Tomiyama N, Asamura H. Ultra-high-resolution computed tomography of the lung: image quality of a prototype scanner. Plos One 2015;10:e0137165.
2. Pourmorteza A, Symons R, Henning A, Ulzheimer S, Bluemke DA. Dose efficiency of quarter-millimeter photon-counting computed tomography first-in-human results. Invest Radiol. 2018;53:365–372.
3. Larsen TC, Gopalakrishnan V, Yao JH, Nguyen CP, Moss J, Wen H. Optimization of a secondary VOI scan for lung imaging in a clinical CT scanner. J Appl Clin Med Phys. 2018;19:271–280.
4. Hosono R, Kawabata T, Hayashida K, Kudo T, Ozaki K, Teranishi N, Hatsui T, Hosoi T, Watanabe H, Shimura T. Advancement of X-ray radiography using microfocus X-ray source in conjunction with amplitude grating and SOI pixel detector, SOPHIAS. Opt Express. 2018;26:21044–21053.
5. Christner JA, Kofler JM, McCollough CH. Estimating effective dose for CT using dose-length product compared with using organ doses: consequences of adopting International Commission on Radiological Protection publication 103 or dual-energy scanning. AJR Am J Roentgenol. 2010;194:881–889.
6. Thirimanne HM, Jayawardena KDGI, Parnell AJ, Bandara RMI, Karalasingam A, Pani S, Huerdler JE, Lidzey DG, Tedde SF, Nisbet A, Mills CA, Silva SRP. High sensitivity organic inorganic hybrid X-ray detectors with direct transduction and broadband response. Nat Commun. 2018;9:2926.
7. Sechopoulos I. A review of breast tomosynthesis. Part II. Image reconstruction, processing and analysis, and advanced applications. Med Phys. 2013;40:014302.

High Intrarenal Lactate Production Inhibits the Renal Pseudohypoxic Response to Acutely Induced Hypoxia in Diabetes

Christoffer Laustsen[1], Kasper Lipsø[2,3], Jakob Appel Østergaard[4], Per Mose Nielsen[1], Lotte Bonde Bertelsen[1], Allan Flyvbjerg[5,6], Michael Pedersen[1], Fredrik Palm[7], and Jan Henrik Ardenkjær-Larsen[2,3,8]

[1]Department of Clinical Medicine, MR Research Centre, Aarhus University, Aarhus, Denmark; [2]Danish Research Centre for Magnetic Resonance, Copenhagen University Hospital Hvidovre, Hvidovre, Denmark; [3]Department of Electrical Engineering, Technical University of Denmark, Kgs Lyngby, Denmark; [4]Department of Endocrinology and Internal Medicine, Aarhus University Hospital, Aarhus, Denmark; [5]Steno Diabetes Center Copenhagen, The Capital Region of Denmark, Gentofte, Denmark; [6]University of Copenhagen, Copenhagen, Denmark; [7]Department of Medical Cell Biology, Uppsala University, Uppsala, Sweden; and [8]GE Healthcare, Copenhagen, Denmark

Corresponding Author:
Christoffer Laustsen, PhD
Aarhus University Hospital, MR Center, Palle Juul Jensens Boulevard.,
DK-8200 Aarhus N, Denmark;
E-mail: cl@clin.au.dk

Key Words: MRI, type 1-diabetes, kidney, renal metabolism, hyperpolarization
Abbreviations: Lactate dehydrogenase (LDH), pyruvate dehydrogenase (PDH), magnetic resonance imaging (MRI), blood oxygenation level–dependent (BOLD), magnetic resonance (MR), magnetic resonance spectroscopy (MRS), field of view (FOV), repetition time (TR), echo time (TE), chemical shift imaging (CSI)

ABSTRACT

Intrarenal hypoxia develops within a few days after the onset of insulinopenic diabetes in an experimental animal model (ie, a model of type-1 diabetes). Although diabetes-induced hypoxia results in increased renal lactate formation, mitochondrial function is well maintained, a condition commonly referred to as pseudohypoxia. However, the metabolic effects of significantly elevated lactate levels remain unclear. We therefore investigated in diabetic animals the response to acute intrarenal hypoxia in the presence of high renal lactate formation to delineate mechanistic pathways and compare these findings to healthy control animals. Hyperpolarized ^{13}C-MRI and blood oxygenation level–dependent ^{1}H-MRI was used to investigate the renal metabolism of [1-^{13}C]pyruvate and oxygenation following acutely altered oxygen content in the breathing gas in a streptozotocin rat model of type-1 diabetes with and without insulin treatment and compared with healthy control rats. The lactate signal in the diabetic kidney was reduced by 12%–16% during hypoxia in diabetic rats irrespective of insulin supplementation. In contrast, healthy controls displayed the well-known Pasteur effect manifested as a 10% increased lactate signal following reduction of oxygen in the inspired air. Reduced expression of the monocarboxyl transporter-4 may account for altered response to hypoxia in diabetes with a high intrarenal pyruvate-to-lactate conversion. Reduced intrarenal lactate formation in response to hypoxia in diabetes shows the existence of a different metabolic phenotype, which is independent of insulin, as insulin supplementation was unable to affect the pyruvate-to-lactate conversion in the diabetic kidney.

INTRODUCTION

In the diabetic kidney, hyperglycemia activates primarily mitochondrial uncoupling and secondarily the production of reactive oxygen species, which reduces energy production and creates hypoxia and an increased oxygen sensitivity in the kidney (1-5). Lactate dehydrogenase (LDH) and pyruvate dehydrogenase (PDH) are key enzymes in the pyruvate metabolism, thus facilitating pyruvate conversion to lactate or acetyl coenzyme A. Acetyl coenzyme A is the entry into Krebs cycle and follows the mitochondrial respiratory chain. An unchanged PDH activity indicates sufficient oxygen supply to the diabetic kidney, while hypoxia causes an elevated lactate pool and possibly a reduced PDH activity (1, 6, 7).

Magnetic resonance imaging (MRI) is considered an important functional imaging method for clinical decision-making in patients with renal disease (8-11), as well as in preclinical animal studies (12-15). Particularly important to assess the metabolic balance (PDH versus LDH) are the blood oxygenation level–dependent (BOLD) method and the metabolic imaging approach referred to as hyperpolarized ^{13}C-based magnetic resonance (MR) spectroscopy (5, 16-19). The combination of these 2 methods enables longitudinal assessment of oxygen availability in parallel with PDH ([1-^{13}C]pyruvate-to-^{13}C-bicarbonate conversion) and LDH ([1-^{13}C]pyruvate-to-[1-^{13}C]lactate conversion) flux estimation directly in the kidney tissue in vivo (5). Previous studies have shown high and unaltered pyruvate-to-lactate conversion in the early diabetic kidney (3, 5, 20-24). This pyruvate-to-lactate conversion has previously been correlated with the severity of diabetic renal complications toward diabetic nephropathy (25). Interestingly, diabetic rats with similar pyru-

ISSN 2379-1381 https://doi.org/10.18383/j.tom.2019.00003

Table 1. RT-PCR Primer Sequences

Gene	Forward Sequence	Reverse Sequence
Rat 18S	5′-CAT GGC CGT TCT TAG TTG-3′	5′-CAT GCC AGA GTC TCG TTC-3′
Rat PDH-A1	5′-TCC ACT CCT TGT AGC TGC AAC-3′	5′-GAG AAC CCA CCA CCC CAT G-3′
Rat LDH-A	5′-GCC ATG TAT TCC TTC CCT CA-3′	5′-GCC TCA TTG AAG ACC TGC TC-3′
Rat ALT	5′-GCC ATG TAT TCC TTC CCT CA-3′	5′-GCC TCA TTG AAG ACC TGC TC-3′
Rat MCT-1	5′-CTC TGG GCG CCG CGA GAT AC-3′	5′-CAA CTA CCA CCG CCC AGC CC-3′
Rat MCT-4	5′-CCA GGC CCA CGG CAG GTT TC-3′	5′-GCC ACC GTA GTC ACT GGC CG-3

vate-to-lactate conversion to healthy controls under normoxic conditions showed an increased pyruvate-to-lactate conversion following acute reduction in the respired oxygen content (3). Moreover, treatment with insulin increased the overall metabolic conversion (not sufficient to maintain good glycemic control), including increased pyruvate-to-lactate conversion (20). These discrepancies seem to suggest either a large variation in the streptozotocin model or potential distinct metabolic phenotypes. In this study, we investigated the metabolism of diabetic rats exhibiting increased pyruvate-to-lactate conversion compared with previous reports at similar time points and similar conditions (2 weeks of diabetes), although similar or even less pronounced diabetic complications and as such represent a naturally occurring phenotype or variation with unknown origin. We study the response to acutely altered oxygen supply [66% O_2, sufficient oxygen to ensure fully saturated blood versus 10% O_2, low oxygen content similar to previous report (3)], with and without insulin supplementation. We test the hypothesis that severe pseudohypoxia [highly elevated lactate-to-pyruvate ratio compared with controls and aforementioned previous reports at 2 weeks (3, 20)] is unable to compensate the lack of oxygen by increasing the intracellular lactate and thus is exhibiting an alternative metabolic phenotype.

METHODOLOGY

Animals and Study Protocol

Twenty-two 8-week-old female Wistar rats (N = 7–8/group; Taconic, Ry, Denmark) were included in this study. The rats were kept in cages with a 12:12-h light–dark cycle, temperature of 21°C ± 2°C and a humidity of 55% ± 5%. Diabetes was induced by an intravenous injection of freshly prepared streptozotocin (55 mg/kg body weight; Sigma-Aldrich, St. Louis, MO) dissolved in 10 mmol/L cold citrate buffer (pH 4.5). Blood glucose was measured in tail capillary blood with a Contour blood glucose meter (Bayer Diabetes Care, Copenhagen, Denmark). Rats were considered diabetic when the blood glucose levels exceeded 15 mmol/L at 48 h after injection of streptozotocin. The rats were divided into a diabetes group and treated group after 1.5 weeks of diabetes. NPH insulin (Eli Lilly, IN) was administered subcutaneous daily for 3 days (1 IU morning and 3 IU afternoon) before the MRI examination. On the day of the MRI examination, the rats received 1 IU in the morning 2–4 h before the MRI scan. The study complied with the guidelines for use and care of laboratory animals and was approved by the Danish Inspectorate of Animal Experiments (License: 2010/561-1938).

Colorimetric Assays

Assays to measure LDH and PDH activity and the absolute amount of lactate were performed according to manufacturer's instructions (Sigma-Aldrich, St. Louis, MO). The assays were performed on homogenized tissue samples dissolved in buffer from each of the respective assays, derived from cortical kidney biopsies. Biopsies were obtained at the time of sacrifice and stored in −80°C. Absorbance was measured in 384 Costar well plates using a PHERAstar FS microplate reader (BMG Labtech, Birkerød, Denmark). In a full spectrum test screen, we found that the optimal wavelength was 662 nm for LDH, PDH, and lactate. The calculated activities were normalized to protein content in the kidney sample. Protein content was determined using a Qubit 3.0 fluorometer (Life Technologies, Thermo Fisher Scientific, Hvidovre, Denmark).

RNA Extraction and Quantitative Polymerase Chain Reaction

RNA extraction and qPCR were performed. In brief, total RNA was isolated using a Nucleospin RNA II kit (Strategene, AH Diagnostics, Aarhus, Denmark) following manufacturer's instructions. We measured RNA purity and concentration using a Qubit 3.0 fluorometer (Life Technologies). cDNA synthesis was performed on 0.5-μg RNA with the RevertAid first-strand cDNA synthesis kit following manufacturer's instructions (Thermo Fisher Scientific). Samples for qPCR were prepared using Maxima SYBR Green Master Mix following manufacturer's instructions (Thermo Fisher Scientific). The qPCR protocol comprised 40 cycles of denaturation for 30 seconds at 95°C followed by annealing and synthesis for 1 minute at 60°C. Rat primer sequences used are described in Table 1. As mentioned, kidneys were rapidly dissected after sacrifice. Cortex and inner medulla were isolated to tubes and dumped in liquid nitrogen and stored in −80°C. Cortex biopsies were homogenized for RNA extraction.

[1-^{13}C]Pyruvate Hyperpolarization

A volume of 20-μL [1-^{13}C]pyruvic acid (Sigma Aldrich) containing 15mM OX063 (Oxford Instruments, Oxford, UK) and 1.5 mmol/L Dotarem (Guerbet, Villepinte, France) was inserted into a dissolution-DNP HyperSense polarizer (Oxford Instruments Molecular Biotools, Oxford, UK). The sample was polarized for

1 h at 94.118 GHz (100 mW). The hyperpolarized sample was dissolved in 4 mL of a dissolution medium (80 mmol/L TRIS, 100 mg/L EDTA, 50 mmol/L NaCl, 80 mmol/L NaOH), yielding an isotonic 80 mmol/L [1-^{13}C]-pyruvate solution at physiological pH. The sample temperature after dissolution was 30°C–35°C, resulting in a reproducible polarization of 30% and a T1 in the range of 40–60 seconds (26). A volume of 1.0 mL was injected into the tail vein over 10 seconds. The transfer time between dissolution and injection was 10 seconds on average, and the ^{13}C chemical shift imaging (CSI) MR-sequence was initiated 20 seconds after start of injection.

Magnetic Resonance Imaging and Spectroscopy

Two weeks after induction of diabetes, tail vein catheterization was performed for administration of hyperpolarized [1-^{13}C]pyruvate. The animal was placed in a 4.7 T Agilent MR scanner with VnmrJ 4.0 (Agilent, Santa Clara, CA) that was equipped with a dual-tuned ^{1}H/^{13}C volume transmit and a 4-channel array surface receive-coil (Rapid Biomedical, Würzburg, Germany). The protocol (Figure 1) consists of 2 baseline scans (^{1}H BOLD MRI and a ^{13}C magnetic resonance spectroscopy [MRS]) during hyperoxic breathing with 66% oxygen content (0.8% isoflurane, 0.66 L/min oxygen, and 0.34 L/min nitrogen) and 2 postinterventions scans (^{1}H BOLD MRI and a ^{13}C MRS) with a 10% oxygen content (15 minutes of 0.8% isoflurane, 0.10 L/min oxygen, and 0.90 L/min nitrogen). Temperature and respiration were monitored. After the MRI session, a 5- to 7-mL blood sample was collected from the aortic bifurcation to EDTA-coated tubes for determination of plasma electrolytes.

MRI and MRS sequence parameters were as follows. An oxygenation-dependent (T2*-weighted) sequence was performed using an axial ^{1}H multiecho gradient-echo sequence. The sequence parameters were: matrix = 128 × 128, field of view (FOV) = 60 × 60 mm^2, flip angle = 30°, repetition time (TR) = 300 milliseconds, number of transients = 16, echo time (TE) = 2, 4, 6, 8, 10, 12, 14, 16 milliseconds, slices = 3, slice thickness = 5 mm, covering both kidneys. A scout ^{1}H axial gradient echo sequence (matrix = 128 × 128, FOV = 60 × 60 mm^2, TR/TE = 100 ms/2.6 ms, flip angle = 20°, averages = 16, slices = 7, slice thickness = 3 mm, covering both kidneys) was acquired for anatomical overlay. A slice-selective 2D ^{13}C chemical-shift imaging sequence was used for hyperpolarized [1-^{13}C]-pyruvate imaging. Parameters were chosen to be similar to previous studies in the same animal model (4, 20): flip angle = 10°, a centric circular k-space trajectory (169 phase encodings), TR/TE = 75 ms/0.65 ms, FOV = 60 × 60 mm^2, spectral width = 4000 Hz, data sampling = 256 complex points, and an axial slice thickness = 20 mm, covering both kidneys.

MRI Analysis

Data analysis of BOLD MRI data was performed in VnmrJ 4.0, generating R_2* maps. CSI data were processed in Matlab (MathWorks, Natick, MA). Spatial dimensions were apodized with a hamming function and zero-filled to a 32 × 32 grid. The spectral dimension was centered on the pyruvate frequency; apodized with a zero shifted sine-bell function and a 5-Hz exponential line broadening; and processed as sum-of-squares of the four coil channels. Spectral analysis was performed on a single voxel placed inside the kidney. Metabolite signals were integrated over a 60-Hz symmetric region. The metabolite signals were normalized relative to the total carbon signal.

Statistical Analyses

Normality was assessed with quantile plots. $P < .05$ was considered statistically significant. A 2-way repeated measurement analysis of variance (ANOVA) was used to compare the metabolic response as a function of oxygen availability between the three groups, using Sidak corrections for multiple comparisons. Statistical analysis was performed in PRISM. Statistical analysis of animal, kidney weight and blood glucose were analyzed with a 1-way ANOVA, while HbA_{1c} between the diabetics and the diabetics receiving insulin was analyzed using a 2-tailed Student t test with equal variance. The intrarenal lactate concentration variance was analyzed using a Brown–Forsyth test of variance.

RESULTS

All diabetic rats developed sustained hyperglycemia within 48 h. Body weight, kidney weight, and long-term glucose level HbA1c were comparable between diabetes and insulin-treated groups (Table 2). Renal oxygen availability depended on the inspired oxygen content, and BOLD MRI showed a significantly decreased T2* in the renal cortex in all groups following a reduction in the oxygen content of the breathing gas (diabetes group, diabetes + insulin group, and control group) ($P < .001$) (Figure 2). The medullary T2* was inversely correlated with oxygen content in the breathing gas in both the diabetes group ($P = .0009$) and in the diabetes + insulin group, albeit the latter did not reach significance ($P = .087$) (Figure 2). On the other hand, T2* was unaffected by altered oxygen availability in the control group ($P = .96$) (Figure 2). Both untreated diabetic ($P < .001$) and insulin-treated diabetic ($P < .001$) rats had an overall increased lactate production (lactate-to-total carbon ratio) in the kidneys compared with healthy controls. In both the untreated diabetes group ($P = .001$) and the insulin-treated diabetes group ($P = .004$), we found a decreased lactate-to-total carbon ratio in response to decreased oxygen availability, while the healthy controls ($P = .035$) showed a significantly increased lactate-to-total carbon ratio in response to decreased oxygen availability (Figure 3). The alanine and the bicarbonate-to-total carbon ratios were unaffected by altered oxygen supply in all groups (Figure 3). The pyruvate-to-total carbon ratio increased after administration of a low oxygen content in the diabetes group compared with controls ($P < .001$), and similar findings were found in the diabetes + insulin group ($P < .001$), while a tendency toward a decreased pyruvate signal was observed in the diabetes + insulin group ($P = .070$) (Figure 3). A statistically significant variance (Brown–Forsyth test, $P = .040$) was found in renal lactate concentration among the groups, indicating a significantly elevated lactate concentration in the 2 diabetes groups compared with controls (Figure 4).

A statistically significant difference in lactate dehydrogenase activity was found between both diabetes groups and the control group ($P = .001$), with the highest activity seen in the diabetes + insulin group, while no difference in LDH expression was seen between any of the groups (Figure 4). No difference

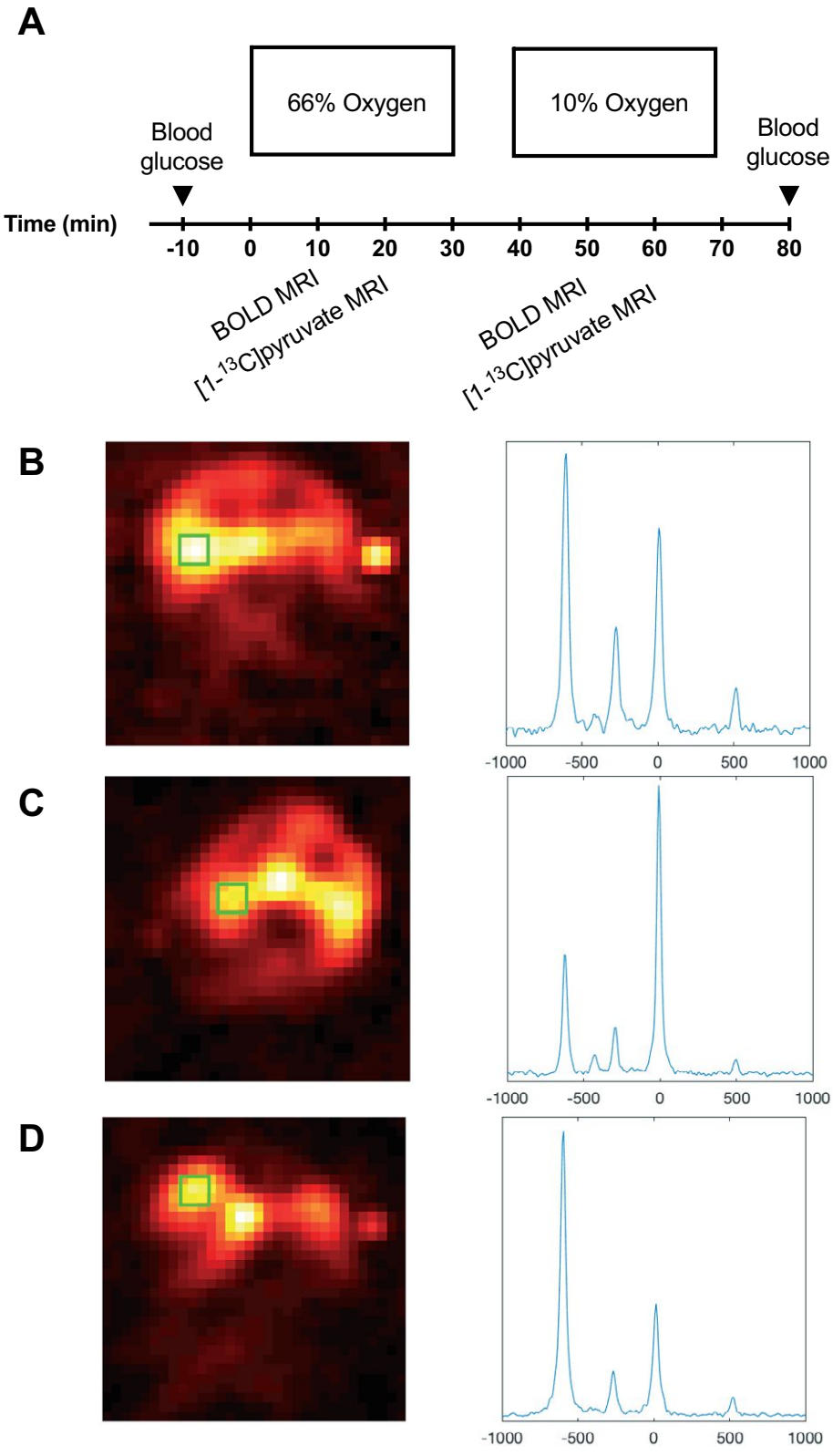

Figure 1. Study protocol (A). All animals were exposed to either 66% oxygen content or 10% oxygen content in the breathing gas. Blood oxygen level–dependent (BOLD) scan is performed 10 minutes after the change of oxygen content followed by a hyperpolarized ^{13}C pyruvate scan 20 minutes thereafter. Hyperpolarized ^{13}C chemical shift imaging (CSI) image of a healthy control animal and accompanying kidney spectra from the green region of interest (ROI) (B). Hyperpolarized ^{13}C CSI image of a untreated diabetic animal and accompanying kidney spectra from the green ROI (C). Hyperpolarized ^{13}C CSI image of an insulin-treated diabetic animal and accompanying kidney spectra from the green ROI (D).

Table 2. Animal Characteristics

	Body Weight (g)	Kidney Weight (g)	Blood Glucose (mmol/L)	HbA_{1c} (%)
Control	222 ± 7	0.8 ± 0.1	8.6 ± 0.7	Not measured
Diabetes	213 ± 20	1.1 ± 0.1[a]	23.8 ± 3.8[a]	11.4 ± 1.5
Diabetes + Insulin	200 ± 26	1.1 ± 0.2[a]	21.0 ± 4.0[a]	12.3 ± 0.7

[a]$P < 0.05$ versus control. The blood glucose level is the average blood glucose of the 2 measurements performed in each rat. Values are represented as mean ± SD. Comparisons analyzed using 1-way ANOVA and Student *t* test.

was seen in the lactate-to-bicarbonate, lactate-to-alanine, and alanine-to-bicarbonate ratios in untreated and insulin-treated diabetic rats during inspiration of 66% and 10% oxygen in the breathing gas (Figure 5). The pyruvate dehydrogenase activity increased in the untreated diabetes group, while the PDH expression was significantly decreased in both diabetes groups (Figure 6). Monocarboxylate transporters (MCT1) was found to be similar in all groups ($P = .27$), whereas MCT4 was found to be significantly reduced in both diabetes groups ($P < .001$) (Figure 6).

DISCUSSION

We have previously reported that the diabetic kidney responded with a pronounced increase in lactate formation following reduced oxygen availability compared with healthy controls (3). The decreased lactate formation in response to low oxygen availability observed in the present study is likely explained by the severity of diabetic nephropathy and the more increased lactate level (80% increased pyruvate-to-lactate conversion compared with previous reports (3, 20). The underlying mechanism for this altered metabolic phenotype is believed to originate from the altered expression of MCT4 in the diabetic rat kidney (dramatically downregulated) in response to profound lactate accumulation similar to what is observed in response to prolonged hypoxia (27). MCT1 controls the influx of lactate, whereas MCT4 ensures redox balance by export of lactate. Restricting lactic acid efflux from renal cells (maintained or reduced MCT4 expression) in concern with increased intracellular lactic acid accumulation, leading to an increased hyperpolarized [1-^{13}C]pyruvate-to-[1-^{13}C]lactate conversion (increased MCT1 expression in diabetes), might be a preventive mechanism to avoid systemic lactic acidosis, as seen in muscles, where an intracellular accumulation of lactic acid and subsequent altered redox state will inhibit glycolysis and induce muscle fatigue before systemic alterations to the pH regulation of the body (27, 28). Indeed mild acidosis has recently been associated with an altered metabolic phenotype in postmitotic cells, overriding oxygen deprivation and thus maintaining mitochondrial function (29). Taken together, an altered MCT transport is essential to the metabolic phenotype seen in diabetes, and an altered efflux of lactate could be the origin of this counterintuitive oxygen reversed oxygen sensitivity.

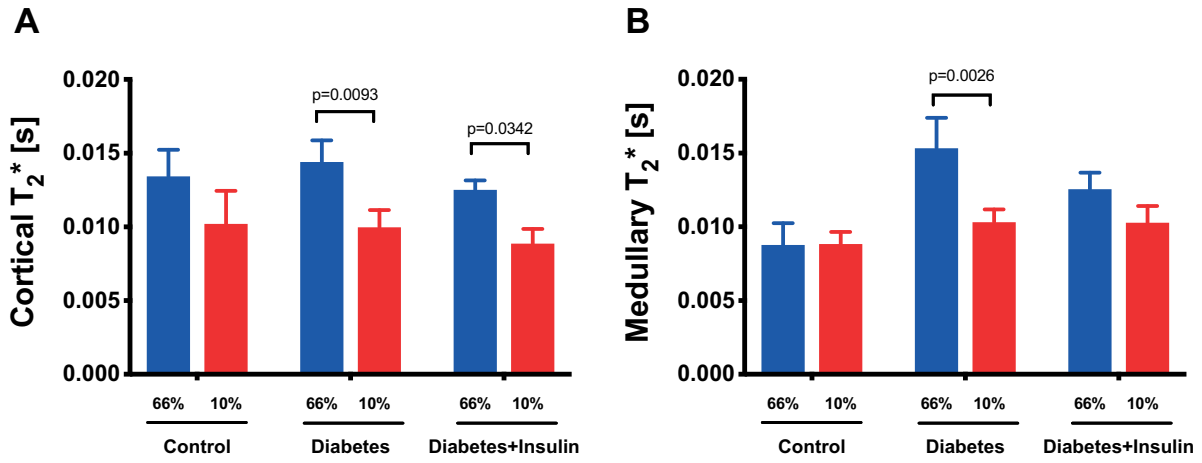

Figure 2. BOLD magnetic resonance imaging (MRI) in cortex and medulla of controls and untreated and insulin-treated diabetic rats during inspiration of 66% and 10% oxygen in the breathing gas. (**Cortical T2***) $P = .68$ for group (*between healthy controls* and *untreated and* insulin-treated *diabetic rats*), $P = .0001$* for treatment (*inspired oxygen*), and $P = .81$ for interaction (A). (**Medullary T2***) $P = .08$ for group (*between healthy controls* and *untreated and* insulin-treated *diabetic rats*), $P = .005$* for treatment (*Inspired oxygen*), and $P = .04$ for interaction* (B). Lines denote mean ± SEM. Two-way repeated ANOVA.

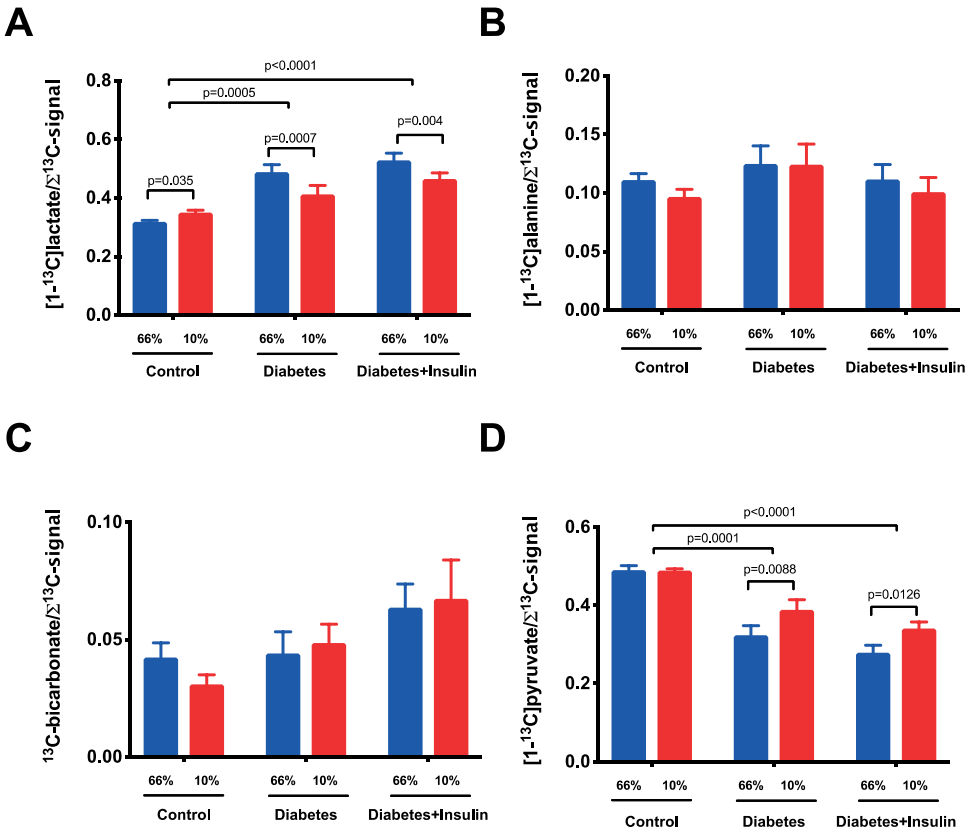

Figure 3. Hyperpolarized lactate, pyruvate, alanine, and bicarbonate signal to sum of the signal ratios in controls and untreated and insulin-treated diabetic rats during inspiration of 66% and 10% oxygen in the inspired air. (**Lactate-to-Σsignal**) $P < .001$ for group* (*between healthy controls* and *untreated and* insulin-treated *diabetic rats*), $P = .002$* for treatment (*inspired oxygen*), and $P = .0007$ for interaction* (A). (**Alanine-to-Σsignal**) $P = .43$ for group (*between healthy controls* and *untreated and* insulin-treated *diabetic rats*), $P = .15$ for treatment (*inspired oxygen*), and $P = .6$ for interaction (B). (**Pyruvate-to-Σsignal**) $P < .001$ for group* (*between healthy controls* and *untreated and* insulin-treated *diabetic rats*), $P = .002$ for treatment* (*inspired oxygen*), and $P = .05$ for interaction* (C); (**Bicarbonate-to-Σsignal**) $P = .1$ for group* (*between healthy controls* and *untreated and* insulin-treated *diabetic rats*), $P = .85$ for treatment* (*inspired oxygen*), and $P = .46$ for interaction. Two-way repeated ANOVA (D).

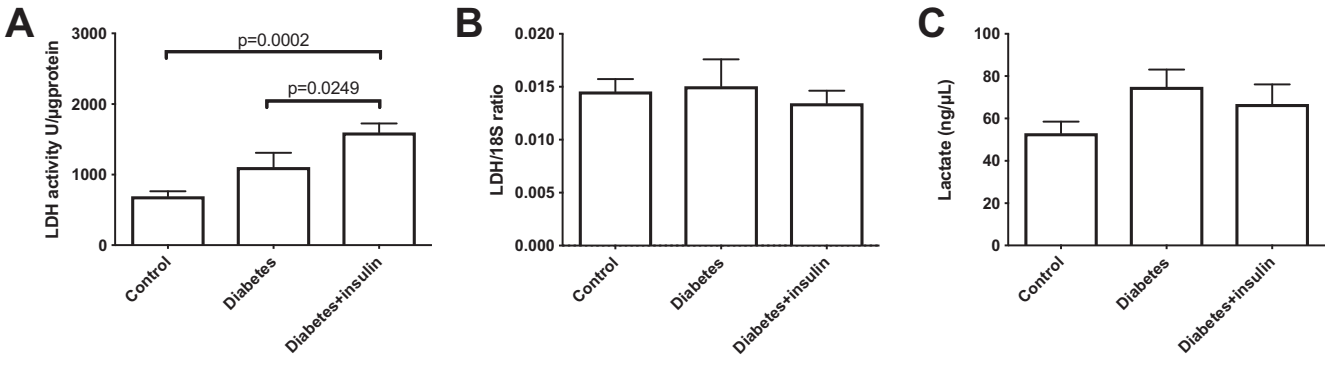

Figure 4. Colorimetric assay lactate dehydrogenase activity ($P = .001$) (A), qPCR lactate dehydrogenase mRNA expression ($P = .787$) (B), and colorimetric assay kidney tissue lactate concentration ($P = .187$) (C); significant variance (Brown–Forsyth test, $P = .04$) was found between healthy controls and untreated and insulin-treated diabetic rats. One-way ANOVA.

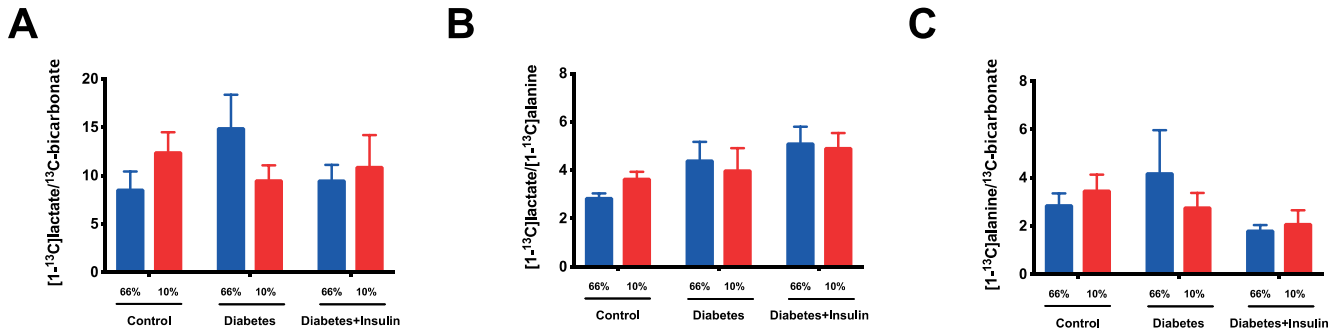

Figure 5. Hyperpolarized lactate-to-bicarbonate, lactate-to-alanine, and alanine-to-bicarbonate signal ratios in untreated and insulin-treated diabetic rats during inspiration of 66% and 10% oxygen in the inspired air. (**Lactate-to-Bicarbonate**) $P = .73$ for group (*between healthy controls* and *untreated and insulin-treated diabetic rats*), $P = .98$ for treatment (*inspired oxygen*), and $P = .06$ for interaction (A). (**Lactate-to-Alanine**) $P = .14$ for group (*between healthy controls* and *untreated and insulin-treated diabetic rats*), $P = .78$ for treatment (*inspired oxygen*), and $P = .12$ for interaction (B). (**Alanine-to-bicarbonate**) $P = .32$ for group (*between healthy controls* and *untreated and insulin-treated diabetic rats*), $P = .72$ for treatment (*Inspired oxygen*), and $P = .23$ for interaction (C). Two-way repeated ANOVA.

We speculate that the altered lactate transport could be active inhibition of the monocarboxylic transporters, as previously shown for the active mitochondrial pyruvate transporter with α-cyano-4-hydroxycinnamate (30) and in muscle tissue where lactate uptake and efflux stimulate an increased lactate concentration and altered intra- and extracellular pH (31).

Interestingly, the increased lactate-to-total carbon ratio in the diabetic kidney occurred regardless of insulin supplementation, indicating that insulin did not affect the balance between oxygen availability and energy metabolism in the hypoxic diabetic kidney. These findings support previous reports on increased lactate production in the diabetic kidneys regardless of

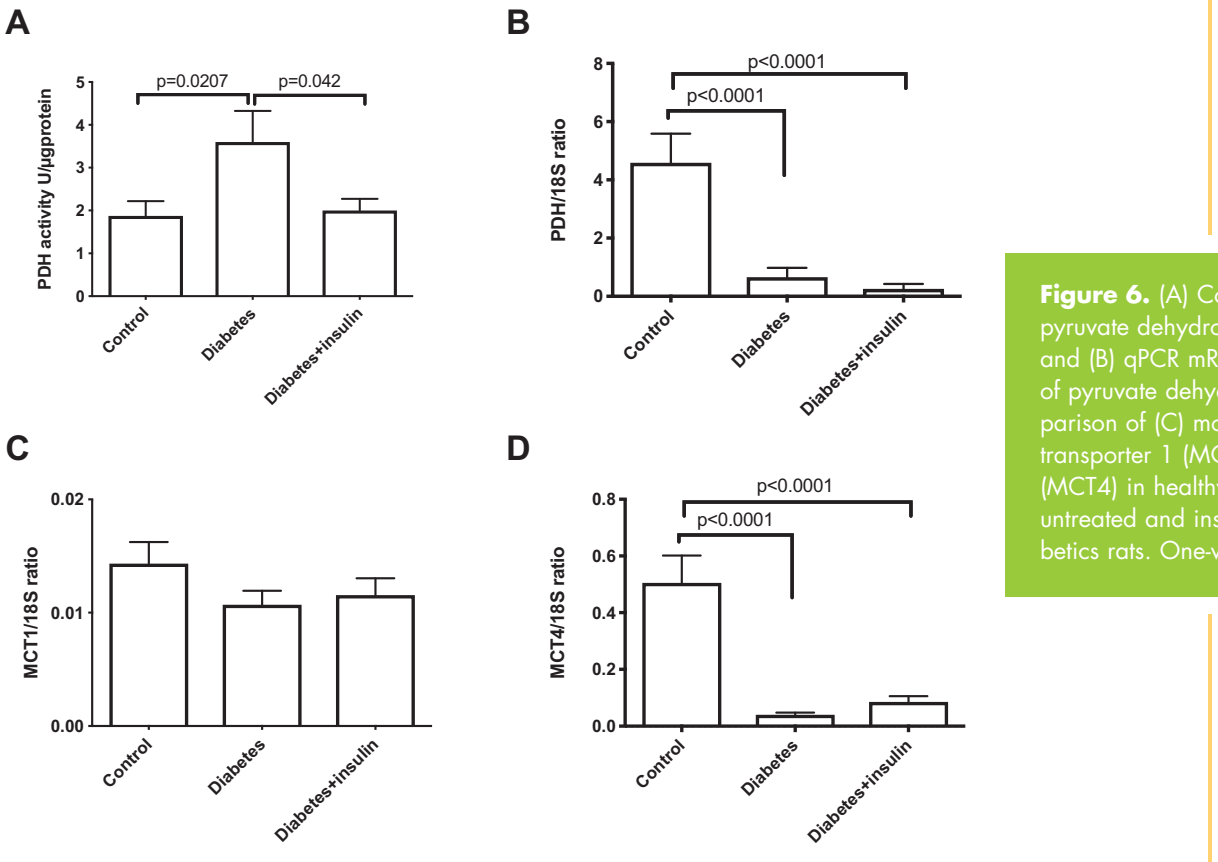

Figure 6. (A) Colorimetric assay pyruvate dehydrogenase activity and (B) qPCR mRNA expressions of pyruvate dehydrogenase; comparison of (C) monocarboxylate transporter 1 (MCT1) and (D) 4 (MCT4) in healthy controls and untreated and insulin-treated diabetics rats. One-way ANOVA.

insulin treatment (20). However, these results also imply the presence of different metabolic phenotypes occurring in diabetes, as high intrarenal lactate levels significantly altered the response to reduced oxygen availability in the diabetic animals (3, 4, 20, 25). This finding might be explained by the need for the high lactate-producing kidney to maintain homeostasis during hypoxia as previously reported in cancer cells (32). Thus, acute hypoxia in an already high lactate environment increases the lactate-to-pyruvate conversion and/or reduces the pyruvate-to-lactate conversion and thus maintains the intracellular redox potential. It is unlikely that the difference in the metabolic conversion is due to decreased conversion in diabetic rats, as the pyruvate-to-total carbon ratio was lower (ie, more pyruvate is being converted to its metabolic derivatives) in diabetics compared with controls.

The increased pyruvate-to-lactate conversion may characterize the severity of the deranged metabolism in the diabetic kidney, as previously described by Lin et al. (33). However, the increased lactate-to-pyruvate level found in the diabetic kidney in this study was not directly linked to severity, and thus, the altered response to oxygen supply may enable a further differentiation of the metabolic phenotype by interrogating the underlying mechanism, thus providing a window of opportunity for pharmacologically targeting these metabolically different phenotypes. In fact, recent studies have indicated that increased glycolytic flux as a renal protective trait and thus the phenotype seen here might be better protected against renal impairment (34). The alanine-to-total carbon ratio, regulated by the alanine transferase and linked via the cosubstrate glutamate and α-ketoglutarate to the glutamine and fatty acid synthesis, is insensitive to the changes in inhaled oxygen. This lack of oxygen dependency indicates a generally sufficient oxygen availability to maintain the increased mitochondrial fatty acid oxidation in kidney tubular cells (35) and similarly the bicarbonate-to-total carbon ratio that describes the oxidative phosphorylation via the mitochondrial pyruvate dehydrogenase activity (2-4). The oxygen-sensitive BOLD MRI showed hypoxia and increased oxygen consumption. These measurements indicate that a general deranged metabolism is inversely dependent on oxygen availability in the severe pseudohypoxic diabetic kidney, both with and without insulin treatment. Therefore, we suggest that the sensitivity toward changes in oxygen supply defines an alternative diabetic phenotype, indicating reduction in active cellular uptake of pyruvate. A potential limitation in the study design is the use of CSI for spatial localization of the metabolites, limiting the spatial resolution and especially the temporal resolution compared with faster or higher resolution imaging methods (26, 36-39). Another limitation is the need for anesthetics, which have been shown to impact the renal metabolism (40), although the used regime has only mild renal effects compared with other anesthetic regimes. Insulin administration did not alter the overall metabolic phenotype, which is supported by previous studies in heart and kidneys (20, 41, 42). However, it is important to note that the used insulin treatment was a dose mimicking suboptimal insulin treatment similar to a previous report (20), and as such, it is currently unknown what the impact of adequate insulin administration for sufficient glycemic control would entail. Further, 66% oxygen was chosen to ensure fully saturated blood, thus maximizing the potential differences between hypoxia and hyperoxia. No difference was observed between the results of this study in healthy controls and previous reports in controls and diabetics under normoxia and hyperoxia (100%) (3), and thus, it is unlikely that hyperoxia (66% O_2 in inspired air) was significantly contributing to the higher lactate production seen in the diabetic rats. Hyperglycemia-induced ketosis could be another potential confounding factor in the metabolic phenotypes, although rarely seen in the animal model used in this study (43); individual metabolic states could be a contributing factor in the increased variance seen in the diabetic rats.

In conclusion, the altered metabolic phenotype, manifested as significantly altered oxygen sensitivity in the presence of high intrarenal lactate levels, shows the existence of two seemingly different metabolic phenotypes in the diabetic kidney, which may highlight the need for tailored treatment strategies to reduce the impact of diabetes on long-term kidney function.

ACKNOWLEDGMENTS

The study was supported by The Simon Spies Foundation and the Danish National Research Foundation. Sascha Gude is acknowledged for her laboratory assistance.

Disclosures: No disclosures to report.

Conflict of Interest: The authors have no conflict of interest to declare.

REFERENCES

1. Brownlee M. Biochemistry and molecular cell biology of diabetic complications. Nature. 2001;414:813–820.
2. Palm F, Hansell P, Ronquist G, Waldenstr m A, Liss P, Carlsson PO. Polyol-pathway-dependent disturbances in renal medullary metabolism in experimental insulin-deficient diabetes mellitus in rats. Diabetologia. 2004;47:1223–1231.
3. Laustsen C, Lycke S, Palm F, Ostergaard JA, Bibby BM, Norregaard R, Flyvbjerg A, Pedersen M8, Ardenkjaer-Larsen JH. High altitude may alter oxygen availability and renal metabolism in diabetics as measured by hyperpolarized [1-13C]pyruvate magnetic resonance imaging. Kidney Int. 2014;86:67–74.
4. Laustsen C, Østergaard JA, Lauritzen MH, Nørregaard R, Bowen S, Søgaard LV, Flyvbjerg A, Pedersen M, Ardenkjaer-Larsen JH. Assessment of early diabetic renal changes with hyperpolarized [1-13C]pyruvate. Diabetes Metab Res Rev. 2013;29:125–129.
5. Laustsen C. Hyperpolarized renal magnetic resonance imaging: potential and oitfalls. Front Physiol. 2016;7:72.
6. Williamson JR, Chang K, Frangos M, Hasan KS, Ido Y, Kawamura T, Nyengaard JR, van den Enden M, Kilo C, Tilton RG. Hyperglycemic pseudohypoxia and diabetic complications. Diabetes. 1993;42:801–813.
7. Zhang G, Darshi M, Sharma K. The Warburg effect in diabetic kidney disease. Semin Nephrol. 2018;38:111–120.
8. Wolf M, de Boer A, Sharma K, Boor P, Leiner T, Sunder-Plassmann G, Moser E, Caroli A, Jerome NP. Magnetic resonance imaging T1- and T2-mapping to assess renal structure and function: a systematic review and statement paper. Nephrol Dial Transplant. 2018;33:ii41–ii50.
9. Caroli A, Schneider M, Friedli I, Ljimani A, De Seigneux S, Boor P, Gullapudi L8, Kazmi I, Mendichovszky IA, Notohamiprodjo M, Selby NM, Thoeny HC, Grenier N, Vallée JP. Diffusion-weighted magnetic resonance imaging to assess diffuse

renal pathology: a systematic review and statement paper. Nephrol Dial Transplant. 2018;33:ii29–ii40.
10. Pruijm M, Mendichovszky IA, Liss P, Van der Niepen P, Textor SC, Lerman LO, Krediet CTP, Caroli A, Burnier M, Prasad PV. Renal blood oxygenation level-dependent magnetic resonance imaging to measure renal tissue oxygenation: a statement paper and systematic review. Nephrol Dial Transplant. 2018;33:ii22–ii8.
11. Odudu A, Nery F, Harteveld AA, Evans RG, Pendse D, Buchanan CE, Francis ST, Fernández-Seara MA. Arterial spin labelling MRI to measure renal perfusion: a systematic review and statement paper. Nephrol Dial Transplant. 2018;33:ii15–ii21.
12. Boor P, Perkuhn M, Weibrecht M, Zok S, Martin I.V., Gieseke J, Schoth F, Ostendorf T, Kuhl C, Floege J. Diffusion-weighted MRI does not reflect kidney fibrosis in a rat model of fibrosis. J Magn Reson Imaging. 2015;42:990–998.
13. Friedli I, Crowe LA, Berchtold L, Moll S, Hadaya K, de Perrot T, Vesin C, Martin PY, de Seigneux S, Vallée JP. New magnetic resonance imaging index for renal fibrosis assessment: A comparison between diffusion-weighted imaging and T1 mapping with histological validation. Sci Rep. 2016;6:30088.
14. Laustsen C, Stokholm Norlinger T, Christoffer Hansen D, Qi H, Mose Nielsen P, Bonde Bertelsen L, Henrik Ardenkjaer-Larsen J, Stødkilde Jørgensen H. Hyperpolarized 13C urea relaxation mechanism reveals renal changes in diabetic nephropathy. Magn Reson Med. 2016;75:515–518.
15. Pedersen M, Dissing TH, Morkenborg J, Stodkilde-Jorgensen H, Hansen LH, Pedersen LB, Grenier N, Frøkiaer J. Validation of quantitative BOLD MRI measurements in kidney: application to unilateral ureteral obstruction. Kidney Int. 2005; 67:2305–2312.
16. Ardenkjaer-Larsen JH, Fridlund B, Gram A, Hansson G, Hansson L, Lerche MH, Servin R, Thaning M, Golman K. Increase in signal-to-noise ratio of >10,000 times in liquid-state NMR. Proc Natl Acad Sci U S. 2003;100:10158–10163.
17. Nelson SJ, Kurhanewicz J, Vigneron DB, Larson PEZ, Harzstark AL, Ferrone M, van Criekinge M, Chang JW, Bok R, Park I, Reed G, Carvajal L, Small EJ, Munster P, Weinberg VK, Ardenkjaer-Larsen JH, Chen AP, Hurd RE, Odegardstuen LI, Robb FJ, Tropp J, Murray JA. Metabolic imaging of patients with prostate cancer using hyperpolarized [1-^{13}C]pyruvate. Sci Transl Med. 2013;5:198ra08.
18. Kurhanewicz J, Vigneron DB, Brindle K, Chekmenev EY, Comment A, Cunningham CH, Deberardinis RJ, Green GG, Leach MO, Rajan SS, Rizi RR, Ross BD, Warren WS, Malloy CR. Analysis of cancer metabolism by imaging hyperpolarized nuclei: prospects for translation to clinical research. Neoplasia. 2011;13: 81–97.
19. Kurhanewicz J, Vigneron DB, Ardenkjaer-Larsen JH, Bankson JA, Brindle K, Cunningham CH, Gallagher FA, Keshari KR, Kjaer A, Laustsen C, Mankoff DA, Merritt ME, Nelson SJ, Pauly JM, Lee P, Ronen S, Tyler DJ, Rajan SS, Spielman DM, Wald L, Zhang X, Malloy CR, Rizi R. Hyperpolarized (13)C MRI: path to clinical translation in oncology. Neoplasia. 2018;21:1–16.
20. Laustsen C, Lipso K, Ostergaard JA, Norregaard R, Flyvbjerg A, Pedersen M, Palm F, Ardenkjær-Larsen JH. Insufficient insulin administration to diabetic rats increases substrate utilization and maintains lactate production in the kidney. Physiol Rep. 2014;2. pii: e12233.
21. Qi H, Nielsen PM, Schroeder M, Bertelsen LB, Palm F, Laustsen C. Acute renal metabolic effect of metformin assessed with hyperpolarised MRI in rats. Diabetologia. 2018;61:445–454.
22. Norlinger TS, Nielsen PM, Qi H, Mikkelsen E, Hansen K, Schmidt NH, Pedersen M, Agger P, Palm F, Laustsen C. Hyperbaric oxygen therapy reduces renal lactate production. Physiol Rep. 2017;5. pii: e13217.
23. von Morze C, Chang GY, Larson PE, Shang H, Allu PK, Bok RA, Crane JC, Olson MP, Tan CT, Marco-Rius I, Nelson SJ, Kurhanewicz J, Pearce D, Vigneron DB. Detection of localized changes in the metabolism of hyperpolarized gluconeogenic precursors 13 C-lactate and 13 C-pyruvate in kidney and liver. Magn Reson Med. 2017;77:1429–1437.
24. Morze CV, Allu PKR, Chang GY, Marco-Rius I, Milshteyn E, Wang ZJ, Ohliger MA, Gleason CE, Kurhanewicz J, Vigneron DB, Pearce D. Non-invasive detection of divergent metabolic signals in insulin deficiency vs. insulin resistance in vivo. Sci Rep. 2018;8:2088.
25. Laustsen C, Nielsen PM, Norlinger TS, Qi H, Pedersen UK, Bertelsen LB, Østergaard JA, Flyvbjerg A, Ardenkjær-Larsen JH, Palm F, Stødkilde-Jørgensen H. Antioxidant treatment attenuates lactate production in diabetic nephropathy. Am J Physiol Renal Physiol. 2017;312:F192–F199.
26. Schmidt R, Laustsen C, Dumez JN, Kettunen MI, Serrao EM, Marco-Rius I, Brindle KM, Ardenkjaer-Larsen JH, Frydman L. In vivo single-shot 13C spectroscopic imaging of hyperpolarized metabolites by spatiotemporal encoding. J Magn Reson. 2014;240:8–15.
27. Halestrap AP, Wilson MC. The monocarboxylate transporter family–role and regulation. IUBMB Life. 2012;64:109–119.
28. Bellomo R. Bench-to-bedside review: lactate and the kidney. Crit Care. 2002;6: 322–326.
29. Khacho M, Tarabay M, Patten D, Khacho P, MacLaurin JG, Guadagno J, Bergeron R, Cregan SP, Harper ME, Park DS, Slack RS. Acidosis overrides oxygen deprivation to maintain mitochondrial function and cell survival. Nat Commun. 2014;5:3550.
30. McCommis KS, Finck BN. Mitochondrial pyruvate transport: a historical perspective and future research directions. Biochem J. 2015;466:443–454.
31. Philp A, Macdonald AL, Watt PW. Lactate – a signal coordinating cell and systemic function. J Exp Biol. 2005;208:4561–4575.
32. Xie J, Wu H, Dai C, Pan Q, Ding Z, Hu D, Ji B, Luo Y, Hu X. Beyond Warburg effect – dual metabolic nature of cancer cells. Sci Rep. 2014;4:4927.
33. Lin MH, Chen HY, Liao TH, Huang TC, Chen CM, Lee JA. Determination of time-dependent accumulation of D-lactate in the streptozotocin-induced diabetic rat kidney by column-switching HPLC with fluorescence detection. J Chromatogr B Analyt Technol Biomed Life Sci. 2011;879:3214–3219.
34. Qi W, Keenan HA, Li Q, Ishikado A, Kannt A, Sadowski T, Yorek MA, Wu IH, Lockhart S, Coppey LJ, Pfenninger A, Liew CW, Qiang G, Burkart AM, Hastings S, Pober D, Cahill C, Niewczas MA, Israelsen WJ, Tinsley L, Stillman IE, Amenta PS, Feener EP, Vander Heiden MG, Stanton RC, King GL. Pyruvate kinase M2 activation may protect against the progression of diabetic glomerular pathology and mitochondrial dysfunction. Nat Med. 2017;23:753–762.
35. Rosca MG, Vazquez EJ, Chen Q, Kerner J, Kern TS, Hoppel CL. Oxidation of fatty acids is the source of increased mitochondrial reactive oxygen species production in kidney cortical tubules in early diabetes. Diabetes. 2012;61:2074–2083.
36. Vinding MS, Laustsen C, Maximov I.I., Sogaard LV, Ardenkjaer-Larsen JH, Nielsen NC. Dynamic nuclear polarization and optimal control spatial-selective 13C MRI and MRS. J Magn Reson. 2013;227:57–61.
37. Gordon JW, Niles DJ, Fain SB, Johnson KM. Joint spatial-spectral reconstruction and k-t spirals for accelerated 2D spatial/1D spectral imaging of 13C dynamics. Magn Reson Med. 2014;71:1435–1445.
38. Milshteyn E, von Morze C, Gordon JW, Zhu Z, Larson PEZ, Vigneron DB. High spatiotemporal resolution bSSFP imaging of hyperpolarized [1-(13) C]pyruvate and [1-(13) C]lactate with spectral suppression of alanine and pyruvate-hydrate. Magn Reson Med. 2018;80:1048–1060.
39. Lau JYC, Geraghty BJ, Chen AP, Cunningham CH. Improved tolerance to off-resonance in spectral-spatial EPI of hyperpolarized [1-(13) C]pyruvate and metabolites. Magn Reson Med. 2018;80:925–934.
40. Qi H, Mariager CO, Lindhardt J, Nielsen PM, Stodkilde-Jorgensen H, Laustsen C. Effects of anesthesia on renal function and metabolism in rats assessed by hyperpolarized MRI. Magn Reson Med. 2018;80:2073–2080.
41. Lauritzen MH, Laustsen C, Butt SA, Magnusson P, Sogaard LV, Ardenkjaer-Larsen JH, Åkeson P. Enhancing the [13C]bicarbonate signal in cardiac hyperpolarized [1-13C]pyruvate MRS studies by infusion of glucose, insulin and potassium. NMR Biomed. 2013;26:1496–1500.
42. Hansen ESS, Tougaard RS, Norlinger TS, Mikkelsen E, Nielsen PM, Bertelsen LB, Bøtker HE, Jørgensen HS, Laustsen C. Imaging porcine cardiac substrate selection modulations by glucose, insulin and potassium intervention: a hyperpolarized [1-(13) C]pyruvate study. NMR Biomed. 2017;30.
43. Forster O, Rudas B. Ketosis in rats with streptozotocin-induced diabetes. Lancet. 1969;1:1321–1322.

TOMOGRAPHY® RESEARCH ARTICLE

Switching Circuit Optimization for Matrix Gradient Coils

Stefan Kroboth[1], Kelvin J. Layton[2], Feng Jia[1], Sebastian Littin[1], Huijun Yu[1], Jürgen Hennig[1], and Maxim Zaitsev[1]

[1]Department of Radiology, Medical Physics, Medical Center University of Freiburg, Faculty of Medicine, University of Freiburg, Freiburg, Germany and [2]Institute for Telecommunications Research, University of South Australia, Adelaide, Australia

Corresponding Author:
Stefan Kroboth, MSc
Killianstr 5a Freiburg, Germany 79106;
E-mail: stefan.kroboth@uniklinik-freiburg.de

Key Words: magnetic resonance imaging, matrix gradient coil, combinatorial optimization, switching circuit, nonlinear encoding
Abbreviations: Field of view (FOV), simulated annealing (SA), genetic algorithm (GA)

ABSTRACT

Matrix gradient coils with up to 84 coil elements were recently introduced for magnetic resonance imaging. Ideally, each element is driven by a dedicated amplifier, which may be technically and financially infeasible. Instead, several elements can be connected in series (called a "cluster") and driven by a single amplifier. In previous works, a set of clusters, called a "configuration," was sought to approximate a target field shape. Because a magnetic resonance pulse sequence requires several distinct field shapes, a mechanism to switch between configurations is needed. This can be achieved by a hypothetical switching circuit connecting all terminals of all elements with each other and with the amplifiers. For a predefined set of configurations, a switching circuit can be designed to require only a limited amount of switches. Here we introduce an algorithm to minimize the number of switches without affecting the ability of the configurations to accurately create the desired fields. The problem is modeled using graph theory and split into 2 sequential combinatorial optimization problems that are solved using simulated annealing. For the investigated cases, the results show that compared to unoptimized switching circuits, the reduction of switches in optimized circuits ranges from 8% to up to 44% (average of 31%). This substantial reduction is achieved without impeding circuit functionality. This study shows how technical effort associated with implementation and operation of a matrix gradient coil is related to different hardware setups and how to reduce this effort.

INTRODUCTION

Recently, matrix gradient coils (also termed multi-coils or multi-coil arrays) were introduced for both magnetic resonance image acquisition and B_0 shimming (1-6). Almost 2 decades earlier, a similar concept called *matrix shim coil system* was introduced for nuclear magnetic resonance (7). Such coils consist of a multitude of (up to 84) compact coil elements, which are in the most trivial configuration individually supplied by a current amplifier. The created field is a superposition of the fields produced by individual coil elements. This multiple-coil topology allows for the creation of a large variety of different field shapes by adjusting the currents in the individual coil elements. The use of multiple coils has certain advantages over that of conventional gradient coils and it opens up new possibilities to imaging and shimming. In most realizations, coil elements of a matrix gradient coil are smaller than typical dimensions of conventional gradient coils, which allows for faster switching of currents. One problem associated with conventional linear gradient coils is the requirement of highly linear fields across the entire field of view (FOV). With matrix gradient coils, encoding fields can be adapted to the actual FOV needed for the given imaging application. This may potentially be more accurate and/or more efficient (4), particularly for small FOVs.

Matrix gradient coils are furthermore favorable for nonlinear spatial encoding schemes such as PatLoc (8-15), O-Space (16-19), or FRONSAC (20). Imaging techniques that incorporate nonlinear gradients into the magnetic resonance pulse sequence can utilize the matrix gradient coil's ability to create a wide variety of field shapes whose nonlinearity extends way beyond that of the quadratic fields used in previous work. For magnetic resonance imaging applications that focus on local anatomy, nonlinear gradients allow for fast sequences that produce high-resolution images in a target area and low-resolution images everywhere else (13). Example images acquired with a matrix gradient coil can be found in Littin et al.'s study (2), but owing to the novelty of the concept, many topics mentioned above require further research and have not made it into clinical applications yet.

Design strategies for unconventional gradient coils are still a topic of active research. For classical linear gradients, the entire gradient system is typically split into 3 gradient channels that correspond to principal spatial directions X, Y, and Z. Each

ISSN 2379-1381 https://doi.org/10.18383/j.tom.2018.00056

independently driven channel lies on a separate surface within the gradient coil structure and is designed mostly independent of the other channels. Variations of the target field method (21-23) are typically used combined with modern numerical optimization techniques, allowing for a simultaneous control of the manufacturing constraints such as minimal conductor spacing, electrical characteristics such as coil inductance, resistance and minimal mutual coupling, as well as fidelity of the achieved field profiles. Less conventional gradient system concepts pursue different design strategies, typically including multiple steps. For example, a linear Z gradient coil with a dynamically movable imaging region (24) was realized by designing a multitude of current density patterns for varying FOV offsets, followed by a singular value decomposition step to compress these current densities into 3 electrical channels to be controlled by individual gradient amplifiers. In contrast to the aforementioned design strategies, when designing a matrix coil, the target field or set of fields is in general unknown. One strategy to address this challenge is to split the poorly defined and computationally intractable problem into a set of smaller tractable problems. For the matrix coil in Littin et al.'s study (2), these steps included the following:

1. definition of the number of elements to balance the field strength and flexibility against power dissipation (25),
2. optimization of the geometry and winding patterns of individual elements to achieve maximum gradient strength and sufficient shielding (6),
3. obtaining a method to drive the matrix gradient coil with substantially fewer amplifiers than coil elements by assigning several coil elements to each of the amplifiers (called a configuration) while preserving the matrix gradient coils' ability to accurately create a certain field shape for a given application (26),
4. finding a suitable strategy to switch between different configurations obtained by step 3 within an imaging pulse sequence or between the pulse sequences for different applications or imaging regions,
5. finding excitation (27), signal conditioning (28), and sampling (15) strategies that optimally use the flexibility provided by the matrix coil.

Although the latter task does not strictly belong to the coil design, it provides the initial motivation as well as the valuable feedback to the entire chain, and in particular to step 4, as the different imaging applications mentioned demand for switching between several varying field shapes. The present paper concerns itself primarily with step 4 from the above listing and builds on top of step 3 which was addressed in previous work (26).

Although the matrix gradient coil design in (2) aimed at maximum flexibility in creating a wide variety of field shapes to assess the advantages and disadvantages of this approach, future coils could be specifically designed for a certain range of applications or use cases. One example for a matrix gradient coil specifically designed for high gradient strength with acceptable switching rates, as required for high b-factor diffusion imaging, are the linear gradient coils of the Human Connectome Project (29), which use 4 independent coil elements per linear gradient axis and are driven by a total of 12 amplifiers. Apart from imaging, matrix coils or multi-coils can be used for B_0 shimming and both imaging and B_0 shimming at the same time (30). Although shimming requires only low current and therefore relatively low-cost power supplies, encoding requires substantial currents, which necessitates powerful and therefore expensive amplifiers. For shimming, each coil element can be driven by an individual amplifier (4, 3), but for imaging applications, which is the focus of this work, it is desirable to keep the number of amplifiers as low as possible.

In an earlier work (26), we presented a method to use the matrix gradient coil with fewer amplifiers than coil elements. When using fewer amplifiers than coil elements, the coil elements are distributed over the available amplifiers such that several coil elements are assigned to a single amplifier. All coil elements assigned to a certain amplifier are connected in series and supplied with the same current from the corresponding amplifier. The coil elements assigned to a single amplifier are termed a *cluster*, and a set of N_A clusters is called a *configuration*, where the number of amplifiers is defined as N_A. In our previous work, we have shown how such a configuration can be optimized by assigning coil elements to clusters such that a desired target field shape can be approximated with high accuracy. We have shown that this combinatorial optimization problem can be solved such that even with a reduced number of amplifiers, a large range of field shapes can be created accurately. For instance, for an 84-channel coil and only 12 amplifiers, it was possible to create spherical harmonics up to third order with a median normalized least squares error of $\sim$5%. With $\geq$24 amplifiers, the median normalized least squares error reduces to $\approx$2.5%, while it increases to $\approx$10% for 6 amplifiers. Note that a configuration creates the desired target field with a particular ratio of the currents supplied by the amplifiers. In principle, this restriction can be lifted by changing the ratio to create a wide range of different field shapes with a single configuration. This means that in practice, each configuration is more powerful than what it was optimized for; however, exploitation of this degree of freedom requires further investigation in future work. Details of the implementation and the performance analysis of the solver are presented in Kroboth et al. (26, 31). In Kroboth et al.'s study (26), each configuration was optimized to create a single target field; however, typical imaging applications require the application of several distinct encoding fields, where each generally corresponds to a different configuration. Different encoding fields usually require different configurations; therefore, to switch between encoding fields, a mechanism is required to switch between configurations. Essentially, this means opening and closing connections between coil elements, depending on the requirements of the desired configuration. This can be achieved via a so-called switching circuit (32), which can be cast into the epoxy resin together with the matrix gradient coil. If space limitations become a problem, the circuit can be located outside the coil. An example of such an approach, which relies on a dense switching network, was proposed recently for B_0 shimming and is termed *dynamically controlled adaptive current network* (33). In such a network—owing to a

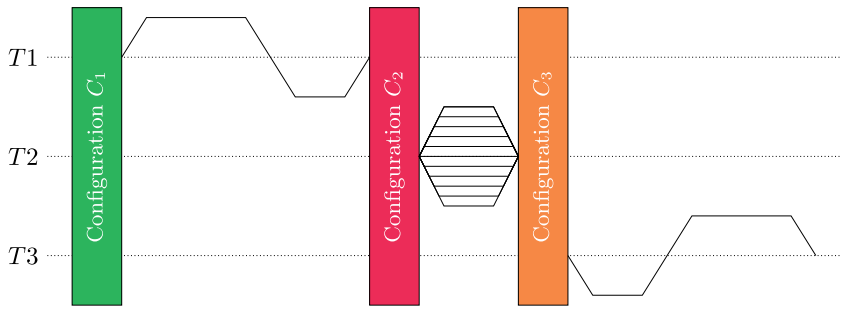

Figure 1. A potential pulse sequence with 3 distinct target fields T1, T2, and T3, each created by a corresponding configuration consisting of N_C coil elements and driven by N_A amplifiers (where the ratio of all currents is predefined). Because configurations differ for different target fields, the sequence requires a mechanism to switch between different configurations. This can be achieved with a switching circuit. Changing the state of the switches requires <10 μs. This example shows 3 target fields; however, the number (and shape) of the target fields can be arbitrary. Note that by changing the ratio of the currents supplied to the individual clusters, other target fields can be created, which were not part of the optimization process of the configurations. Therefore, the actual capabilities of such a setup are much larger than this figure may suggest at a first glance.

particularly simple geometry of the B_0-contributing elements, which are straight wire segments orthogonal to the B_0 direction—a 2D network of metal–oxide–semiconductor field-effect transistor (MOSFET) switches connecting each element to its neighbors and a single amplifier is sufficient to realize any discrete current path. However, the achievable surface current density in such a network is not sufficient for imaging applications requiring strong local gradients. Therefore in our research, we focus on multiturn element geometries. A switching circuit for the available 84-element matrix gradient coil, in its straightforward implementation, can be designed to connect every terminal of a coil element to all terminals of every other coil element. In addition, every terminal of each coil element has to be connected with every terminal of every amplifier. This hypothetical switching circuit would allow for arbitrary current paths through a network of coil elements. By changing the state of the individual switches, every configuration can be realized, allowing for sequences such as the one illustrated in Figure 1, where the configuration for the next encoding field can be switched at zero-current conditions. Unfortunately, this would require 18 060 switches for the case of $N_C = 84$ coil elements and $N_A = 12$ amplifiers, as the number of switches necessary to connect all coil element terminals to each other is given by $N_C \cdot (2 \cdot N_C - 1) = 14028$, and the number of switches necessary to connect all amplifier terminals to all coil element terminals is given as $4 \cdot N_C \cdot N_A = 4032$. Not only is this technically infeasible owing to the complexity of the network and the dimensions of the individual switches, it is also potentially prohibitively expensive owing to the requirements on the switches (high currents, fast switching times). In this work we use the property that if a finite set of configurations to be switched is known *a priori*, a full switching circuit is not necessary. For instance, connections that are connected in all configurations can be hard-wired (no switch required), and connections that are not present in any configuration do not require a switch (and no hard-wiring). Only connections that are closed in some but not all configurations require a switch. The same applies to the switches that connect the amplifiers to the coil element network. The number of required switches depends on the configurations and the ordering of elements within a cluster. There are numerous switching circuits for a given set of configurations that are all capable of switching between the configurations.

We propose an optimization algorithm that finds, in the set of all possible switching circuits, one which requires a low number of switches for a given set of configurations. We exploit the fact that the ordering of coil elements within a cluster does not change its electromagnetic properties owing to the fact that the elements are connected in series and that any amplifier can supply any cluster (assuming that the amplifiers have equal specifications). In our model, the coil elements are characterized

by individual resistances and an inductance matrix and we further assume perfect switches. The configurations are designed before the optimization of the switching circuit, for instance, by the method introduced in Kroboth et al.'s study (26). *Note that the optimization procedure presented in this work does not affect the magnetic field created by the given configuration.* The coil design (2) used in this work is a cylindrical head-insert with a length of 70 cm and an inner diameter of 39 cm. It consists of 84 coil elements (6), distributed on 7 rings with 12 elements each (Figure 2A). In line with a previously published work (26), we assume that each coil element is equipped with a bridge consisting of 4 switches (Figure 2B). This allows for the current to be routed through the coil winding in both directions. Throughout this work, we treat the bridge as an integral part of each coil element. The method presented here is also applicable to other matrix gradient coil or multi-coil designs. Ideally, the problem presented in this work would be optimized jointly with the optimization of the configurations. However, as both problems are combinatorial and as the joint optimization would have multiple objectives, this was considered intractable given the currently available computational power.

METHODOLOGY

Theory

Minimizing the number of switches for a given set of configurations can be split into 2 combinatorial NP-hard (nondeterministic polynomial-time hardness) optimization routines which are executed sequentially. The first minimizes the number of switches between coil element terminals, then, based on the result, the second minimizes the number of switches which connect the amplifiers to the matrix coil. The used variables are summarized in Table 1.

Minimizing the Number of Switches Between Coil Elements. The problem of reducing the number of switches between the elements is a distant relative of the well-known traveling salesman problem (TSP) (34), where a salesman aims at visiting several cities in minimum time or minimum travelled distance. However, here we have N_F companies (configurations C_k, where $k = 1, \ldots, N_F$), each employing N_A salesmen (amplifiers). Each company assigns N_C cities (coil elements) to its salesmen such that all cities are assigned and every city is assigned exactly once for each company. Given such a setup, the aim is to find a path for each salesman such that the total number of streets (connections) between cities (coil elements) and the number of necessary junctions (switches) are minimal.

A configuration defines how coil elements are grouped into clusters. Each cluster is a set of coil elements that are all supplied with the same current. When implementing a configuration, all coil elements of a cluster are therefore connected in series in an arbitrary order and supplied with current by a single amplifier. For each configuration, there is a graph that models how coil elements are connected. The ordering of elements within a cluster does not change the electromagnetic properties of the cluster (and hence the configuration); however, ordering does change the associated graph. This means that changes to the ordering do *not* affect the ability of the configuration to create a certain target field at a certain accuracy and field strength. Let C_k be the k^{th} of N_F configurations, which is optimized to create a certain target field T_k. Furthermore, let X be a variable that indicates how coil elements within the clusters are ordered for all k. Then there is an associated adjacency matrix $A(C_k, X)$ that indicates which terminals of the coil elements are connected with each other for the configuration C_k given the ordering X. The adjacency matrix contains the terminals of the coil elements, which allows us to account for polarity. Therefore, the size of $A(C_k, X)$ is $2N_C \times 2N_C$. Furthermore, let $\Sigma(X, G)$ be the sum of a set of N_F general adjacency matrices $G(C_k, X)$:

$$\Sigma(X, G) = \sum_{k=1}^{N_F} G(C_k, X). \tag{1}$$

The nonzero entries of $\Sigma(X, G)$ indicate connections. Let $\sigma^{i,j}(X, G)$ be the element of $\Sigma(X, G)$ in the i^{th} row and the j^{th} column. Every entry where $\sigma^{i,j}(X, G) = N_F$ indicates a hardwired connection because this connection exists for every configuration in case of the ordering X; therefore, there is also no switch required. Finally, the number of necessary switches is given by the following equation:

$$s(\Sigma(X, G)) = \sum_{i,j;j<i} \begin{cases} 0 & \text{if} \quad \sigma^{i,j}(X, G) = 0 \\ 0 & \text{if} \quad \sigma^{i,j}(X, G) = N_F \\ 1 & \text{else} \end{cases}. \tag{2}$$

Applying equation (2) to the adjacency matrices $A(C_k, X)$ serves as the cost function for the optimization problem as follows:

$$X^* = \underset{X}{\operatorname{argmin}} \{ s(\Sigma(X, G)) \}. \tag{3}$$

For optimization, the following degrees of freedom can be exploited, which are reflected in X:

- The order in which the elements are connected within a cluster can be arbitrary.
- Each element is equipped with a bridge consisting of 4 switches that allow current to be routed through the element in both directions (Figure 2B). Hence every element can be connected in both orientations provided the current direction in the coil windings is adapted accordingly by using the bridge switches.

To change X, either the ordering of elements within a cluster can be changed or the direction in which a coil element is connected. Changing X affects the individual adjacency matrices $A(C_k, X)$, which furthermore affects $s(\Sigma(X, A))$.

Figure 3 illustrates this principle using a toy example with a matrix gradient coil with $N_C = 4$ coil elements (E1, E2, E3, E4), $N_A = 2$ amplifiers, and $N_F = 3$ configurations.

Minimizing the Number of Switches from the Amplifiers to the Coil Element Network. Once a favorable ordering of coil elements is obtained, the number of necessary switches from the terminals of the amplifier to the entry and exit terminals of the individual clusters of all configurations can be minimized. Let $B(C_k, Y)$ be adjacency matrices that indicate the connections between amplifiers and clusters of configuration C_k given Y that defines which amplifier is assigned to which cluster. Using equations (1) and (2) with the adjacency matrices $B(C_k, Y)$, the global optimizer Y^* can be obtained via the following equation:

$$Y^* = \underset{Y}{\operatorname{argmin}} \{ s(\Sigma(Y, B)) \}. \tag{4}$$

Under the assumption that all amplifiers have equal properties and that they can adapt to the actual load, it is irrelevant which cluster is driven by which amplifier. Furthermore, the positive and negative terminals of the amplifier can be connected to either the entry- or exit-terminal of a cluster because the am-

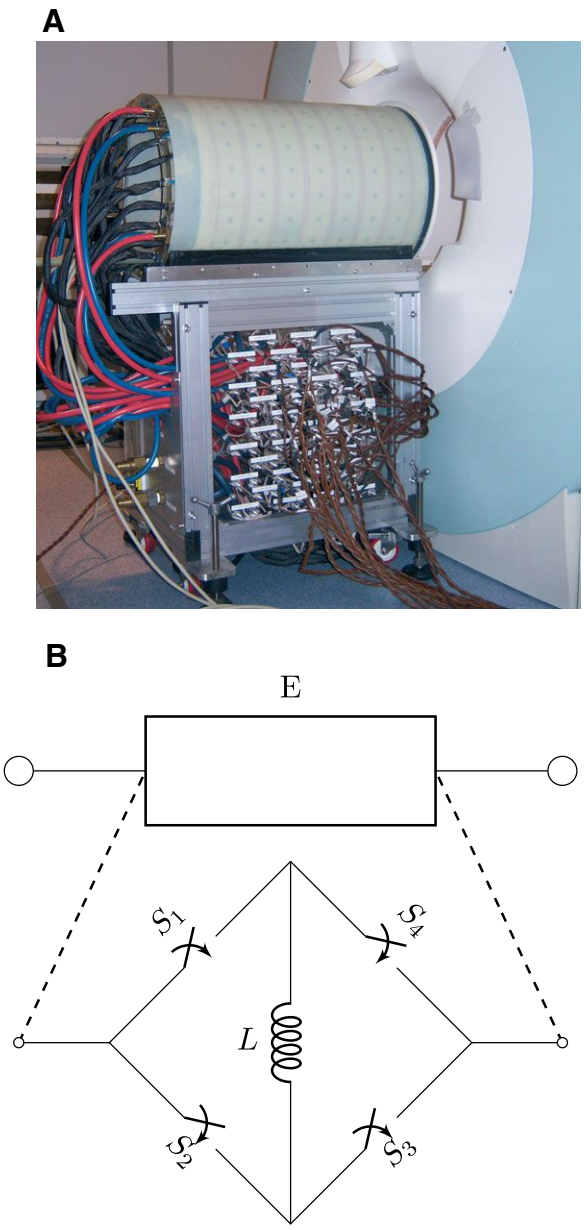

Figure 2. Implementation of the matrix gradient coil shown at the backside of a Siemens Trio scanner (A). To conduct measurements, the coil is pushed into the isocenter of the scanner. The black connections feed current to the individual coil elements. The water cooling is supplied by the red and blue hoses. On the side of cart are connector boards with connections for every coil element. A schematic representation of a coil element E which consists of the coil windings L equipped with a bridge switch (B). This allows to route current through the element in both directions. One direction is achieved by having the switches S_1 and S_3 in on-state and S_2 and S_4 in off-state. The other direction is achieved the other way around. In addition, the bypass mode can be achieved by having control switches S_1 and S_4 in on-state and switches S2 and S3 in off-state, or the other way around.

Table 1. List of Variables

Variable	Explanation
E1	Coil element 1
S_1	Switch 1
Amp1	Amplifier 1
p_1^2	Terminal 2 of coil element E1
N_A	Number of amplifiers
N_C	Number of coil elements
N_F	Number of fields
N_D	Number of different (random) configurations
N_R	Number of repetitions (optimization algorithm runs)
T_k	Target field k
C_k	Configuration k
X, Y	Orderings
$G(C_k, X)$	General adjacency matrix for a configuration C_k and an ordering X
$A(C_k, X)$	Adjacency matrix for the connections between coil element terminals
$B(C_k, Y)$	Adjacency matrix for the connections between coil element terminals and amplifier terminals
$\Sigma(X, G)$	Sum of adjacency matrices
$\sigma^{i,j}(X, G)$	Element (i, j) of sum of adjacency matrices $\Sigma(X, G)$
$s(\Sigma(X, G))$	Number of switches for $\Sigma(X, G)$
T^i	Temperature at iteration i (Simulated Annealing)

plifiers are bipolar and therefore the direction of the current can be changed. These degrees of freedom are exploited to minimize the number of switches that connect the amplifiers to the coil element network. The concept is illustrated in Figure 4, where changing how amplifiers are assigned to the network of coil elements leads to an ordering that requires 2 fewer switches.

Matrix Gradient Coil and Other Hardware

The algorithm is applied to the matrix gradient coil design introduced in Littin et al.'s study (2). The gradient coil design dictates the basic conditions for optimization such as the number of coil elements; however, in principle, the presented method can be applied to any matrix gradient coil or multi-coil design. For the given coil, eddy currents are $<1\%$ of the original field owing to the use of Litz wire, shielded element design, and a substantial distance to the cryovessel. They can therefore be ignored for most applications. Mutual coupling has been assessed in Littin et al.'s study (2). Both eddy currents and mutual coupling are ignored in the present work because they are not affected by any of the operations performed during the optimization. The amplifiers further impose restrictions, owing to the limitations regarding the load. This is considered via the maximum and minimum number of coil elements per amplifier in the optimization of the configurations as shown in Kroboth et al.'s study (26). The amplifiers used to drive the matrix gradient coil can be adapted to load changes. Therefore the amplifiers need to

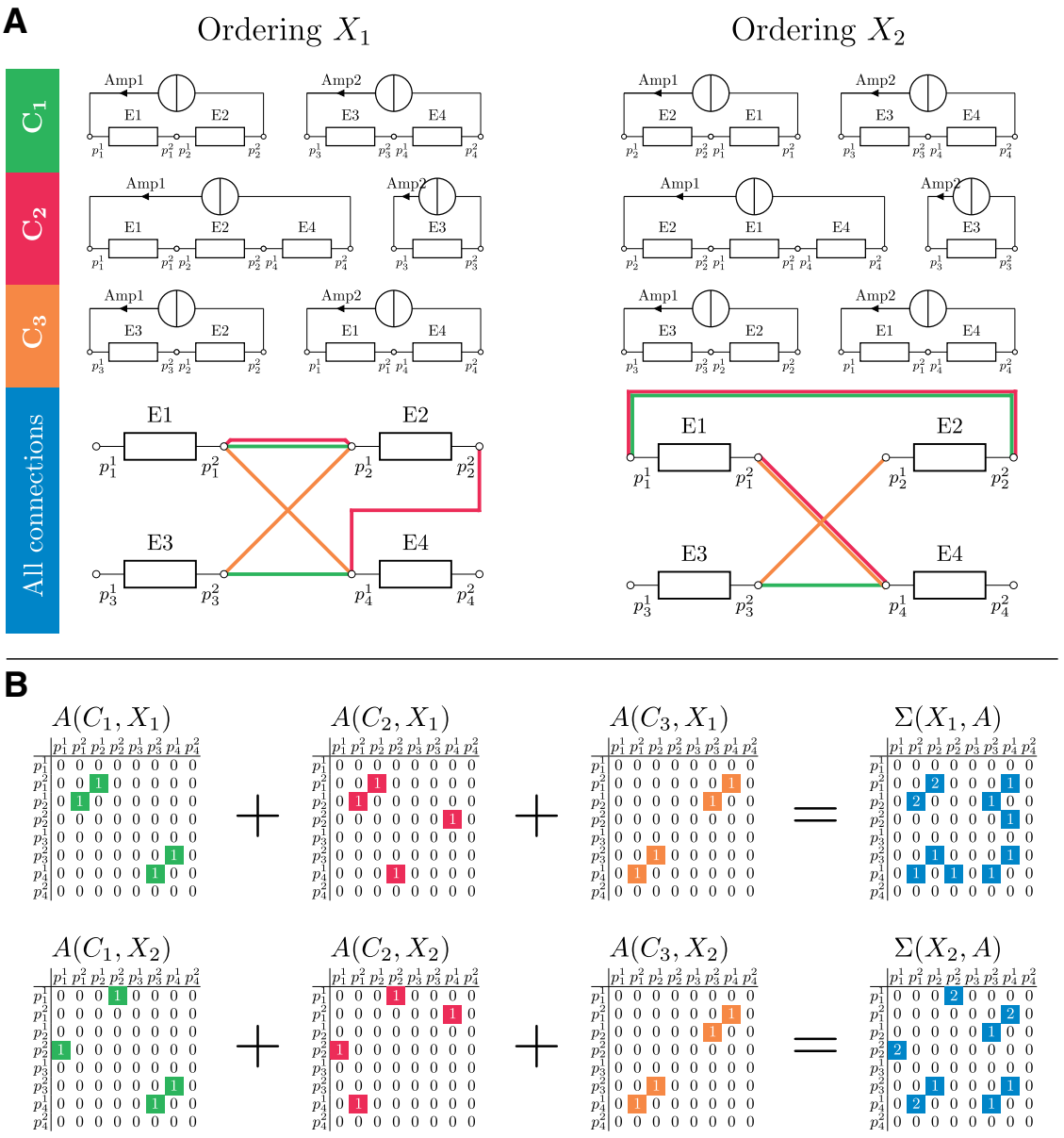

Figure 3. (A) Illustration of how changing the ordering of coil elements within a cluster can affect the number of switches for a matrix gradient coil with 4 coil elements (E1, E2, E3, E4; each box represents a circuit as shown in Figure 2B), 2 amplifiers (Amp1, Amp2), and $N_F = 3$ configurations (C_1, C_2, C_3). (B) The initial ordering X_1 and the updated ordering X_2 are shown in the left and right columns, respectively. The first 3 rows show how the coil elements are assigned to and supplied by amplifiers to create the N_F target fields. The fourth row summarizes all connections between coil elements for each setup. Terminals are labeled with the symbol p. Observe that in C_1 the ordering of E1 and E2 changes in the first cluster, whereas in C_2 the ordering of E1, E2, E4 changes to E2, E1, E4. Configuration C_3 remains unchanged. As can be seen in the last row, X_1 has only 1 connection between terminals which is used by 2 configurations, whereas X_2 has 2 shared connections. While the ordering X_1 requires 5 switches, the ordering X_2 requires only 4 switches. Corresponding adjacency matrices of the undirected graph representing 2 configurations, X_1 (top) and X_2 (bottom). Each nonzero entry represents a connection between 2 terminals of the coil elements. Applying equation (2) to each of the 2 adjacency matrices (X_1; A) and (X_2; A) gives the final number of switches, which is 5 for X_1 and 4 for X_2. Similar strategies can be followed for the switches connecting the amplifiers to the coil element network (Figure 4).

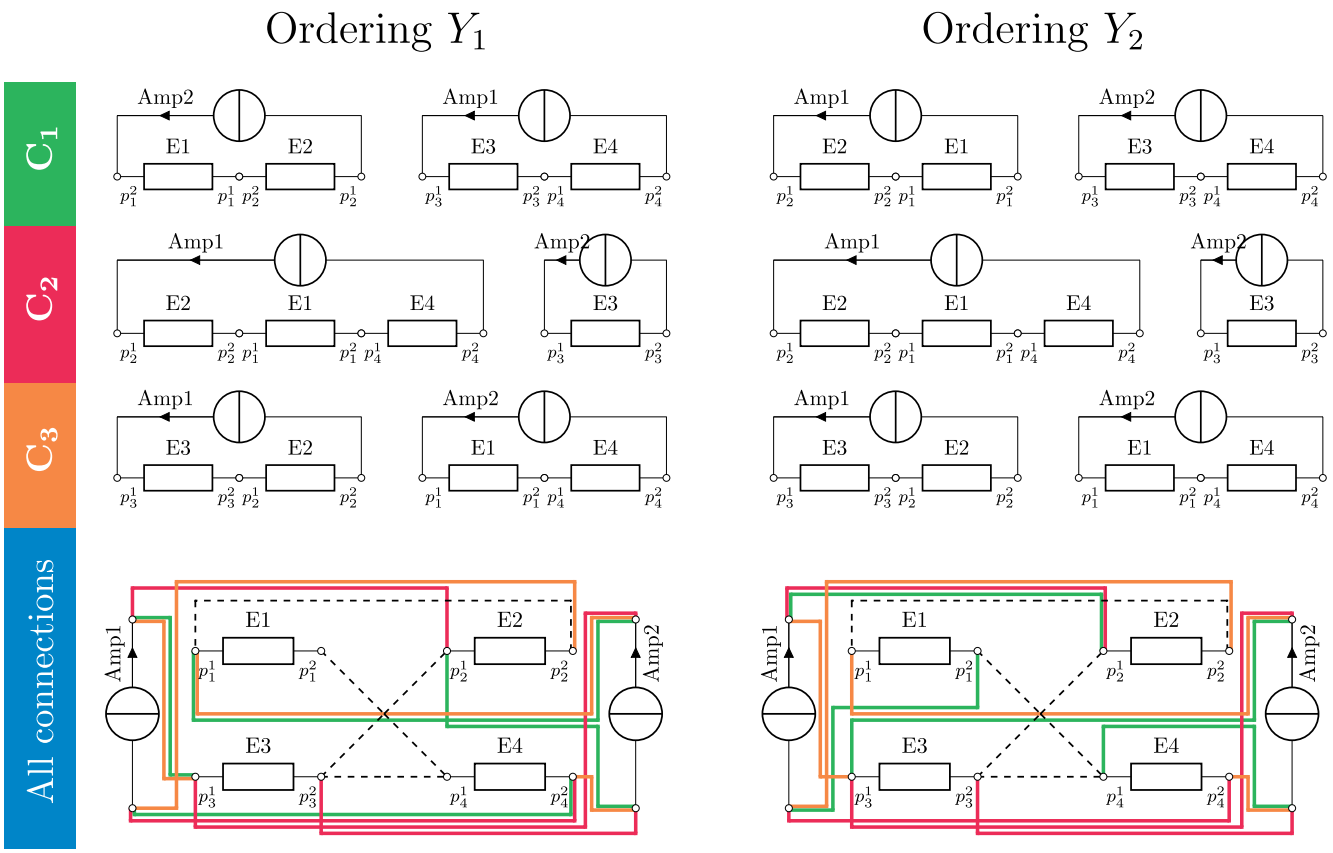

Figure 4. This figure illustrates possible moves taken in the optimization of the switches connecting the amplifiers to the coil element network. The configuration Y_1 is equivalent to the configuration X_2 of Figure 3. The difference between Y_2 and Y_1 is that in configuration C_1, Amp1 is connected the other way around. Note that the terminals of E1 and E2 are still connected in the same way as in Y_1. In addition, in configuration C_2, the amplifiers are swapped such that Amp2 now powers the first cluster and Amp1 the second cluster. None of the possible moves this optimization can perform can influence the result of the previous optimization illustrated in Figure 3. The final row shows all connections for the different configurations. For this toy example, the maximum number of switches is 12. The ordering Y_1 has 3 shared connections (from terminal 1 of Amp1 to p_2^1, from terminal 1 of Amp2 to p_3^1, and from terminal 2 of Amp2 to p_4^2). Owing to 3 shared connections, the ordering number of switches reduces to 9. In Y_2, there are again 3 shared connections (from terminal 1 of Amp1 to p_3^1, from terminal 1 of Amp2 to p_3^1, and from terminal 2 of Amp2 to p_1^1 of E1 p_4^2). The connection from Amp2 to p_4^2 is special, as this is wired for every configuration, meaning that there is no switch necessary, and instead, it can be hard-wired. In total, the number of switches for Y_2 reduces to 7.

be reprogrammed whenever the load changes during switching. Switching is performed at zero current conditions only (32).

Algorithm

The optimization problems addressed in this work [equations (3) and (4)] are combinatorial and NP-hard. Performing an exhaustive search over the parameter space is too expensive for practical use. For instance, consider the optimization of a switching circuit that is designed to switch between 3 configurations given a 84-channel coil and 12 amplifiers (where for simplicity, the coil elements are equally distributed amongst the amplifiers). This would require the evaluation of $(((84/12)!)^{12})^3 \approx 2{\cdot}10^{133}$ different orderings for the minimization of the number of switches in between coil terminals alone. This number is given by $(84/12)! = 7!$ possible orderings of coil elements within a single cluster to the power of the number of clusters/amplifiers ($N_A = 12$) and finally to the power of the number of fields ($N_F = 3$). This calculation does not even consider the bridge switches, which would further increase the number of necessary evaluations. The additional complexity owing to the nonconvex and multimodal (many local minima) nature of the optimization problems further aggravates finding the global minimizer with conventional gradient-based methods. Therefore a probabilistic metaheuristic called simulated annealing (SA) (35) is used to find a (local) minimum. This iterative and stochastic optimization method is inspired by the annealing of metals, where the metal is heated to a certain temperature and then cooled down according to a schedule. The energy state of the resulting crystals strongly depends on the initial temperature and the cooling schedule. These ideas can be transferred to optimization prob-

Algorithm 1. Annealing Function 1

```
for j < ⌊T^i⌋ + random_integer(1, 5) do
    C_r ← random configuration
    K_r ← random cluster in C_r
    e_1 ← random element index 1 in K_r
    e_2 ← random element index 2 in K_r
    if random(0,1) > 0.5 then
        X^i ← swap_elements(X^i, e_1, e_2)
    else
        X^i ← flip_element_orientation(X^i, e_1)
    end if
    j ← j + 1
end for
Return X^i
```

Algorithm 2. Annealing Function 2

```
for or j < ⌊T^i⌋ + 1 do
    C_r ← random configuration
    v_1 ← random amplifier index 1
    v_2 ← random amplifier index 2
    if random(0, 1) > 0.5 then
        Y^i ← swap_amplifiers(Y^i, C_r, v_1, v_2)
    else
        Y^i ← flip_amplifier_orientation(Y^i, C_r, v_1)
    end if
    j ← j + 1
end for
Return Y^i
```

lems, where instead of metals, parameter vectors are "heated up" to a temperature T^0, and then cooled down by reducing the temperature over the course of the iterations. The parameter vectors are randomly modified in each iteration by a degree proportional to the temperature. These modifications (sometimes also called *moves*) are performed by a problem-specific *annealing function*. After every iteration, the temperature is reduced according to a cooling schedule. The cooling schedule used in this work is T^0/i, where i is the current iteration number, which has worked well during our simulation experiments. This means that in early iterations with high temperature, the parameter space will be explored randomly by performing big "jumps," while later iterations with lower temperature will focus on improvements in close proximity to the current position of the parameter vector in the parameter space. The quality of every parameter vector is calculated by the so-called *cost function*. Better solutions are always accepted; however, worse solutions may also be accepted with a probability given by $P = 1/(1 + \exp(\delta/T))$, where δ is the absolute difference of the previous and current cost function value. This is beneficial for overcoming local minima. The acceptance probability increases with temperature and small δ. When the current best cost function value has not improved for N_{SAmax} iterations, we consider it converged and stop the optimization. Note that this method is not guaranteed to find the global optimum.

Annealing Function

The annealing function defines how a parameter vector is modified in each iteration of the SA algorithm. It depends on the temperature T^i of iteration i. If the temperature is high, more modifications will be performed. In the case of minimizing the number of switches between coil elements (Algorithm 1), the annealing function randomly performs 1 of 2 operations with the same probability. It either picks 2 random elements within a randomly chosen cluster of a randomly chosen configuration and swaps them to change the ordering or reverses the polarity of a randomly chosen coil element (which can be accounted for in the actual implementation of the circuit by adapting the state of the switches of the corresponding bridge switch). This step is repeated several times depending on T^i.

When minimizing the number of switches from the amplifiers to the coil element network, the annealing function (Algorithm 2) randomly changes how amplifiers are assigned to clusters within randomly chosen configurations. In other words, within a configuration, the positions of some of the amplifiers in the network are randomly permuted as this may affect the number of switches. The concept is illustrated in Figure 4 using a toy example, where swapping amplifiers Amp1 and Amp2 in configuration C_2 and changing the direction how Amp1 in C_1 is connected to the first cluster reduced the number of necessary switches by 2. The number of times this procedure is repeated depends again on the temperature.

Optimization Settings

To assess the performance of the optimization algorithm, randomly generated configurations were used. The configurations were generated for $N_F = \{3, 9, 15, 21, 27\}$ (number of fields) and $N_A = \{6, 12, 24, 36, 42\}$ (number of amplifiers/clusters). The range of the number of fields is not based on specific applications, but it was chosen to cover a large range with equidistant spacing. All configurations are based on a matrix gradient coil with $N_C = 84$ coil elements. For each setting, $N_D = 100$ random configurations were created. Each optimization is run for $N_R = 4$ times to account for the statistical nature of the solver. For creating the random configurations, the minimum and maximum numbers of coil elements per amplifier are set to $N_{Cmin} = 2$ and $N_{Cmax} = 15$, respectively. This large amount of randomly created configurations covers a large range of possible cases and is used here as a means to assess the performance of the algorithm. Note that these randomly created configurations are likely to not produce useful magnetic fields. In addition, the algorithm has been tested on a subset of the (realistic) configurations obtained in Kroboth et al.'s study (26) for an $N_C = 84$ channel matrix gradient coil. These configurations where designed for $N_A = \{6, 12, 24, 42\}$ (number of amplifiers/clusters) to create spherical harmonics up to full third order (15 fields). Here we optimize a switching circuit for the first 3, 9, and 15 configurations. The number of configurations were chosen

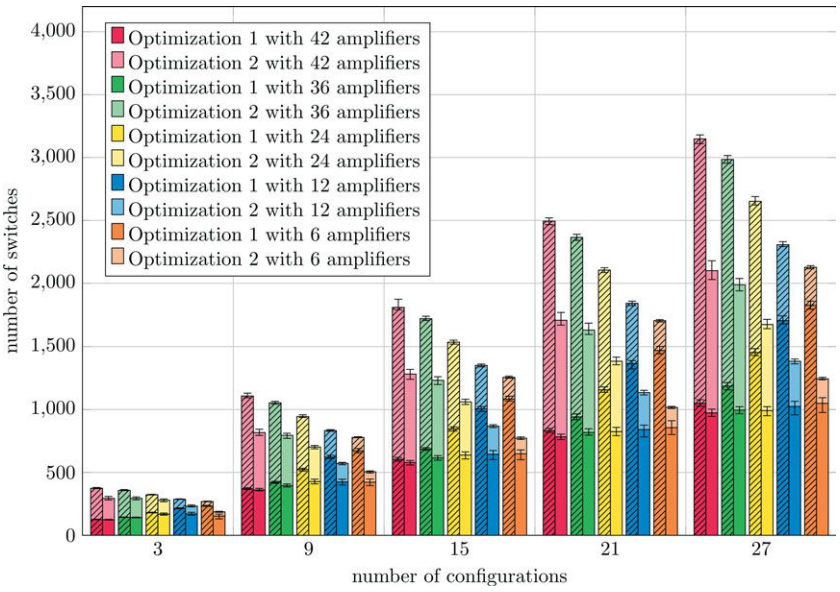

Figure 5. Comparison of the unoptimized (hatched bars) with the optimized case. The mean values of the number of switches between coil elements (before and after optimization 1) and the number of switches from the amplifiers to the coil elements (before and after optimization 2) are stacked to show the total number of switches. Different setups (3 to 27 configurations and the number of amplifiers ranging from 6 to 42) were evaluated. Per bar, 100 random configurations were created where each configuration uses all 84 coil elements. Each optimization instance was run 4 times, therefore the total number of data sets per bar is 400. The variation over all runs is indicated with error bars.

such that the results are comparable to the results obtained with the random configurations (they do not correspond to the number of basis functions contained in certain orders of spherical harmonics). For all runs, the initial temperature was set to $T^0 = 10^4$, and the maximum number of iterations where the best cost function value has not changed was set to $N_{\mathrm{SAmax}} = 2{\cdot}10^4$ (stopping criterion). These parameters were experimentally found to obtain good results. The software has been implemented in the Matlab (The MathWorks, Natick, MA) programming language using Matlab's Global Optimization Toolbox. Each optimization was executed on a single CPU core without parallelization.

RESULTS

Combinations of different hardware setups with a large range of numbers of configurations have been investigated. Figure 5 shows the comparison between the unoptimized and optimized cases for randomly generated configurations. Each bar includes 100 different optimization instances where each is run 4 times, leading to a total of 400 data points per bar. As it would not be fair to compare the optimized switching circuit to the full switching circuit, the optimized circuits are compared with the unoptimized switching circuit. The unoptimized switching circuit is based on the ordering given by the method that produces the configurations. In case of the random configurations, the initial, unoptimized ordering of coil elements within clusters and the assignment of amplifiers to the coil element network is random. For the realistic configurations, the optimization algorithm of Kroboth et al.'s study (26) does not consider the ordering of the coil elements within clusters and the assignment of amplifiers to the network; therefore, the ordering can also be considered random. Note that therefore the unoptimized case is rather an average case than a worst-case scenario.

Optimization 1—Switches Between Coil Elements

As expected, the number of required switches increases with the number of configurations that are to be switched. This is because the number of different pathways through the coil element network increases with the number of configurations. The switching circuit needs to be able to realize all these pathways, which in general, comes with the need to increase the number of necessary switches. For the investigated range of configurations, the number of switches after optimization ranges from ≈200 switches (3 configurations) to ≈1000 switches (27 configurations). The influence of the number of amplifiers (which is equal to the number of clusters, as each amplifier is connected to a cluster) is rather small, at least for the optimized case. In the unoptimized case, fewer amplifiers/clusters lead to an increase in the number of switches. The optimization however is capable of reducing this substantially, see, for instance, the case of 15 configurations and 6 amplifiers. In comparison, for a large number of amplifiers (ie, 15 configurations and 42 amplifiers), the optimization only leads to a small reduction. This suggests that the number of configurations to be switched is the dominating factor in terms of number of switches between coil elements, while the actual composition of the individual configurations plays a minor role.

Optimization 2—Switches Between Amplifiers and Coil Elements

The results of this part also depend on the number of configurations; however, this time there is also a pronounced depen-

dency on the number of amplifiers: more amplifiers require more switches. However, the reduction of switches from unoptimized to optimized suggests that the more amplifiers, the higher is the potential for minimization, as there are more degrees of freedom to exploit. This means that this optimization is more effective for a large number of amplifiers, but effectively, a lower number of amplifiers leads to fewer necessary switches. Over all investigated data sets, the number of switches between amplifier and coil element terminals after optimization ranges from ≈30 to slightly over ≈1130.

Combined Results of Optimizations 1 and 2

For a given number of configurations, it is favorable to have a low number of amplifiers. However, from the results in Kroboth et al.'s study (26), we know that for a low number of amplifiers, it is in general more difficult to obtain a configuration which is capable of accurately creating a desired target field. This is because lowering the number of amplifiers essentially limits the number of different current values flowing through the coil and hence restricts the coil's capabilities to accurately reproduce target fields. Therefore, the number of amplifiers is usually dictated by the desired field accuracy in the optimization of the configurations, as shown in Kroboth et al.'s study (26). The optimization algorithms themselves perform best for a low number of amplifiers, leading to a reduction (compared to the unoptimized case) ranging from ≈8% to ≈44%. The average reduction across all investigated data sets is ≈31%.

Realistic Configurations

The algorithm has furthermore been tested on a subset of the configurations obtained in Kroboth et al.'s study (26). These configurations were designed such they are able to create spherical harmonics up to full third order for 6, 12, 24, 42 amplifiers. The median least squares error of all 15 configurations compared with the desired target fields was ≈10% for 6 amplifiers, ≈5% for 12 amplifiers, and ≈2.5% for ≥24 amplifiers (including all 84 channels driven individually). Figure 6 shows the results for switching circuits optimized to switch between the first 3, 9, and 15 configurations. These results are in line with the results shown in Figure 5. This affirms the assumption that in practice, the number of switches depends stronger on the hardware setup such as the number of amplifiers and the number of configurations than on the actual composition of the configuration.

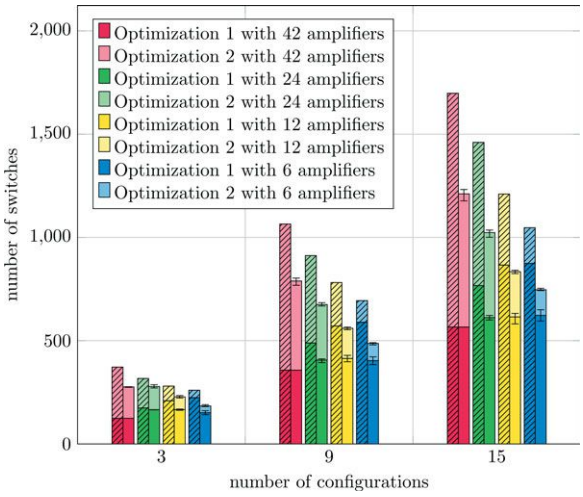

Figure 6. Comparison of the unoptimized case (hatched bars) with the optimized case for the first 3, 9, and 15 configurations published in Kroboth et al.'s study (26). Each optimization instance was run 100 times to account for the statistical nature of the solver. The variation of these runs is indicated with error bars. The general trends match Figure 5.

DISCUSSION

Many parameters require consideration when designing a matrix gradient coil. Mainly, the coil should be suitable for the task at hand, but also the technical effort and costs associated with it cannot be neglected. The parameters that influence the coil's capabilities and technical effort are (among others) the number of coil elements, the number of amplifiers, and the complexity of the switching circuit. This work in combination with Kroboth et al.'s study (26) aims to shed light on the relationship between those parameters in terms of both technical effort and ability to create fields. In Kroboth et al.'s study (26), we showed (in case of the matrix gradient coil) that even with a reduced number of amplifiers, a large range of field shapes can be created accurately. Here we extend the previous work by showing how the number of switches needed for a switching circuit can be reduced. By changing the order of coil elements within clusters and by varying which amplifier supplies which cluster of a configuration with current, we were able to reduce the number of switches by up to ≈44% without affecting the configurations' ability to create a target field at a desired accuracy. Many random configurations were used to assess the algorithms on a wide range of different situations. To address the statistical nature of the optimization algorithms, each instance was optimized 4 times. In addition, a subset of the configurations optimized in Kroboth et al.'s study (26) was used to show the performance of the algorithms on a realistic setup. The problem of minimizing the switches was split into 2 sequential optimization problems. At first, given a set of configurations, the number of switches connecting the terminals of all the coil elements with each other is minimized. Based on the results, the number of switches that connect the amplifiers to the clusters is minimized. Both problems pose challenging combinatorial optimization problems, which were solved with the use of SA. In the early stages of development, the problem was also solved with a genetic algorithm (GA); however, initial tests showed that performance was similar compared with SA. Given that GA has substantially more parameters to tune, SA was chosen. With proper tuning, we expect that GA can outperform SA in terms of speed; however, finding the perfect tuning is difficult given that it is likely problem-dependent. One major advantage of GA is its potential ability to extensively explore the parameter space owing to cross-over. Similar effects can be achieved by high

initial temperatures and/or multiple runs of SA in parallel. Unfortunately, the solution space of the second optimization may, in principle, be constrained by the solution of the first in an unfavorable way. To avoid this, both problems can be solved in a single optimization problem. However, this problem is much more complex, and the results of a pilot study were consistently worse than that of the proposed methods (data not shown).

In addition to reducing the number of switches, the results of this work also expose the relationships between the number of configurations and the number of amplifiers. Figure 5 gives insight into how the complexity of the switching circuit scales with different hardware setups. Running both optimizations requires ≈30 minutes to ≈8 hours depending on the parameters. The biggest influence on the runtime is the number of configurations. Because switching circuits are not changed or modified often, these long run-times are acceptable. The proposed method operates on configurations only and is therefore independent of the actual matrix gradient coil design, as configurations can be computed for any design.

The resulting optimized numbers of switches in the range of ≈200 to ≈1200 may appear to be high. Indeed the gradient array method (24) allows to create one localized Z gradient, which is movable along the Z direction without the need for switches (but using 3 gradient amplifiers). It is currently unclear how many gradient channels and amplifiers would be required to extend this approach of moveable FOVs to 3 spatial dimensions. Contrary to that, the *dynamically controlled adaptive current network approach* (33), which was recently introduced for shimming, relies on a single current amplifier, but it requires a substantial number of switches. As noted by the authors, for a body-sized coil with 2-cm wire spacing, 6000 switches would be required. To achieve surface current densities comparable to that of the present matrix coil (2) the number of switches would increase to 25 000. Compared with that, the matrix coil setup with a switching circuit, capable of generating a full third-order spherical harmonic set, driven by only 12 amplifies and controlled by ≈900 switches, appears to be favorable for imaging applications. It is further to be noted that none of the clusters in any of the configurations contained >15 elements connected in series, which is advantageous with regard to the voltage drop and the power dissipation in the coil.

One potential future step could be combining the optimization of configurations (26) with the optimization of the switching circuit presented in this work. However, this would be a substantially harder optimization problem, which additionally has 2 objectives (field accuracy and number of switches). Alternatively the configuration optimization and switching circuit optimization could be merged partially. For instance by favoring configurations that offer good starting conditions for the switching circuit optimization. These conditions need to be defined, and their effectiveness and their feasibility have to be assessed in future work. In this current work, it was assumed that each coil element is equipped with a bridge (Figure 2B); however, not every element may require such a bridge. In future work, the switches of the bridges could be included into the optimization to further reduce the technical effort. Furthermore it was assumed that the amplifiers are bipolar which is common for gradient channels. With adaptions, the optimization could also be performed with unipolar amplifiers. This also remains part of further research.

The setup shown in Figure 1 does not allow for the superposition of fields created by different configurations; however, each configuration can potentially create many different field shapes by changing the currents through the individual clusters. Therefore there are many more degrees of freedom for encoding than this diagram may suggest. Theoretically, the switching circuit offers more paths through the network of coil elements than it is optimized for which can be exploited for the creation of fields. Unfortunately, finding all possible or reasonable paths is also a computationally complex problem and the obtained additional functionality most likely does not scale well with the invested effort.

Also the dynamically controlled adaptive current networks B_0-shimming method (33) can benefit from the methodology presented here. In the original approach, desired current patterns are approximated by a dense network of small wire paths connected with MOSFETs, leading to very high flexibility for the creation of a wide range of current densities, with many of them leading to similar field shapes. The method presented here may be used to sparsify the dense switch network by eliminating the switches that are irrelevant for effective field creation and hardwiring the connections that are persistent across the set of the relevant target fields. The methodology and results presented in this work can further serve as a valuable tool for the search of such tradeoffs by combining it with the various approaches from the literature (2, 4, 24, 33).

CONCLUSION

We presented a method which reduces the effort associated with a switching circuit for matrix gradient coils by minimizing the number of switches for a given set of configurations without affecting the configurations' ability to accurately create a desired target field. The results give insights in the relationship between the number of switches and different parameters, which are important for the design of matrix gradient coils.

ACKNOWLEDGMENTS

This work was supported by the European Research Council (ERC) under grant ERC-POC 755466 "mrSANE" and by the German Research Foundation (DFG) under grant ZA 422/6-1.

Disclosures: No disclosures to report.

Conflict of Interest: The authors have no conflict of interest to declare.

REFERENCES

1. Wintzheimer S, Driessle T, Ledwig M, Jakob PM, Fidler F. A 50-channel matrix gradient system: a feasibility study. In Proceedings of ISMRM; Stockholm, Sweden; 2010. p. 3937.
2. Littin S, Jia F, Layton KJ, Kroboth S, Yu H, Hennig J, Zaitsev M. Development and implementation of an 84-channel matrix gradient coil. Magn Reson Med. 2017; 79:1181–1191.
3. Juchem C, Umesh Rudrapatna S, Nixon TW, de Graaf RA. Dynamic multi-coil technique (DYNAMITE) shimming for echo-planar imaging of the human brain at 7 Tesla. Neuroimage 2015;105:462–472.
4. Juchem C, Nixon TW, McIntyre S, Rothman DL, de Graaf RA. Magnetic field modeling with a set of individual localized coils. J Magn Reson. 2010;204:281–289.
5. Juchem C, Green D, Graaf RA de. Multi-coil magnetic field modeling. J Magn Reson. 2013;236:95–104.
6. Jia F, Littin S, Layton KJ, Kroboth S, Yu H, Zaitsev M. Design of a shielded coil element of a matrix gradient coil. J Magn Reson. 2017;281:217–228.
7. Konzbul P, Sveda K, Srnka A. Design of matrix shim coils system for nuclear magnetic resonance. IEEE Trans Magn. 2000;36:1732–1735.
8. Hennig J, Welz AM, Schultz G, Korvink J, Liu Z, Speck O, Zaitsev M. Parallel imaging in non-bijective, curvilinear magnetic field gradients: a concept study. MAGMA. 2008;21:5–14.
9. Schultz G, Ullmann P, Lehr H, Welz AM, Hennig J, Zaitsev M. Reconstruction of MRI data encoded with arbitrarily shaped, curvilinear, nonbijective magnetic fields. Magn Reson Med. 2010;64:1390–1403.
10. Gallichan D, Cocosco CA, Schultz G, Weber H, Welz AM, Hennig J, Zaitsev M. Practical considerations for in vivo MRI with higher dimensional spatial encoding. MAGMA. 2012;25:419–431.
11. Gallichan D, Cocosco CA, Dewdney A, Schultz G, Welz A, Hennig J, Zaitsev M. Simultaneously driven linear and nonlinear spatial encoding fields in MRI. Magn Reson Med. 2011;65:702–714.
12. Schultz G, Gallichan D, Weber H, Witschey WRT, Honal M, Hennig J, Zaitsev M. Image reconstruction in k-space from MR data encoded with ambiguous gradient fields. Magn Reson Med. 2015;73:857–864.
13. Layton KJ, Gallichan D, Testud F, Cocosco CA, Welz AM, Barmet C, Pruessmann KP, Hennig J, Zaitsev M. Single shot trajectory design for region-specific imaging using linear and nonlinear magnetic encoding fields. Magn Reson Med. 2013; 70:684–696.
14. Testud F, Gallichan D, Layton KJ, Barmet C, Welz AM, Dewdney A, Cocosco CA, Pruessmann KP, Hennig J, Zaitsev M. Single-shot imaging with higher-dimensional encoding using magnetic field monitoring and concomitant field correction. Magn Reson Med. 2015;73:1340–1357.
15. Layton KJ, Kroboth S, Jia F, Littin S, Yu H, Zaitsev M. Trajectory optimization based on the signal-to-noise ratio for spatial encoding with nonlinear encoding fields. Magn Reson Med. 2015;104–17.
16. Stockmann JP, Ciris PA, Galiana G, Tam L, Constable RT. O-space imaging: Highly efficient parallel imaging using second-order nonlinear fields as encoding gradients with no phase encoding. Magn Reson Med. 2010;64:447–456.
17. Stockmann JP, Galiana G, Tam L, Juchem C, Nixon TW, Constable RT. In vivo O-Space imaging with a dedicated 12 cm Z2 insert coil on a human 3T scanner using phase map calibration. Magn Reson Med. 2013;69:444–455.
18. Tam LK, Galiana G, Stockmann JP, Tagare H, Peters DC, Constable RT. Pseudo-random center placement O-space imaging for improved incoherence compressed sensing parallel MRI. Magn Reson Med. 2015;73:2212–2224.
19. Wang H, Tam L, Kopanoglu E, Peters DC, Constable RT, Galiana G. Experimental O-space turbo spin echo imaging. Magn Reson Med. 2016;75:1654–1661.
20. Dispenza NL, Littin S, Zaitsev M, Constable RT, Galiana G. Clinical potential of a new approach to MRI acceleration. Sc Rep. 2019;9:1912.
21. Turner R. Gradient coil design: A review of methods. Magn Reson Imaging. 1993;11:903–920.
22. Lemdiasov RA, Ludwig R. A stream function method for gradient coil design. Concepts Magn Reson Part B Magn Reson Eng. 26B:67–80.
23. Poole M, Bowtell R. Novel gradient coils designed using a boundary element method. Concepts Magn Reson Part B Magn Reson Eng. 31B:162–175.
24. Smith E, Freschi F, Repetto M, Crozier S. The coil array method for creating a dynamic imaging volume. Magn Reson Med. 78:784–793.
25. Jia F, Schultz G, Testud F, Welz AM, Weber H, Littin S, Yu H, Hennig J, Zaitsev M. Performance evaluation of matrix gradient coils. MAGMA. 2016;29:59–73.
26. Kroboth S, Layton KJ, Jia F, Littin S, Yu H, Hennig J, Zaitsev M. Optimization of coil element configurations for a matrix gradient coil. IEEE Trans Med Imaging. 2018;37:284–292.
27. Weber H, Gallichan D, Schultz G, Cocosco CA, Littin S, Reichardt W, Welz A, Witschey W, Hennig J, Zaitsev M. Excitation and geometrically matched local encoding of curved slices. Magn Reson Med. 69:1317–1325.
28. Witschey WR, Cocosco CA, Gallichan D, Schultz G, Weber H, Welz A, Hennig J, Zaitsev M. Localization by nonlinear phase preparation and k-space trajectory design. Magn Reson Med. 2012;67:1620–1632.
29. Van Essen DC, Ugurbil K, Auerbach E, Barch D, Behrens TEJ, Bucholz R, Chang A, Chen L, Corbetta M, Curtiss SW, Della Penna S, Feinberg D, Glasser MF, Harel N, Heath AC, Larson-Prior L, Marcus D, Michalareas G, Moeller S, Oostenveld R, Petersen SE, Prior F, Schlaggar BL, Smith SM, Snyder AZ, Xu J, Yacoub E. The Human Connectome Project: A data acquisition perspective. 2012;62: 2222–2231.
30. Umesh Rudrapatna S, Fluerenbrock F, Nixon TW, Graaf RA de, Juchem C. Combined imaging and shimming with the dynamic multi-coil technique. Magn Reson Med. 2019;81:1424–1433.
31. Kroboth S, Layton KJ, Jia F, Littin S, Yu H, Zaitsev M. Optimization of matrix gradient coil switching for a limited number of amplifiers. In: Proceedings of ISMRM. ISMRM. Toronto, 2015.
32. Yu H, Huethe F, Littin S, Layton KJ, Kroboth S, Jia F, Hennig J, Zaitsev M. An improved design of multi-channel switching circuit for matrix gradient coil. In: Proceedings of ISMRM. ISMRM. Toronto, 2015.
33. Harris CT, Handler WB, Chronik BA. A new approach to shimming: the dynamically controlled adaptive current network. Magn Reson Med; 2014;71:859–869.
34. Applegate DL, Bixby RE, Chvatal V, Cook WJ. The Traveling Salesman Problem: A Computational Study. Princeton Series in Applied Mathematics. 2007;608.
35. Kirkpatrick S, Gelatt CD, Vecchi MP. Optimization by simulated annealing. Science. 1983;220:671–680.

TOMOGRAPHY® RESEARCH ARTICLE

Use of Indicator Dilution Principle to Evaluate Accuracy of Arterial Input Function Measured With Low-Dose Ultrafast Prostate Dynamic Contrast-Enhanced MRI

Shiyang Wang[1], Xiaobing Fan[1], Yue Zhang[1], Milica Medved[1], Dianning He[1,2], Ambereen Yousuf[1], Ernest Jamison[1], Aytekin Oto[1], and Gregory S. Karczmar[1]

[1]Department of Radiology, University of Chicago, Chicago, IL and [2]Sino-Dutch Biomedical and Information Engineering School, Northeastern University, Shenyang, China

Corresponding Author:
Gregory S. Karczmar, PhD
Department of Radiology, University of Chicago, 5841 S. Maryland Avenue, MC2026, Chicago, IL, USA 60637;
E-mail: gskarczm@uchicago.edu

Key Words: arterial input function, low dose DCE-MRI, cardiac output, indicator dilution principle

Abbreviations: Arterial input function (AIF), dynamic contrast-enhanced (DCE), magnetic resonance imaging (MRI), cardiac output (CO), cardiac MRI (CMRI), cardiac output from CMRI (CO_{CMRI}), cardiac output from DCE-MRI (CO_{DCE}), computed tomography (CT), repetition time (TR), echo time (TE), flip angle (FA), field of view (FOV), gadolinium (Gd), region of interest (ROI), standard deviation (SD)

ABSTRACT

Accurately measuring arterial input function (AIF) is essential for quantitative analysis of dynamic contrast-enhanced (DCE) magnetic resonance imaging (MRI). We used the indicator dilution principle to evaluate the accuracy of AIF measured directly from an artery following a low-dose contrast media ultrafast DCE-MRI. In total, 15 patients with biopsy-confirmed localized prostate cancers were recruited. Cardiac MRI (CMRI) and ultrafast DCE-MRI were acquired on a Philips 3 T Ingenia scanner. The AIF was measured at iliac arties following injection of a low-dose (0.015 mmol/kg) gadolinium (Gd) contrast media. The cardiac output (CO) from CMRI (CO_{CMRI}) was calculated from the difference in ventricular volume at diastole and systole measured on the short axis of heart. The CO from DCE-MRI (CO_{DCE}) was also calculated from the AIF and dose of the contrast media used. A correlation test and Bland–Altman plot were used to compare CO_{CMRI} and CO_{DCE}. The average (±standard deviation [SD]) area under the curve measured directly from local AIF was 0.219 ± 0.07 mM·min. The average (±SD) CO_{CMRI} and CO_{DCE} were 6.52 ± 1.47 L/min and 6.88 ± 1.64 L/min, respectively. There was a strong positive correlation ($r = 0.82$, $P < .01$) and good agreement between CO_{CMRI} and CO_{DCE}. The CO_{DCE} is consistent with the reference standard CO_{CMRI}. This indicates that the AIF can be measured accurately from an artery with ultrafast DCE-MRI following injection of a low-dose contrast media.

INTRODUCTION

Dynamic contrast-enhanced (DCE) magnetic resonance imaging (MRI) has been widely used for cancer diagnosis, as well as to quantitatively and noninvasively estimate a lesion's physiological characteristics (1-5). Quantitative DCE-MRI analysis is usually performed by using a pharmacokinetic model to obtain transfer rate constants, such as K^{trans} (forward volume transfer constant) and k_{ep} (reverse reflux rate constant between extracellular space and plasma) to characterize cancers (6, 7). However, variations of arterial input function (AIF) have a strong impact on calculations of physiological parameters (8-11). To extract reliable physiological parameters, an accurate AIF must be measured for each patient to account for variations in cardiac output (CO), systemic vascular function, and injection protocol (8). Unfortunately, there is potential for significant error in AIF measurements owing to partial volume effects, respiratory motions, inflow artifacts, dose-dependent T2*, and water exchange effects (12-14). To avoid problems with accurate measurement of patient-specific AIFs, a population AIF is often used in quantitative DCE-MRI data analysis (15-17). However, this does not account for the large interpatient and interscan variability, and this makes it difficult to compare physiological parameters between patients or measure changes in each patient over time (18, 19).

Several investigators have developed methods for quantitatively measuring patient-specific AIFs with MRI (10, 20, 21). However, the accuracy of the measured AIF was not verified in most studies. Previous studies reported that using CO combined with capillary input function improved the estimation of pharmacokinetic parameters for liver (22). By applying the indicator dilution principle (23) to constrain the area under the first pass of the AIF, Zhang et al. (24) reported a 3-fold higher precision in

ISSN 2379-1381 https://doi.org/10.18383/j.tom.2019.00004

calculating tumor perfusion parameters (K^{trans} and v_e). Di Giovanni et al. (25) reported a method for estimating perfusion parameters in patients with breast cancer using a T2*-weighted DCE data set optimized with CO. All of these studies applied the indicator dilution principle to optimize (scale) AIF based on each patient's CO. The need for this adjustment indicates that there were significant errors in the directly measured AIFs. Several studies also compared the AIFs measured from DCE-MRI and DCE computed tomography (CT) scans (26-28), where the AIF obtained from CT was treated as gold standard. However, the accuracy of this comparison was limited because of radiation dose constraints on temporal sampling with dynamic CT. In addition, this approach to validation entails radiation and additional contrast media.

In the present study, the indicator dilution principle was used to verify the accuracy of the AIF directly measured at the iliac arties following injection of a very low-dose contrast media. The key difference from previous studies is to verify, but not to optimize (scale), the measured AIF. The CO of each patient was directly calculated from short-axis cardiac MRI (CMRI) data. A high temporal resolution (ultrafast) prostate DCE-MRI scan was acquired with a low-dose contrast media, that is, 15% of the conventional amount, to avoid errors due to T2* changes and water exchange.

METHODOLOGY

Patient

This study was approved by the Institutional Review Board. Patients were enrolled from January 01, 2017, to March 01, 2018. Informed consent was obtained from all patients before conducting any study procedures. All patients enrolled in this study had prostate cancer proven by TRUS (transrectal ultrasound)-guided biopsy and were scheduled for radical prostatectomy at our hospital. Patients with previous treatments (radiation or chemotherapy) for prostate cancer, any type of bioimplant, moderate or high anxiety and/or claustrophobia, and contraindications for MRI or CT including impaired renal function (GFR $<$ 60 mL/min) were excluded from the study.

Fifteen patients (average age, 59 years; range, 47–73 years; average weight, 96.7 kg; range, 79–132 kg) received both cardiac MRI (CMRI) and a subsequent prostate DCE-MRI scans on the same day. The cohort comprised Gleason grade 6–9 lesions including: Gleason score (GS) 3 + 3 (n = 2), GS 3 + 4 (n = 11), GS 4 + 3 (n = 6), and GS 4 + 5 (n = 1).

CMRI and Prostate DCE-MRI Scan Protocols

Both CMRI and low-dose (0.015 mmol/kg of gadobenate dimeglumine) ultrafast DCE-MRI were acquired on the same Philips 3 T Ingenia scanner (Philips Healthcare, Best, Netherlands). A gradient echo sequence (B-TFE) was used for imaging the cardiac short axis (repetition time [TR] = 3.2 milliseconds, echo time [TE] = 1.6 milliseconds, flip angle [FA] = 45°, field of view [FOV] = 30 × 30 cm^2, slices = 14, phases = 30–40, gap = 0, in-plane resolution = 1.0 × 1.0 × 8 mm^3, maximum dynamic time = 800–1025 milliseconds).

Prostate MRI scans were performed approximately 30 minutes after the CMRI scan. First, clinically required prostate MRI scans, including high-resolution axial T2-weighted MRI and diffusion-weighted imaging, were acquired. Then variable FA 3D-FFE-T1 scans (TE/TR = 2.3/12 milliseconds; FA = 3°, 5°, 10°, 15°, 20°, 30°; FOV = 25 × 39 cm^2; in-plane resolution = 1.25 × 1.75 mm^2; thickness = 3.5 mm) were acquired for the calculation of native T1. Next, 150 axial ultrafast DCE-MRI using an mDixon sequence (27, 29, 30) (TE1/TE2/TR = 1.5/2.8/4.2 milliseconds, FA = 10°, FOV = 18 × 37 × 8 cm^3, in-plane resolution = 1.5 × 2.8 × 3.5 mm^3, temporal resolution = 1.5 s) were acquired over 225 seconds. A small dose (15% of the conventional dose, 0.015 mmol/kg) of Gd-based contrast media (gadobenate dimeglumine) was injected into the patients' left arm median cubital vein with a power injector at an injection duration of ~1.5 seconds, and followed by a 20-mL saline flush. The first 10 sets of ultrafast DCE-MRI images were precontrast scans used as baseline images. An approximate standard dose of contrast media was injected ~5 minutes after the low-dose contrast media DCE-MRI. Data from the standard dose were not used in the work reported here.

CO Measurements from CMRI

Electrodes were attached on the patient's chest during the CMRI scan to monitor the patient's electrocardiogram. The CO from CMRI (CO_{CMRI}) was calculated on the basis of the difference between ventricular volume at diastole and at systole measured on the short axis of the heart using the following formula (31-33):

$$CO_{CMRI} = HR \times (V_{ED} - V_{ES}) \quad (1)$$

where V_{ED} (L) is the volume at the end of diastole, V_{ES} (L) is the volume at the end of systole, and HR (beats/min, bpm) is the patient's heart rate recorded from electrocardiogram.

Contrast Media Concentration Measurements from DCE-MRI

For all DCE-MRI slices, the contrast media concentration as a function of time was calculated by using a previously published method (34) based on MRI TR, FA, native T1, and baseline signal. The native T1 was calculated by using the acquired precontrast dual-TR and variable flip angle images as previously described (35-37). The relaxivity of the contrast media of 5.5 L/mmol/s (38) was used to calculate the Gd concentration in millimolar units. AIFs were extracted from ultrafast DCE-MRI by manually tracing the region of interest (ROI) over the left and right iliac arteries. The shapes of the ROIs changed on different slices owing to blood vessel visibility variations on DCE-MRI. The average (±standard deviation [SD]) size of the ROI was 18 ± 6 pixels. The vessel walls could be easily excluded from the contour because they had different contrasts compared with the vessel lumen. The average contrast media concentration from the left and right iliac arteries was calculated and used as the AIF for the patient.

The accuracy of the measured AIF was verified by using the indicator dilution theory, which states that the area under a curve of the blood plasma contrast media concentration during the first-pass perfusion is constant in every vessel (25). The CO measured from CMRI versus DCE-MRI should be the same if the AIF is accurately measured.

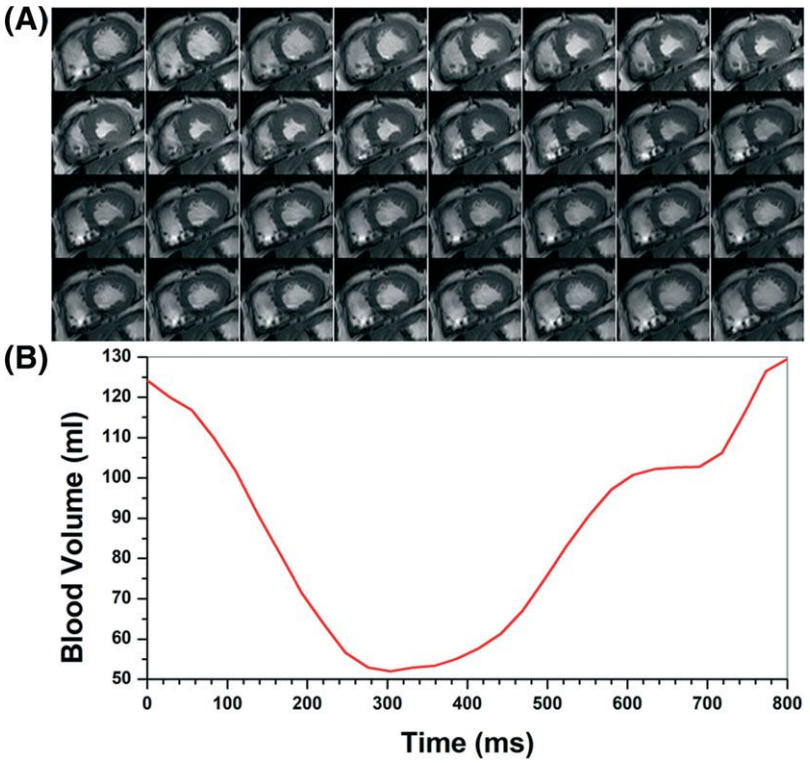

Figure 1. Cardiac output (CO) calculation from cardiac magnetic resonance imaging (CMRI) where (A) is a a section of short-axis CMRI during a full CO. Row 2, column 2, image shows the minimum cross-section area during the end of the systolic period; row 4, column 8, image shows the maximum cross-section area during the end of the diastolic period; (B) is the plot of ventricular volume measured from short-axis CMRI.

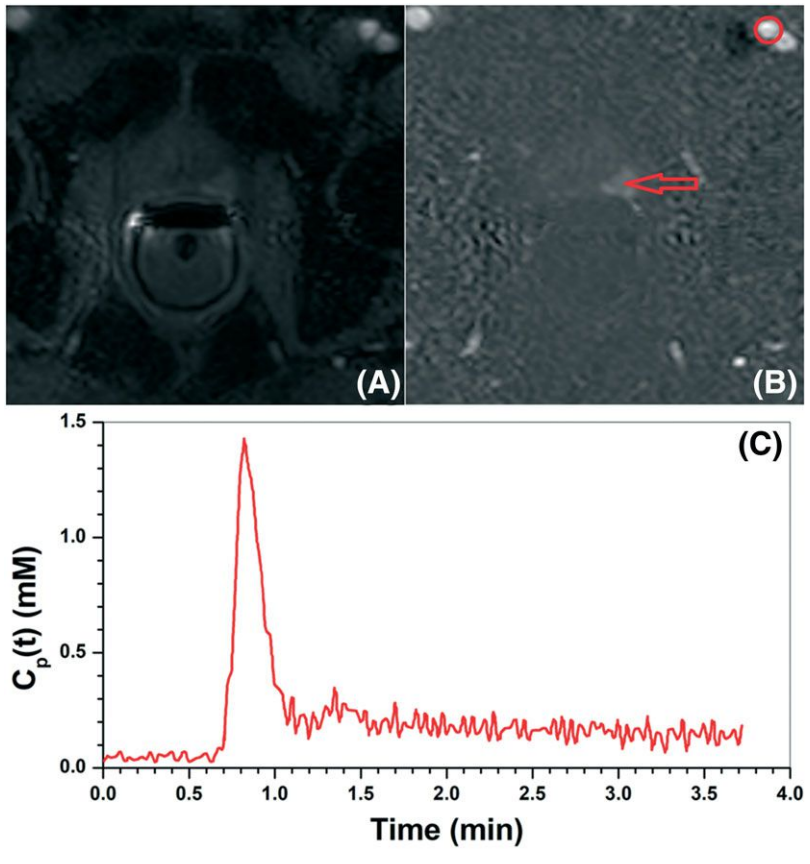

Figure 2. The ultrafast dynamic contrast-enhanced (DCE) image following a low dose of contrast media from the same patient (at the 40th dynamic scan) (A), the subtracted dynamic image from baseline shows early enhancement in prostatic carcinoma (red arrow) (B), and the AIF generated from iliac artery (red circle) from the ultrafast DCE-MRI data (C).

Table 1. Patients' Heart Rate, Area Under the Curve Measured Directly from Local AIF, and CO_{DCE} and CO_{CMRI}

No.	Heart Rate (beats/min)	AIF (AUC) (mM·min)	CO_{DCE} (L/min)	CO_{CMRI} (L/min)
1	66	0.228	5.92	5.90
2	68	0.252	5.63	5.90
3	73	0.203	6.37	5.70
4	53	0.189	6.88	7.70
5	47	0.440	2.73	3.99
6	82	0.175	7.20	6.54
7	60	0.174	7.47	5.80
8	63	0.170	8.24	7.74
9	67	0.225	6.67	6.01
10	60	0.229	6.81	5.50
11	65	0.163	8.56	7.90
12	61	0.149	8.66	7.92
13	65	0.266	5.64	5.10
14	58	0.169	9.67	9.96
15	51	0.247	6.80	6.10

CO Measurements from Ultrafast DCE-MRI

The CO from ultrafast DCE-MRI (CO_{DCE}) was calculated from the AIF and the dose of contrast media (24):

$$CO_{DCE} = Q \Big/ \int C_p(t)dt \qquad (2)$$

where Q (mmol) is the amount of the contrast media injected, and $C_P(t)$ (mM) is the contrast media concentration in the blood plasma. The area under the "first pass" of contrast media circulation was used for integration, that is, from baseline immediately before bolus arrival to the end of the first pass of the contrast media bolus.

Data Analysis

Paired Student *t*-test was used to compare the CO_{CMRI} and ultrafast CO_{DCE}. Pearson correlation test was performed to examine whether there is a linear relationship between CO_{CMRI} and CO_{DCE}. The agreements between CO_{CMRI} and CO_{DCE} values were evaluated using Bland–Altman analysis. $P < .05$ was considered significant.

RESULTS

CMRI was acquired first for calculating CO as a reference standard. Figure 1A shows typical images of the short axis of the heart during a cardiac cycle. The image in row 2, column 2, has the minimum cross-sectional area during the end of the systolic period; the image in row 4, column 8, has the maximum cross-sectional area during the end of the diastolic period. The corresponding plot of ventricular volumes measured from short axis of the heart as a function of time is shown in Figure 1B. The V_{ED} and V_{ES} used in equation (1) for calculating CO_{CMRI} were the maximum and minimum values, respectively, in the plot.

After CMRI, prostate DCE-MRI was acquired, and the AIF was measured directly from the iliac arteries. Figure 2A shows the ultrafast DCE image (at the 40th dynamic scan) from the same patient as shown in Figure 1. The subtracted dynamic image (Figure 2B) from the baseline (averaged from all baseline frames) shows early enhancement in prostatic carcinoma (red arrow), and the AIF traced from the iliac artery (red circle) is shown in Figure 2C. The first and second pass peaks of the contrast bolus can be clearly seen in the AIF despite limited signal-to-noise ratio owing to injection of the low-dose contrast media.

This data analysis procedure was applied to data from all 15 patients. Table 1 lists the patients' heart rate, the area under the curve measured directly from local AIF, and the calculated CO_{DCE} and CO_{CMRI} as the reference standard. The average (±SD) area under the curve measured directly from local AIF obtained from ultrafast DCE-MRI is 0.219 ± 0.07 mM·min. The average (±SD) COs calculated from CMRI and DCE-MRI are 6.52 ± 1.47 L/min and 6.88 ± 1.64 L/min, respectively. Both CO_{CMRI} and CO_{DCE} vary by over a factor of 2 in this group of patients. Figure 3A shows the scatter plot of the CO_{CMRI} vs CO_{DCE}. There are strong positive correlations ($r = 0.82$, $P < .01$) between the CO_{CMRI} and CO_{DCE}. The corresponding Bland–Altman plot shows good agreement between the two CO measurements (Figure 3B) with bias of 0.37 (L/min) and limits of agreement between −1.14 to 1.87 (L/min).

DISCUSSION

The indicator dilution principle was used to verify the accuracy of AIF measured at iliac arties from ultrafast DCE-MRI scan after injection of the low-dose contrast media. The subject's CO was directly measured from CMRI before the prostate DCE-MRI scan. We showed that the CO measured from ultrafast DCE-MRI is consistent with the "gold standard" CO measured from the short-axis CMRI. Our results show that AIF can be accurately measured directly from an artery with ultrafast DCE-MRI following injection of a low-dose contrast media. Accurate measurement of AIF for individual patients is critical for pharmacokinetic analysis.

The present results also suggest some clinical and diagnostic advantages for use of a low-dose contrast media DCE-MRI (39). The association between Gd-based contrast media administration and nephrogenic systemic fibrosis has been a concern for patients with renal failure. In a retrospective study, acute renal failure was reported after high-dose (≥0.2 mmol/kg) Gd injection for patients with an eGFR lower than 30 mL/min (40). It has also been reported that high-dose Gd injection contributed to an increased risk of nephrogenic systemic fibrosis (41). There are increasing concerns regarding intracellular accumulation of Gd-based contrast media (42). Therefore, a low-dose contrast media is preferred to minimize the risk (39). In addition, a standard dose of contrast media may lead to erroneous estimation of AIF owing to the high concentration of the contrast, water exchange effects, and T2* effects (12-14). The AIF measured from a low-dose contrast media may reduce such errors, as demonstrated by the present study results. In addition, this was previously shown by comparing results from ultrafast DCE-MRI with those from DCE-CT with 120-mL Iohexol in 20 patients with prostate cancer (27). Previous work from this group showed

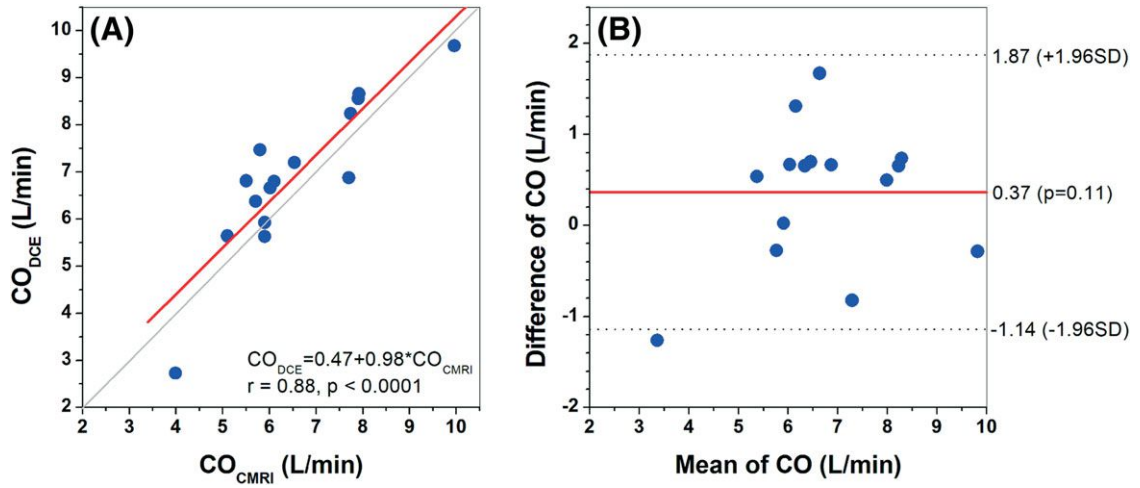

Figure 3. The scatter plot (A) shows the correlation (red line) of CO measured from the CMRI and ultrafast DCE-MRI. The corresponding Bland–Altman plot is shown in (B). The solid red line represents the mean difference ($CO_{DCE} - CO_{CMRI}$), and the dashed lines represent the lower and upper limits of agreement, defined by a range of $\pm 1.96 \times$ SD (95% confidence interval) around the mean. The *P*-value appearing beside the mean line on the plot indicates the probability of bias that differs from zero.

that low-dose Gd contrast distinguishes prostate cancer from benign prostate tissue more effectively than a standard dose on the basis of the signal enhancement rate; this diagnostic accuracy is similar on qualitative assessments (39).

CO is an important physiological parameter that directly relates to the metabolism of the entire organism (43). Results from the current group of patients show that there is a wide variation in CO (over a factor of 2) and this will result in large errors in pharmacokinetic parameters if it is not properly accounted for. A separate magnetic resonance sequence is often used to obtain CO. Our method with a low-dose contrast media and ultrafast DCE of the abdomen can provide accurate AIF *and* measure CO simultaneously, without performing additional scans, and with minimal exposure to contrast media.

Our measurements of CO and AIF are not perfect. For example, the native T1 measurement has a strong effect on Gd concentration calculation and AIF curve shape. This is because other parameters used in the calculation of contrast media concentration are dependent on MRI acquisition parameters. In addition, the native T1 must be determined from additional MRI scans that can contribute error. The CMRI slice thickness (8 mm) can be reduced to more accurately measure the diastolic and systolic volume for more accurate CO calculation. The measurement errors in V_{ED} and V_{ES} would only linearly affect CO_{CMRI} calculations, which were naturally smaller than errors in CO_{DCE} calculations owing to the many calculations involved.

In conclusion, accurately measuring of the AIF is essential for quantitative DCE-MRI. Here we compared the CO measured from CMRI as reference standard with the CO determined from measurement of the AIF with ultrafast DCE-MRI. The results validated the accuracy of the AIF measured at iliac arties following injection of a low-dose (0.015 mmol/kg) Gd contrast media. The low dose chosen for this study may not be optimal for measuring AIF and/or for the diagnosis of cancers. More studies are needed to determine the optimal low dose for both accurately measuring the AIF and estimating physiological parameters.

ACKNOWLEDGMENTS

This research is supported by the National Institutes of Health (Grant numbers: R01CA218700, U01CA142565, R01CA172801, and S10OD018448) and the University of Chicago Comprehensive Cancer Center from the National Cancer Institute Cancer Center Support Grant P30CA014599.

Disclosures: No disclosures to report.

Conflict of Interest: The authors have no conflict of interest to declare.

REFERENCES

1. Abramson RG1, Li X, Hoyt TL, Su PF, Arlinghaus LR, Wilson KJ, Abramson VG, Chakravarthy AB, Yankeelov TE. Early assessment of breast cancer response to neoadjuvant chemotherapy by semi-quantitative analysis of high-temporal resolution DCE-MRI: preliminary results. Magn Reson Imaging. 2013;31:1457–1464.
2. Alonzi R, Padhani AR, Allen C. Dynamic contrast enhanced MRI in prostate cancer. Eur J Radiol. 2007;63:335–350.
3. Gollub MJ, Gultekin DH, Akin O, Do RK, Fuqua JL 3rd, Gonen M, Kuk D, Weiser M, Saltz L, Schrag D, Goodman K, Paty P, Guillem J, Nash GM, Temple L, Shia J, Schwartz LH. Dynamic contrast enhanced-MRI for the detection of pathological complete response to neoadjuvant chemotherapy for locally advanced rectal cancer. Eur Radiol. 2012;22:821–831.
4. Pinker K, Bogner W, Baltzer P, Trattnig S, Gruber S, Abeyakoon O, Bernathova M, Zaric O, Dubsky P, Bago-Horvath Z, Weber M, Leithner D, Helbich TH. Clinical application of bilateral high temporal and spatial resolution dynamic contrast-enhanced magnetic resonance imaging of the breast at 7 T. Eur Radiol. 2014; 24:913–920.
5. Vos EK, Litjens GJ, Kobus T, Hambrock T, Hulsbergen-van de Kaa CA, Barentsz JO, Huisman HJ, Scheenen TW. Assessment of prostate cancer aggressiveness

using dynamic contrast-enhanced magnetic resonance imaging at 3 T. Eur Urol. 2013;64:448–455.
6. Patankar TF, Haroon HA, Mills SJ, Baleriaux D, Buckley DL, Parker GJ, Jackson A. Is volume transfer coefficient (K(trans)) related to histologic grade in human gliomas? AJNR Am J Neuroradiol. 2005;26:2455–2465.
7. Tofts PS, Brix G, Buckley DL, Evelhoch JL, Henderson E, Knopp MV, Larsson HB, Lee TY, Mayr NA, Parker GJ, Port RE, Taylor J, Weisskoff RM. Estimating kinetic parameters from dynamic contrast-enhanced T(1)-weighted MRI of a diffusable tracer: standardized quantities and symbols. J Magn Reson Imaging. 1999;10:223–232.
8. Fedorov A, Fluckiger J, Ayers GD, Li X, Gupta SN, Tempany C, Mulkern R, Yankeelov TE, Fennessy FM. A comparison of two methods for estimating DCE-MRI parameters via individual and cohort based AIFs in prostate cancer: a step towards practical implementation. Magn Reson Imaging. 2014;32:321–329.
9. Huang W, Chen Y, Fedorov A, Li X, Jajamovich GH, Malyarenko DI, Aryal MP, LaViolette PS, Oborski MJ, O'Sullivan F, Abramson RG, Jafari-Khouzani K, Afzal A, Tudorica A, Moloney B, Gupta SN, Besa C, Kalpathy-Cramer J, Mountz JM, Laymon CM, Muzi M, Schmainda K, Cao Y, Chenevert TL, Taouli B, Yankeelov TE, Fennessy F, Li X. The impact of arterial input function determination variations on prostate dynamic contrast-enhanced magnetic resonance imaging pharmacokinetic modeling: a multicenter data analysis challenge. Tomography. 2016;2:56–66.
10. Sanz-Requena R, Prats-Montalbán JM, Marti-Bonmati L, Alberich-Bayarri A, Garcia-Marti G, Perez R, Ferrer A. Automatic individual arterial input functions calculated from PCA outperform manual and population-averaged approaches for the pharmacokinetic modeling of DCE-MR images. J Magn Reson Imaging. 2015;42:477–487.
11. Wang S, Fan X, Medved M, Pineda FD, Yousuf A, Oto A, Karczmar GS. Arterial input functions (AIFs) measured directly from arteries with low and standard doses of contrast agent, and AIFs derived from reference tissues. Magn Reson Imaging. 2016;34:197–203.
12. Hansen AE, Pedersen H, Rostrup E, Larsson HB. Partial volume effect (PVE) on the arterial input function (AIF) in T1-weighted perfusion imaging and limitations of the multiplicative rescaling approach. Magn Reson Med. 2009;62:1055–1059.
13. Kleppesto M, Larsson C, Groote I, Salo R, Vardal J, Courivaud F, Bjørnerud A. T2*-correction in dynamic contrast-enhanced MRI from double-echo acquisitions. J Magn Reson Imaging. 2014;39:1314–1319.
14. Roberts C, Little R, Watson Y, Zhao S, Buckley DL, Parker GJ. The effect of blood inflow and B(1)-field inhomogeneity on measurement of the arterial input function in axial 3D spoiled gradient echo dynamic contrast-enhanced MRI. Magn Reson Med. 2011;65:108–119.
15. McGrath DM, Bradley DP, Tessier JL, Lacey T, Taylor CJ, Parker GJ. Comparison of model-based arterial input functions for dynamic contrast-enhanced MRI in tumor bearing rats. Magn Reson Med. 2009;61:1173–1184.
16. Meng R, Chang SD, Jones EC, Goldenberg SL, Kozlowski P. Comparison between population average and experimentally measured arterial input function in predicting biopsy results in prostate cancer. Acad Radiol. 2010;17:520–525.
17. Parker GJ, Roberts C, Macdonald A, Buonaccorsi GA, Cheung S, Buckley DL, Jackson A, Watson Y, Davies K, Jayson GC. Experimentally-derived functional form for a population-averaged high-temporal-resolution arterial input function for dynamic contrast-enhanced MRI. Magn Reson Med. 2006;56:993–1000.
18. Beuzit L, Eliat PA, Brun V, Ferre JC, Gandon Y, Bannier E, Saint-Jalmes H. Dynamic contrast-enhanced MRI: Study of inter-software accuracy and reproducibility using simulated and clinical data. J Magn Reson Imaging. 2016;43:1288–1300.
19. Huang W, Li X, Chen Y, Li X, Chang MC, Oborski MJ, Malyarenko DI, Muzi M, Jajamovich GH, Fedorov A, Tudorica A, Gupta SN, Laymon CM, Marro KI, Dyvorne HA, Miller JV, Barbodiak DP, Chenevert TL, Yankeelov TE, Mountz JM, Kinahan PE, Kikinis R, Taouli B, Fennessy F, Kalpathy-Cramer J. Variations of dynamic contrast-enhanced magnetic resonance imaging in evaluation of breast cancer therapy response: a multicenter data analysis challenge. Transl Oncol. 2014;7:153–166.
20. Cron GO, Foottit C, Yankeelov TE, Avruch LI, Schweitzer ME, Cameron I. Arterial input functions determined from MR signal magnitude and phase for quantitative dynamic contrast-enhanced MRI in the human pelvis. Magn Reson Med. 2011;66:498–504.
21. Fennessy FM, Fedorov A, Penzkofer T, Kim KW, Hirsch MS, Vangel MG, Masry P, Flood TA, Chang MC, Tempany CM, Mulkern RV, Gupta SN. Quantitative pharmacokinetic analysis of prostate cancer DCE-MRI at 3T: comparison of two arterial input functions on cancer detection with digitized whole mount histopathological validation. Magn Reson Imaging. 2015;33:886–894.
22. Chouhan MD, Bainbridge A, Atkinson D, Punwani S, Mookerjee RP, Lythgoe MF, Taylor SA. Improved hepatic arterial fraction estimation using cardiac output correction of arterial input functions for liver DCE MRI. Phys Med Biol. 2017;62:1533–1546.
23. Zierler K. Indicator dilution methods for measuring blood flow, volume, and other properties of biological systems: a brief history and memoir. Ann Biomed Eng. 2000;28:836–848.
24. Zhang JL, Rusinek H, Bokacheva L, Chen Q, Storey P, Lee VS. Use of cardiac output to improve measurement of input function in quantitative dynamic contrast-enhanced MRI. J Magn Reson Imaging. 2009;30:656–665.
25. Di Giovanni P, Ahearn TS, Semple SI, Azlan CA, Lloyd WK, Gilbert FJ, Redpath TW. Use of a capillary input function with cardiac output for the estimation of lesion pharmacokinetic parameters: preliminary results on a breast cancer patient. Phys Med Biol. 201121;56:1743–1753.
26. Rata M, Collins DJ, Darcy J, Messiou C, Tunariu N, Desouza N, Young H, Leach MO, Orton MR. Assessment of repeatability and treatment response in early phase clinical trials using DCE-MRI: comparison of parametric analysis using MR- and CT-derived arterial input functions. Eur Radiol. 2016;26:1991–1998.
27. Wang S, Lu Z, Fan X, Medved M, Jiang X, Sammet S, Yousuf A, Pineda F, Oto A, Karczmar GS. Comparison of arterial input functions measured from ultra-fast dynamic contrast enhanced MRI and dynamic contrast enhanced computed tomography in prostate cancer patients. Phys Med Biol. 2018;63:03NT1.
28. Yang C, Stadler WM, Karczmar GS, Milosevic M, Yeung I, Haider MA. Comparison of quantitative parameters in cervix cancer measured by dynamic contrast-enhanced MRI and CT. Magn Reson Med. 2010;63:1601–1609.
29. Dixon WT. Simple proton spectroscopic imaging. Radiology. 1984;153:189–194.
30. Le Y, Dale B, Akisik F, Koons K, Lin C. Improved T1, contrast concentration, and pharmacokinetic parameter quantification in the presence of fat with two-point Dixon for dynamic contrast-enhanced magnetic resonance imaging. Magn Reson Med. 2016;75:1677–1684.
31. Hundley WG, Li HF, Hillis LD, Meshack BM, Lange RA, Willard JE, Landau C, Peshock RM. Quantitation of cardiac output with velocity-encoded, phase-difference magnetic resonance imaging. Am J Cardiol. 1995;75:1250–1255.
32. Lin HY, Freed D, Lee TW, Arora RC, Ali A, Almoustadi W, Xiang B, Wang F, Large S, King SB, Tomanek B, Tian G. Quantitative assessment of cardiac output and left ventricular function by noninvasive phase-contrast and cine MRI: validation study with invasive pressure-volume loop analysis in a swine model. J Magn Reson Imaging. 2011;34:203–210.
33. Vincent JL. Understanding cardiac output. Crit Care. 2008;12:174.
34. Dale BM, Jesberger JA, Lewin JS, Hillenbrand CM, Duerk JL. Determining and optimizing the precision of quantitative measurements of perfusion from dynamic contrast enhanced MRI. J Magn Reson Imaging. 2003;18:575–584.
35. Fram EK, Herfkens RJ, Johnson GA, Glover GH, Karis JP, Shimakawa A, Perkins TG, Pelc NJ. Rapid calculation of T1 using variable flip angle gradient refocused imaging. Magn Reson Imaging. 1987;5:201–208.
36. Manuel A, Li W, Jellus V, Hughes T, Prasad PV. Variable flip angle-based fast three-dimensional T1 mapping for delayed gadolinium-enhanced MRI of cartilage of the knee: need for B1 correction. Magn Reson Med. 2011;65:1377–1383.
37. Pineda FD, Medved M, Fan X, Karczmar GS. B1 and T1 mapping of the breast with a reference tissue method. Magn Reson Med. 2016;75:1565–1573.
38. Rohrer M, Bauer H, Mintorovitch J, Requardt M, Weinmann H-J. Comparison of magnetic properties of MRI contrast media solutions at different magnetic field strengths. Invest Radiol. 2005;40:715–724.
39. He D, Chatterjee A, Fan X, Wang S, Eggener S, Yousuf A, Antic T, Oto A, Karczmar GS. Feasibility of dynamic contrast-enhanced magnetic resonance imaging using low-dose gadolinium: comparative performance with standard dose in prostate cancer diagnosis. Invest Radiol. 2018;53:609–615.
40. Prince MR, Zhang H, Morris M, MacGregor JL, Grossman ME, Silberzweig J, DeLapaz RL, Lee HJ, Magro CM, Valeri AM. Incidence of nephrogenic systemic fibrosis at two large medical centers. Radiology. 2008;248:807–816.
41. Broome DR, Girguis MS, Baron PW, Cottrell AC, Kjellin I, Kirk GA. Gadodiamide-associated nephrogenic systemic fibrosis: why radiologists should be concerned. AJR Am J Roentgenol. 2007;188:586–592.
42. Ramalho J, Semelka RC, Ramalho M, Nunes RH, AlObaidy M, Castillo M. Gadolinium-based contrast agent accumulation and toxicity: an update. AJNR Am J Neuroradiol. 2016;37:1192–1198.
43. Carlsson M, Andersson R, Bloch KM, Steding-Ehrenborg K, Mosen H, Stahlberg F, Stahlberg F, Ekmehag B, Arheden H. Cardiac output and cardiac index measured with cardiovascular magnetic resonance in healthy subjects, elite athletes and patients with congestive heart failure. J Cardiovasc Magn Reson. 2012;14:51.

TOMOGRAPHY® RESEARCH ARTICLE

GantryMate: A Modular MR-Compatible Assistance System for MR-Guided Needle Interventions

Andreas Reichert[1], Michael Bock[1], Michael Vogele[2], and Axel Joachim Krafft[1]

[1]Department of Radiology, Medical Physics, Medical Center – University of Freiburg, Faculty of Medicine, University of Freiburg, Freiburg, Germany and [2]Interventional Systems GmbH, Kitzbühel, Austria

Corresponding Author:
Andreas Reichert, MSc
Department of Radiology, Medical Physics, Medical Center – University of Freiburg, Killianstr. 5a, 79106 Freiburg;
E-mail: andreas.reichert@uniklinik-freiburg.de

Key Words: interventional magnetic resonance imaging, MR-guided interventional procedures, percutaneous procedures, MRI-compatible assistance system

Abbreviations: Magnetic resonance imaging (MRI), magnetic resonance (MR), phase-only cross-correlation (POCC), gradient-echo (GRE), spin-echo (SE), repetition time (TR), echo time (TE), flip angle (FA), field of view (FOV), bandwidth (BW)

ABSTRACT

Percutaneous minimally invasive interventions are difficult to perform in closed-bore high-field magnetic resonance systems owing to the limited space between magnet and patient. To enable magnetic resonance–guided needle interventions, we combine a small, patient-mounted assistance system with a real-time instrument tracking sequence based on a phase-only cross-correlation algorithm for marker detection. The assistance system uses 2 movable plates to align an external passive marker with the anatomical target structure. The targeting accuracy is measured in phantom experiments, yielding a precision of 1.7 ± 1.0 mm for target depths up to 38 ± 13 mm. In in vivo experiments, the possibility to track and target static and moving structures is demonstrated.

INTRODUCTION

Magnetic resonance imaging (MRI) has unique advantages to guide and monitor interventional procedures over other imaging methods such as computed tomography or ultrasound (US). It offers an unparalleled soft tissue contrast, it can acquire images in arbitrary scan planes along the device trajectories, it provides morphological and functional imaging, and it exposes neither the patient nor the interventionalist to ionizing radiation. MRI can be used at various stages of the intervention—during target localization, device positioning, monitoring of therapeutic progress, and assessment of therapeutic outcome (1-3). Besides intravascular (4) and thermal treatments [e.g., with high-intensity focused ultrasound (5-7)], minimally invasive percutaneous interventions such as needle biopsies tremendously benefit from image guidance (8, 9).

Percutaneous interventional procedures have traditionally been performed in open-bore low-field magnetic resonance (MR) systems to ensure good patient access (10). However, a good contrast-to-noise ratio is required to differentiate the target region from the surrounding tissue, a high signal-to-noise ratio is needed to unambiguously visualize the instruments in the patient's body, and an adequate spatial resolution needs to be ensured to detect, e.g., small deviations from the planned needle pathway. Currently, these requirements are best fulfilled in high-field, high gradient power MRI systems at 1.5 T or 3 T, which are typically constructed as solenoid superconducting MR magnets. However, spatial constraints because of the closed-bore design (typical bore diameter of ≤70 cm, cover-to-cover length in the range of 125–160 cm) limit the physicians' access to the patient and make device handling challenging. Assistance systems can help overcome these problems and facilitate percutaneous interventions (1-3, 11). Such systems have been shown to improve needle placement (12, 13), help to achieve needle trajectories with increased precision, and help to shorten procedure durations (14-17). Any assistance system operating in the MRI environment must not only conform to all conventional safety standards for MRI accessories but also preserve the MR image quality, and its operation has to remain unaffected by the MR system's radiofrequency and magnetic fields. This makes the construction of assistance systems for the MR environment a challenging task.

In recent years, assistance systems have been presented for numerous applications with various degrees of remote control and haptic feedback. The fully MR-compatible pneumatic arm INNOMOTION (18) can hold and align an instrument around a pivot point in 6 degrees of freedom (DOF) over the patient inside the magnet bore. It found only a limited number of applications (19, 20) and is no longer commercially available. Another commercial prototype assistance system is the smaller, second-generation remote-controlled manipulator using pneumatic air stepper motors (21) for MR-guided transrectal prostate biopsies (22). A technically more complex system is the neuroArm (23) driven by ultrasonic piezoelectric motors, which features remotely controlled and exchangeable neurosurgical instruments and provides the neurosurgeon with both visual control and

ISSN 2379-1381 https://doi.org/10.18383/j.tom.2019.00007

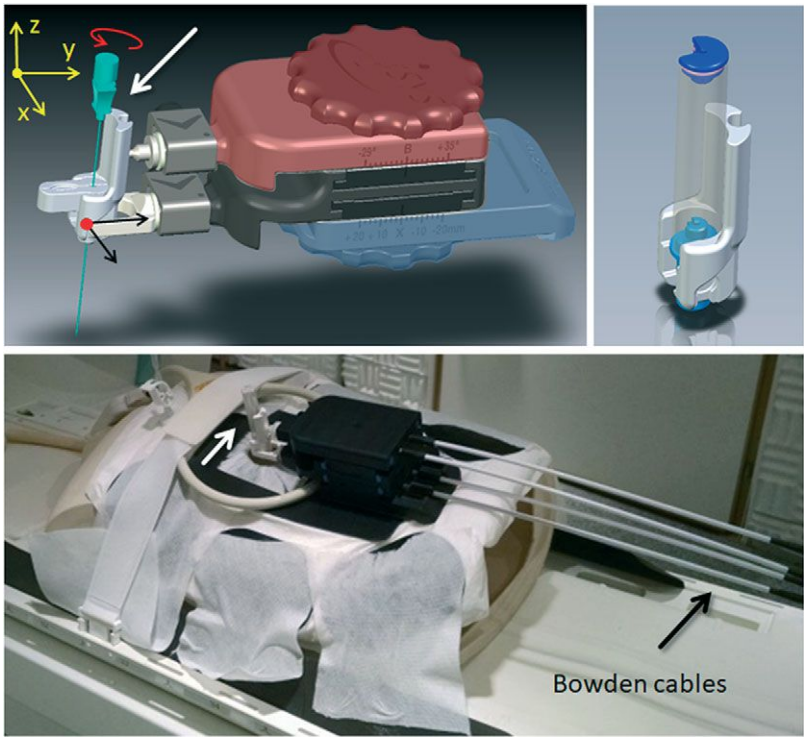

Figure 1. Schematic of the GantryMate assistance system (top, left). The base platform (blue) allows gross positioning of the device, and the upper 2 plates (black and red) can be moved independently in *x* and *y* directions. This allows steering of a distal instrument holder (white arrow) through Bowden cable (visible in the bottom image) from outside the magnet bore. The lower plate (black) translates the instrument holder in *x* or *y* direction, and the upper plate allows for rotations of the holder (red arrow) around a pivot point (red dot). The holder can be equipped with a customized cylindrical marker (top, right) or a needle sleeve (top, left).

haptic feedback. In addition to these commercial systems, several other small patient-mounted systems have been recently presented (13, 24): Monfaredi et al. described a shoulder-mounted robot using 4 MRI-compatible piezo-motors for needle placement with 4 DOF (25). Ghelfi et al. assessed a patient-mounted light puncture robot for percutaneous needle interventions that is fixed to the patient's body to allow for patient movements (26). The 4 piezoelectric driven motors, which are placed at the feet to avoid interferences with MR imaging, enable placement of a needle in 4 DOF through Bowden cables.

Nearly all of these systems depend on sophisticated control mechanisms that require bulky additional hardware in the MR room, making it difficult for them to integrate into the clinical routine (24, 27). Thus, despite the variety and abundance of system designs, only a few of these design concepts were converted into commercially available systems for clinical use (13). Therefore, the exploration and design of novel assistance systems for MR-guided interventions remain areas of active research.

Here, we present an alternative patient-mounted assistance system for image-guided percutaneous needle interventions. Compared with existing systems, this new GantryMate system features a flexible, simpler design and is constructed entirely from plastic material. It can be remotely steered via Bowden cables to manipulate a needle-guide inside the magnet bore, i.e., no additional hardware is required for operation. We tested the assistance system according to American Society for Testing and Materials (ASTM) standards (28-32), and we verified if the MR system's radiofrequency and magnetic fields remain unaffected. To enable automatic scan plane positioning, we combined GantryMate with a tracking MRI sequence to automatically detect a passive marker needle-guide and followed the device motion during targeting in real time (22, 33-35). In a phantom setting, the lateral puncture accuracy of needle placements, as well as the procedure time, was assessed. Furthermore, technical proof of concept in in vivo situations is shown with the successful alignment of the needle pathway with basivertebral veins in the vertebrae and a vessel branch in the liver of a volunteer.

METHODS

Assistance System GantryMate

The assistance system GantryMate (Interventional Systems, Kitzbühel, Austria) is entirely constructed from electrically non-conducting, nonmetallic, and nonmagnetic plastic and fiber glass materials (Figure 1). The system is mounted on a base platform, which is used for gross positioning and can be fixed to the patient with straps. The system consists of 2 movable plates (Figure 1, top left) and an instrument holder, which is attached to the distal end-effector (Figure 1, top right). The plates can each be moved independently in 2 translational DOF (forward-backward—FB, left-right—LR) via 4 mechanical adjustment threads, which are accessible from outside the magnet through Bowden cables (cf. Figure 1, bottom). Manipulation of the lower plate moves the entire unit in either FB or LR direction relative to the base platform (approximate translational range = 40 mm in each direction). Translation (FB and LR direction) of the upper plate relative to the lower plate causes rotations of the distal instrument holder (angular range = ±30° in both directions) about a pivot point located at the level of the lower plate (cf. Figure 1, top left).

During targeting, a passive marker is attached to the instrument holder for online device localization and planning of the needle pathway. Once the marker is correctly aligned with the target in the patient's body, a needle is manually inserted through the marker that now serves as a needle guide, and the

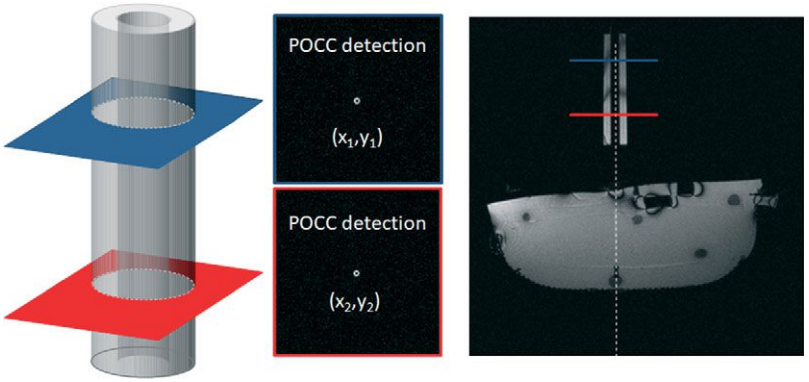

Figure 2. Schematics of the passive marker tracking sequence. Two parallel images (blue and red) are acquired perpendicular to the symmetry axis of the marker (left). The position of the ring-shaped structures can be detected via a POCC algorithm (middle). The position information is used to align a third image along the marker and to visualize the theoretical needle trajectory (right). The sequence runs continuously and allows online needle targeting procedures.

insertion can be visualized with real-time imaging. Alternatively, a needle sleeve can be attached that allows for the use of needles with varying diameters.

Device Tracking

For device tracking during the targeting, the GantryMate system was equipped with a cylindrical passive marker needle-guide (inner/outer diameter = 5/13 mm, length = 62.5 mm) filled with a contrast agent solution (Magnevist®/H_2O: 1/100, Bayer Schering Pharma AG, Berlin, Germany). To automatically determine the position and orientation of the passive marker, a previously developed tracking sequence was used (22, 33-35). The sequence acquires 2 T1-weighted gradient echo (FLASH) images, which are oriented perpendicular to the marker's symmetry axis. In these images, the marker is seen as a ring-like structure (Figure 2) that can be automatically detected via a phase-only cross-correlation (POCC) algorithm (33) during online image reconstruction. Based on the position information, the sequence automatically aligns the plane of a subsequent imaging acquisition with the marker direction. For imaging, a different contrast (balanced steady-state free precession, bSSFP) is used to increase the lesion contrast. The bSSFP image is then displayed online on a screen in the MR room, and the theoretical needle trajectory is overlaid to enable targeting maneuvers of the needle-guide.

MR Safety and Compatibility Measurements

MR experiments were carried out in a 1.5 T whole-body system (MAGNETOM Symphony, Siemens Healthcare, Erlangen, Germany) with a manufacturer-provided open-loop coil (Flex Loop Large, Siemens Healthcare) for signal reception. A bottle (diameter = 12 cm; Siemens Healthcare) filled with a solution [(1.25 g $NiSO_4$ × 6 g H_2O + 5 g NaCl)/1000 g H_2O] was placed on the system's patient table around the magnet's isocenter. Measurements were conducted without and with the assistance system placed on top of the phantom bottle to examine image artifacts and distortions according to the standard ASTM F2119 (30). Therefore, gradient-echo (GRE) and spin-echo (SE) images were acquired in sagittal and axial orientations with the following parameters: GRE: repetition time (TR)/echo time (TE) = 500/15 ms, slice thickness = 3 mm, slices = 20, slice gap = 6 mm, flip angle (FA) = 30°, field of view (FOV) = 350 × 350 mm, matrix = 256 × 256, bandwidth (BW) = 130 Hz/px; SE: TR/TE = 500/20 ms, slice thickness = 5 mm, slices = 20, slice gap = 10 mm, FA = 90°, FOV = 350 × 350 mm, matrix = 256 × 256, BW = 130 Hz/px. Afterwards, a dual-echo GRE sequence was used to assess B_0 distortions without and with the device in place: TR/TE/ΔTE = 15/8.76/4.76 ms, slice thickness = 5 mm, FA = 15°, FOV = 300 × 300 mm, matrix = 256 × 256, BW = 250 Hz/px (Figure 3, left). In addition, 3D GRE images were acquired (TR/TE = 1500/2.6 ms, slice thickness = 1.88 mm, FA = 30/60°, FOV = 127 × 240 mm, matrix = 128 × 68, BW = 279 Hz/px) to assess B_1 distortions and to calculate a relative FA map (Figure 3, right) with the double-angle method (36, 37).

Phantom Measurements

The accuracy of the needle positioning was measured in a phantom experiment with an agar phantom (volume = 50 × 50 × 40 mm^3) with 13 embedded fiducial targets (mean diameter = 8.1 mm), which was placed inside a plastic casing that was shaped like a human torso (Figure 1, bottom). After target definition in a 3D GRE localizer data set, the following procedure, including 4 steps, was performed for each target:

1. The passive marker was attached to the instrument holder at the manipulator's center position.
2. Instrument positioning and alignment of the needle pathway with the target were performed under online guidance with the POCC tracking sequence (Figure 4; FLASH tracking images: TR/TE = 4.0/2.0 ms, FOV = 244 × 300 mm^2, matrix = 156 × 192, α_{FLASH} = 15°, slice thickness = 10 mm, BW = 1180 Hz/px; bSSFP targeting image: TR/TE = 4.0/2.0 ms, FOV = 244 × 300 mm^2, matrix = 156 × 192, α_{bSSFP} = 70°, slice thickness = 5 mm, BW = 1180 Hz/px, TA_{tot} per tracking cycle = 1.9 s).

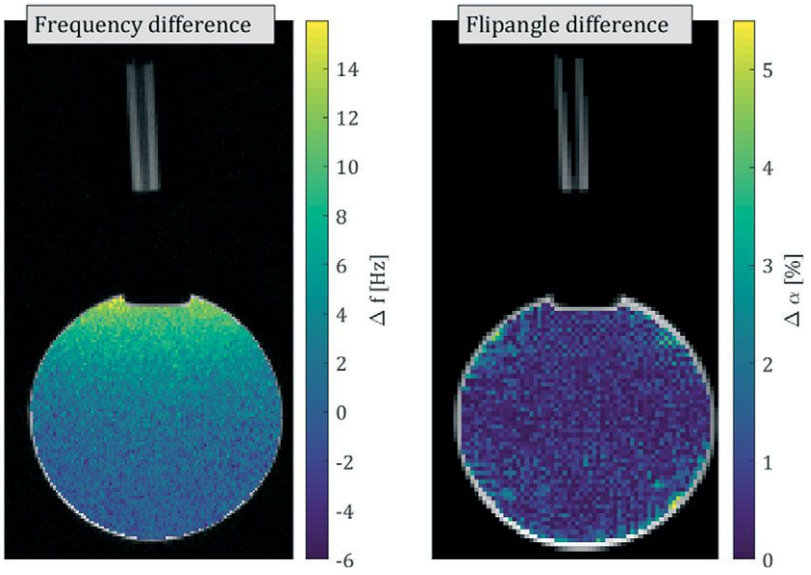

Figure 3. Frequency difference (left) and relative flip angle (FA) difference (right) in the phantom between images acquired before and after the assistance system was placed on the phantom.

3. The passive marker was replaced with a dedicated needle sleeve for a 16-G needle (Somatex GmbH, Teltow, Germany).
4. The needle was manually advanced into the target under online monitoring with a HASTE (*H*alf-Fourier *A*cquisition *S*ingle-shot *T*urbo spin *E*cho imaging) sequence (TR/TE = 2000/46 ms, FOV = 250 × 250 mm^2, matrix = 256 × 256, α_{HASTE} = 180°, thickness = 5 mm, partial Fourier = 4/8, BW = 781 Hz/px).

After all targets were successfully punctured, a high-resolution (0.5 × 0.5 × 0.5 mm^3) 3D bSSFP data set (TR/TE = 7.52/3.76 ms, FOV = 200 × 150 mm^2, matrix = 384 × 288, α_{bSSFP} = 70°, thickness = 0.5 mm, BW = 482 Hz/px) was acquired to evaluate the needle pathways and assess the insertion accuracy. Therefore, the distance of each needle pathway was measured in the gel from the target center using reformatted multiplanar views (Figure 5).

In Vivo Measurements

To simulate an in vivo application, a volunteer was placed on the patient table in supine position, and the assistance system was attached above the abdomen (Figure 6, top left). The assistance system was positioned in its center position, and then a targeting maneuver was simulated using the circular cross sec-

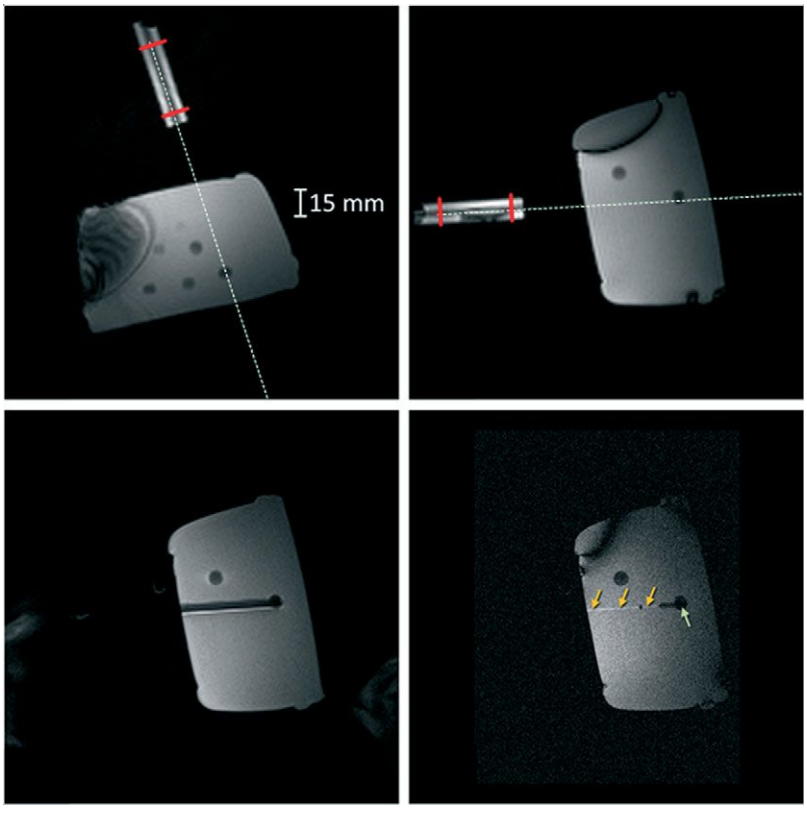

Figure 4. Example of the alignment of the theoretical needle trajectory (dashed white) with the desired target in transversal and sagittal orientation (top left and right). The location of the tracking slices is marked in red. A HASTE sequence is used for online monitoring of the needle insertion (bottom, left). After the needle is removed, the needle pathway (yellow arrows) is visible, which can be used to determine targeting precision (bottom, right).

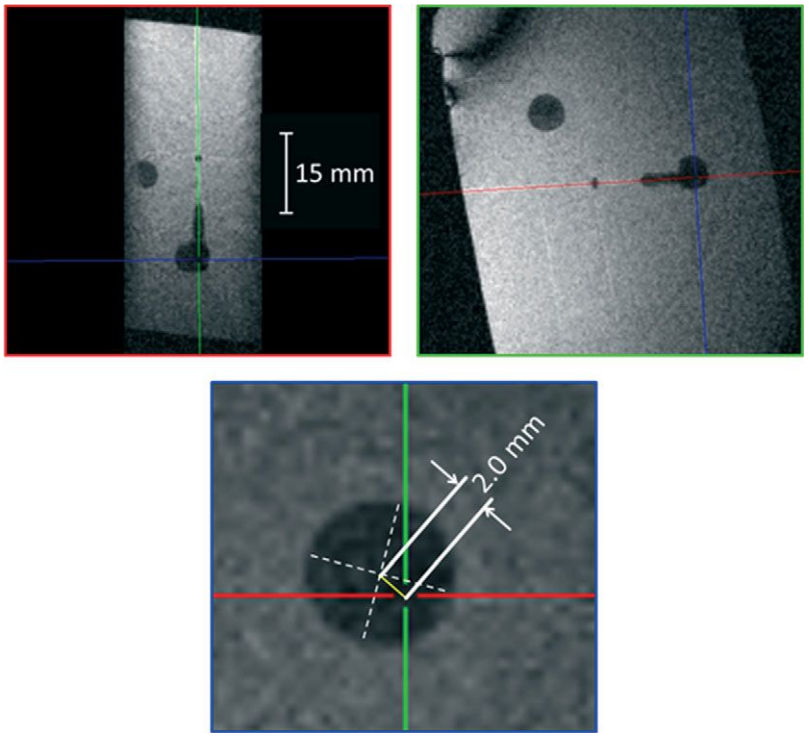

Figure 5. Reformatted orthogonal multiplanar views of the needle pathway (red and green boxes) that define the bullseye-view (blue box) for assessment of the lateral accuracy.

tions of the basivertebral veins in the lumbar vertebra (L2, L3, L4 and L5) as anatomical target structures (Figure 6, top right). The location and orientation of the GantryMate device were manipulated via the Bowden cables under online tracking guidance (FLASH tracking images: TR/TE = 3.6/1.7 ms, FOV: 380 × 380 mm^2, matrix = 154 × 192, α_{FLASH} = 15°, slice thickness = 10 mm, BW = 1042 Hz/px, partial Fourier = 6/8; bSSFP targeting image: TR/TE = 3.6/1.7 ms, FOV: 380 × 380 mm^2, matrix = 154 × 192, α_{bSSFP} = 70°, slice thickness = 5 mm, BW = 1042 Hz/px, partial Fourier = 6/8, TA_{tot} per tracking cycle = 1.3 s) until the needle pathway was aligned with the target in sagittal and transversal views.

To test the assistance system in a moving target, a distal vessel branch of the portal vein was defined as target which is moving over the breathing cycle (Figure 7). Again, the device was manipulated under online tracking guidance until the needle pathway was aligned with the target. Gross alignment was performed during breathing in a transverse view, and final

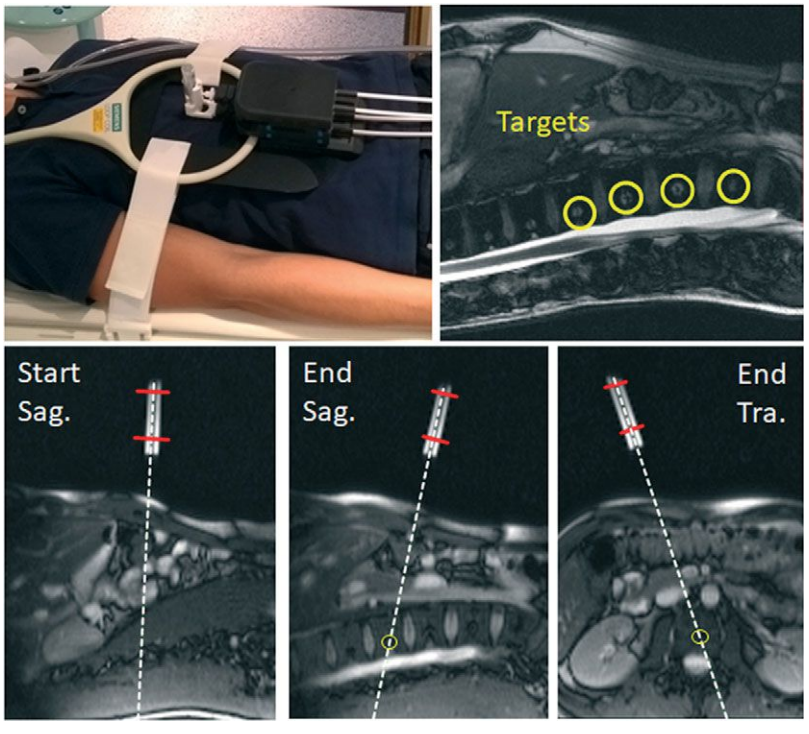

Figure 6. Experimental setup (top left) for the targeting of stationary targets (cross sections of basivertebral veins, top right) in a volunteer. The targeting procedure is started in a sagittal view (bottom left), and the projected needle pathway (dashed white) is aligned with the predefined target region in sagittal and transversal views (yellow circles, bottom middle and right).

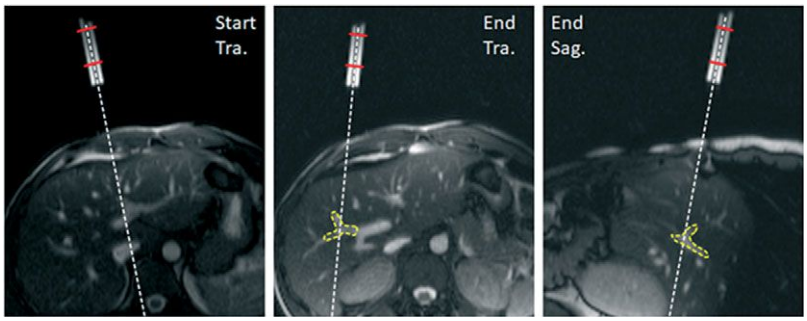

Figure 7. First image of the procedure to align the projected needle pathway (dashed white) with the predefined target region (left). Last images of the procedure in transversal and sagittal view (middle, right); the needle pathway was successfully aligned with the target region.

alignment of the needle pathway was done in a breath-hold maneuver for a sagittal and transverse view.

RESULTS

No distortion or signal loss artifacts were visible in either the GRE or SE images (images not shown). B_0 field and FA mapping without and with the assistance systems revealed no significant influence of the device on either the B_0 or B_1 field, respectively (Figure 3). Here, B_0 maps without and with the setup showed a mean frequency difference of 0.9 Hz, that is, 0.01 ppm (range: −6 and 15.5 Hz). The B_1 field measurements showed almost no effects because of the setup with mean relative B_1 differences of 0.2%.

The results from the needle experiment in the phantom with 13 fiducial targets are summarized in Table 1. Puncturing was successfully performed in all 13 targets within the mean procedure time (duration for instrument positioning, exchange of marker and needle sleeve, and needle insertion) of $t_{puncture}$ = 6.4 ± 1.5 min. The mean lateral distance between the needle channels and the geometric center points of the targets was 1.7 ± 1.0 mm.

In the in vivo experiment, the passive marker needle guide could be successfully aligned with cross sections of the basivertebral veins in the lumbar spine. The durations of the individual targeting procedures are summarized in Table 2 (mean duration for instrument positioning = 2.0 ± 0.5 min). Furthermore, the passive marker needle guide could be also successfully aligned with a moving target in the liver. Here, gross alignment was performed during free breathing (duration = 2.7 min) and final fine alignment could be accomplished during short breath holds for sagittal (duration = 15 s) and transverse (duration = 5 s) image orientation, respectively.

DISCUSSION AND CONCLUSION

In this work, a patient-mounted assistance system for MR-guided needle interventions is presented in combination with an online POCC device tracking sequence. The assistance system is designed to move a passive needle-guide inside of a closed-bore MR system and can be mechanically manipulated from outside the magnet via Bowden cables.

Table 1. Summary of Measured Diameter, Depth from Phantom Surface, Needle Pathway Angles in FB and LR Direction, Duration (Procedure Time for Instrument Positioning and Needle Insertion), and Lateral Distance of Needle Pathway to Target Center for all 13 Targets

Target #	Diameter (mm)	Depth (mm)	Angle FB (°)	Angle LR (°)	Duration (min:second)	Lateral Distance (mm)
1	8.0	53.8	12	16	6:45	1.1
2	8.3	52.9	0	3	4:26	2.0
3	8.1	53.5	16	3	8:46	2.6
4	7.9	53.1	7	3	5:41	3.6
5	7.7	55.9	12	3	7:24	2.6
6	7.5	35.5	17	4	5:59	0.1
7	7.4	33.4	23	1	7:02	1.4
8	8.7	38.4	5	0	6:54	2.3
9	9.0	23.7	28	9	5:27	1.6
10	8.5	23.5	32	19	8:07	0.3
11	8.7	24.2	29	9	8:40	0.7
12	7.8	25.6	16	11	5:01	1.5
13	8.1	20.1	0	0	3:31	2.2
Mean ± SD[a] (range)	8.1 ± 0.5 (7.4–9.0)[a]	38 ± 13 (20.1–55.9)	15 (0–32)	6 (0–19)	6:26 ± 1:33 (3:31–8:46)	1.7 ± 1.0 (0.1–3.6)

[a] Respective mean values and standard deviations (SD) are summarized in the bottom line.

Table 2. Summary of Measured Times of Needle Pathway Alignment with the Vertebral Veins

Lumbar Vertebra	Diameter (mm)	Duration (min:second)
L2	7.7	02:18
L3	9.4	03:03
L4	8.7	01:34
L5	8.2	02:04
L2	7.7	01:55
L3	9.4	01:56
L4	8.7	01:50
L5	8.2	01:36
Mean ± SD[a] (range)	8.6 ± 0.6 (7.7–9.4)	2:00 ± 0:30 (1:34–3:03)

[a] Respective mean values and standard deviations (SD) are summarized in the bottom line.

The assistance system is manufactured from electrically nonconducting, nonmetallic, and nonmagnetic plastic material. Measurements revealed no interference with the magnetic or the radiofrequency fields of the MR system, as can be seen in the small B_0 frequency differences and small relative B_1 distortions (Figure 3). Thus, according to our measurements, the device can be classified as "MR-safe" according to the ASTM F2503 standard (28). This safety assessment is only valid for the holder without the instrument (e.g., a needle), which needs to be tested separately. However, many MR-safe needles are commercially available, which can be used in combination with the assistance system.

In combination with a passive POCC tracking sequence, the assistance system provided an accurate and versatile tool for MR-guided needle interventions. In the phantom measurement, all 13 targets were successfully punctured. The system was intuitive to use, no special training was required, and the surrounding adjacent targets were not unintentionally perforated. The mean procedure duration (6.5 min) and the lateral accuracy (1.7 mm) in this evaluation are comparable to values found in previous studies (22, 33-35).

In the in vivo experiment, the device could target stationary targets such as deep-lying cross sections of the basivertebral veins in the lumbar vertebrae. Here, the needle trajectory could be successfully aligned with the targets in 2.0 ± 0.5 min, which would allow one to perform multiple procedures in a single setting. Furthermore, the device was tested in a moving target—here, a hepatic vessel branch was chosen as a fiducial target because the anatomical structure can be unambiguously identified on MR images—and also follows the movement of the liver during respiratory motion. Again, the targeting procedure could be performed without any special training. Gross targeting could be achieved during breathing motion and fine adjustment with only 2 breath holds in 20 seconds, which is in line with requirements for abdominal procedures.

The current realization of the system allows planning of the lateral needle pathway, whereas the depth of the needle insertion has to be manually defined. For this, the target depth is either predefined in the targeting images before needle insertion. Alternatively, the needle insertion can be monitored continuously using image sequences which are less prone to needle-induced artifacts. Here, real-time monitoring of the insertion has been realized with the spin-echo single-shot technique HASTE, which is insensitive to field inhomogeneities and provides an excellent T2 contrast but is leading to signal saturation and increased specific absorption rate (SAR) values. In this context, accelerated SE-based sequences such as targeted-HASTE (38) were presented for an optimized visualization of the needle insertion. However, in some needle placement scenarios, depth control is not needed. For example, in arthrography contrast agent insertions, the needle is inserted until the tip touches the bone (25).

Currently, targeting the passive marker is not possible as soon as the needle is introduced in the marker because the needle artifacts distort the ring-shaped cross section required for POCC tracking. However, it would be beneficial to place the needle inside of the marker from the very beginning of the procedure because the total procedure time could be reduced as the needle would only have to be mounted once and no exchange of passive marker and needle guide would be required. To enable targeting with the needle inside the marker, again fast spin echo sequences could be used which reduce the needle artifact. Accurate tracking of the marker with the needle in place could be highly advantageous to detect needle deflections from the planned needle trajectory during insertion. Here, the interventionalist could use the direct visual feedback to stabilize the needle trajectory by manual needle rotation (39).

In its current implementation, the device setup with Bowden cables is simpler than that of other assistance systems. Nevertheless, it could be expanded in future for example, with more advanced robotic technologies for fully remote control. With its flexible design, it is not restricted to single interventional scenarios and could be used in many abdominal applications, for example, transgluteal prostate or kidney biopsies. The main components of the device are reusable and only small parts (distal instrument holder, marker, instruments) are made as sterile disposables, which might be important for clinical applicability.

The presented combination of the MR-safe assistance system and online POCC tracking sequence could also be used for other MR-guided interventions. For example, RF ablation electrodes could be placed in the target regions, and the thermal destruction would be subsequently monitored with MR temperature imaging. All these procedures would benefit from acceleration of the POCC tracking sequence. This can be achieved, for example, with simultaneous acquisition of the tracking images (35) or with radially undersampled projection imaging of the passive marker (40). A higher temporal resolution would allow better tracing of anatomical targets during breathing motion.

In conclusion, we presented a simple, accurate, and versatile assistance system in combination with a passive marker tracking sequence, which might be a valuable tool to facilitate MR-guided interventions.

ACKNOWLEDGMENTS

We would like to thank Dr. Florian Maier (Siemens Healthcare, Erlangen, Germany) for support with the implementation of the tracking sequence. Financial support from the Tiroler Innovationsförderung (Project "GantryMate") is gratefully acknowledged. This study was supported by Deutsche Forschungsgemeinschaft (DFG) grant number HA 7006/1-1.

Disclosures: M. Bock reports grants from Tiroler Innovationsförderung (Project "GantryMate") during the conduct of the study; nonfinancial support (research cooperation) from Siemens Healthcare, outside the submitted work. Dr. Vogele reports grants from Tiroler Innovationsförderung, other from Interventional Systems GmbH, during the conduct of the study. In addition, Dr. Vogele has patent 20 2013 007 831 issued to iSYS Medizintechnik GmbH, patent 20 2013 007 831.6 pending to iSYS Medizintechnik GmbH, and patent 20 2011 005 573.6 pending to iSYS Medizintechnik GmbH.

REFERENCES

1. Fritz J, Weiss CR. The state-of-the-art of interventional magnetic resonance imaging: Part 1. Top Magn Reson Imaging. 2018;27(1):1–2.
2. Weiss CR, Fritz J. The state-of-the-art of interventional magnetic resonance imaging: Part 2. Top Magn Reson Imaging. 2018;27:113–114.
3. Kaye EA, Granlund KL, Morris EA, Maybody M, Solomon SB. Closed-bore interventional MRI: percutaneous biopsies and ablations. AJR Am J Roentgenol. 2015; 205:W400–W410.
4. Bock M, Wacker FK. MR-guided intravascular interventions: techniques and applications. J Magn Reson Imaging. 2008;27:326–338.
5. Jolesz FA. MRI-guided focused ultrasound surgery. Annu Rev Med. 2009;60: 417–430.
6. Napoli A, Anzidei M, Ciolina F, Marotta E, Marincola BC, Brachetti G, Mare LD, Cartocci G, Boni F, Noce V, Bertaccini L, Catalano C. MR-guided high-intensity focused ultrasound: current status of an emerging technology. Cardiovasc Intervent Radiol. 2013;36:1190–1203.
7. Yiallouras C, Ioannides K, Dadakova T, Pavlina M, Bock M, Damianou C. Three-axis MR-conditional robot for high-intensity focused ultrasound for treating prostate diseases transrectally. J Ther Ultrasound. 2015;3:2.
8. Beyersdorff D, Winkel A, Hamm B, Lenk S, Loening SA, Taupitz M. MR imaging-guided prostate biopsy with a closed MR unit at 1.5 T: initial results. Radiology. 2005;234:576–581.
9. Overduin CG, Fütterer JJ, Barentsz JO. MRI-guided biopsy for prostate cancer detection: a systematic review of current clinical results. Curr Urol Rep. 2013;14: 209–213.
10. Lewin JS, Petersilge CA, Hatem SF, Duerk JL, Lenz G, Clampitt ME, Williams ML, Kaczynski KR, Lanzieri CF, Wise AL, Haaga JR. Interactive MR imaging-guided biopsy and aspiration with a modified clinical C-arm system. Am J Roentgenol. 1998;170:1593–1601.
11. Weiss CR, Nour SG, Lewin JS. MR-guided biopsy: a review of current techniques and applications. J Magn Reson Imaging. 2008;27:311–325.
12. Heerink WJ, Ruiter SJS, Pennings JP, Lansdorp B, Vliegenthart R, Oudkerk M, de Jong KP. Robotic versus freehand needle positioning in CT-guided ablation of liver tumors: a randomized controlled trial. Radiology. 2019;290:826–832.
13. Arnolli MM, Hanumara NC, Franken M, Brouwer DM, Broeders IA. An overview of systems for CT- and MRI-guided percutaneous needle placement in the thorax and abdomen. Int J Med Robot. 2015;11:458–475.
14. Krieger A, Susil RC, Menard C, Coleman JA, Fichtinger G, Atalar E, Whitcomb LL. Design of a novel MRI compatible manipulator for image guided prostate interventions. IEEE Trans Biomed Eng. 2005;52:306–313.
15. Stoianovici D, Kim C, Srimathveeravalli G, Sebrecht P, Petrisor D, Coleman J, Solomon SB, Hricak H. MRI-safe robot for endorectal prostate biopsy. IEEE ASME Trans Mechatron. 2014;19:1289–1299.
16. Susil RC, Camphausen K, Choyke P, McVeigh ER, Gustafson GS, Ning H, Miller RW, Atalar E, Coleman CN, Ménard C. System for prostate brachytherapy and biopsy in a standard 1.5 T MRI scanner. Magn Reson Med. 2004;52:683–687.
17. Schouten MG, Ansems J, Renema WKJ, Bosboom D, Scheenen TWJ, Fütterer JJ. The accuracy and safety aspects of a novel robotic needle guide manipulator to perform transrectal prostate biopsies. Med Phys. 2010;37:4744–4750.
18. Melzer A, Gutmann B, Remmele T, Wolf R, Lukoscheck A, Bock M, Bardenheuer H, Fischer H. INNOMOTION for Percutaneous Image-Guided Interventions. IEEE Eng Med Biol Mag. 2008;27:66–73.
19. Li M, Kapoory A, Mazilu D, Woody B, Horvath KA. Cardiac interventions under MRI guidance using robotic assistance. In: 2010 IEEE International Conference on Robotics and Automation. 2010. pp. 2574–2579.
20. Miller JG, Li M, Mazilu D, Hunt T, Horvath KA. Robot-assisted real-time magnetic resonance image–guided transcatheter aortic valve replacement. J Thorac Cardiovasc Surg. 2016;151:1407–1412.
21. Bomers JGR, Bosboom DGH, Tigelaar GH, Sabisch J, Fütterer JJ, Yakar D. Feasibility of a 2nd generation MR-compatible manipulator for transrectal prostate biopsy guidance. Eur Radiol. 2017;27:1776–1782.
22. Zamecnik P, Schouten MG, Krafft AJ, Maier F, Schlemmer H-P, Barentsz JO, Bock M, Fütterer JJ. Automated real-time needle-guide tracking for fast 3-T MR-guided transrectal prostate biopsy: a feasibility study. Radiology. 2014;273:879–886.
23. Sutherland GR, Latour I, Greer AD. Integrating an image-guided robot with intraoperative MRI: a review of the design and construction of neuroArm. IEEE Eng Med Biol Mag. 2008;27:59–65.
24. Monfaredi R, Cleary K, Sharma K. MRI robots for needle-based interventions: systems and technology. Ann Biomed Eng. 2018;46:1479–1497.
25. Monfaredi R, Iordachita I, Wilson E, Sze R, Sharma K, Krieger A, Fricke S, Cleary K. Development of a shoulder-mounted robot for MRI-guided needle placement: phantom study. Int J Comput Assist Radiol Surg. 2018;13:1829–1841.
26. Ghelfi J, Moreau-Gaudry A, Hungr N, Fouard C, Véron B, Medici M, Chipon E, Cinquin P, Bricault I. Evaluation of the needle positioning accuracy of a light puncture robot under MRI guidance: results of a clinical trial on healthy volunteers. Cardiovasc Intervent Radiol. 2018;41:1428–1435.
27. Busse H, Kahn T, Moche M. Techniques for interventional MRI guidance in closed-bore systems. Top Magn Reson Imaging. 2018;27(1):9–18.
28. ASTM F2503-13, Standard Practice for Marking Medical Devices and Other Items for Safety in the Magnetic Resonance Environment, ASTM International, West Conshohocken, PA, 2013, www.astm.org [Internet]. ASTM International; Available from: http://www.astm.org/cgi-bin/resolver.cgi?F2503-13; Accessed: April 16, 2019.
29. ASTM F2052-15, Standard Test Method for Measurement of Magnetically Induced Displacement Force on Medical Devices in the Magnetic Resonance Environment, ASTM International, West Conshohocken, PA, 2015, www.astm.org [Internet]. ASTM International; Available from: http://www.astm.org/cgi-bin/resolver.cgi?F2052-15; Accessed: April 16, 2019.
30. ASTM F2119-07(2013), Standard Test Method for Evaluation of MR Image Artifacts from Passive Implants, ASTM International, West Conshohocken, PA, 2013, www.astm.org [Internet]. ASTM International; Available from: http://www.astm.org/cgi-bin/resolver.cgi?F2119-07R13; Accessed: April 16, 2019.
31. ASTM F2182-11a, Standard Test Method for Measurement of Radio Frequency Induced Heating On or Near Passive Implants During Magnetic Resonance Imaging, ASTM International, West Conshohocken, PA, 2011, www.astm.org [Internet]. ASTM International; Available from: http://www.astm.org/cgi-bin/resolver.cgi?F2182-11A; Accessed: April 16, 2019.
32. ASTM F2213-17, Standard Test Method for Measurement of Magnetically Induced Torque on Medical Devices in the Magnetic Resonance Environment, ASTM International, West Conshohocken, PA, 2017, www.astm.org [Internet]. ASTM International; Available from: http://www.astm.org/cgi-bin/resolver.cgi?F2213-17; Accessed: April 16, 2019.
33. de Oliveira A, Rauschenberg J, Beyersdorff D, Semmler W, Bock M. Automatic passive tracking of an endorectal prostate biopsy device using phase-only cross-correlation. Magn Reson Med. 2008;59:1043–1050.
34. Krafft AJ, Zamecnik P, Maier F, de Oliveira A, Hallscheidt P, Schlemmer H-P, Bock M. Passive marker tracking via phase-only cross correlation (POCC) for MR-guided needle interventions: Initial in vivo experience. Phys Med. 2013;29:607–614.
35. Reichert A, Bock M, Reiss S, Overduin CG, Fütterer JJ, Krafft AJ. Simultaneous slice excitation for accelerated passive marker tracking via phase-only cross correlation (POCC) in MR-guided needle interventions. Magn Reson Mater Phys Biol Med. 2018;31:781–788.
36. Stollberger R, Wach P. Imaging of the active B1 field in vivo. Magn Reson Med. 1996;35:246–251.
37. Cunningham CH, Pauly JM, Nayak KS. Saturated double-angle method for rapid B1+ mapping. Magn Reson Med. 2006;55:1326–1333.
38. Zimmermann H, Müller S, Gutmann B, Bardenheuer H, Melzer A, Umathum R, Nitz W, Semmler W, Bock M. Targeted-HASTE imaging with automated device tracking for MR-guided needle interventions in closed-bore MR systems. Magn Reson Med. 2006;56:481–488.
39. Abolhassani N, Patel R, Moallem M. Needle insertion into soft tissue: a survey. Med Eng Phys. 2007;29:413–431.
40. Reichert A, Krafft AJ, Bock M. Passive marker tracking with phase-only cross correlation (POCC) in highly undersampled radial images: improvements by point-spread-function considerations. In: Proceedings of the International Society of Magnetic Resonance in Medicine (ISMRM); 2018; Paris, France.

TOMOGRAPHY® RESEARCH ARTICLE

A Carbon-Fiber Sheet Resistor for MR-, CT-, SPECT-, and PET-Compatible Temperature Maintenance in Small Animals

Veerle Kersemans, Stuart Gilchrist, Sheena Wallington, Philip D. Allen, Ana L. Gomes, Gemma M. Dias, Bart Cornelissen, Paul Kinchesh, and Sean C. Smart

Department of Oncology, CRUK/MRC Oxford Institute for Radiation Oncology, University of Oxford, Oxford, UK

Corresponding Author:
Veerle Kersemans, PhD
CRUK/MRC Oxford Institute for Radiation Oncology, Old Road Campus Research Building, Off Roosevelt Drive, OX3 7DQ, Oxford, UK;
E-mail: Veerle.Kersemans@oncology.ox.ac.uk

Key Words: carbon fiber, heater, multimodal imaging, MR-CT-PET-SPECT compatibility
Abbreviations: Magnetic resonance (MR), computed tomography (CT), single-photon emission computed tomography (SPECT), positron emission tomography (PET), radiofrequency (RF), fast low angle shot (FLASH), echo time (TE), field of view (FOV), repetition time (TR), flip angle (FA), dynamic contrast-enhanced (DCE), signal-to-noise ratio (SNR)

ABSTRACT

A magnetic resonance (MR)-, computed tomography (CT)-, single-photon emission computed tomography (SPECT)-, and positron emission tomography(PET)-compatible carbon-fiber sheet resistor for temperature maintenance in small animals where space limitations prevent the use of circulating fluids was developed. A 250 Ω carbon-fiber sheet resistor was mounted to the underside of an imaging cradle. Alternating current, operating at 99 kHz, and with a power of 1-2 W, was applied to the resistor providing a cradle base temperature of ~37°C. Temperature control was implemented with a proportional–integral–derivative controller, and temperature maintenance was demonstrated in 4 mice positioned in both MR and PET/SPECT/CT scanners. MR and CT compatibility were also shown, and multimodal MR-CT-PET-SPECT imaging of the mouse abdomen was performed in vivo. Core temperature was maintained at 35.5°C ± 0.2°C. No line-shape, frequency, or image distortions attributable to the current flow through the heater were observed on MR. Upon CT imaging, no heater-related artifacts were observed when carbon-fiber was used. Multimodal imaging was performed and images could be easily coregistered, displayed, analyzed, and presented. Carbon fiber sheet resistors powered with high-frequency alternating current allow homeothermic maintenance that is compatible with multimodal imaging. The heater is small, and it is easy to produce and integrate into multimodal imaging cradles.

INTRODUCTION

In vivo imaging using positron emission tomography (PET), single-photon emission computed tomography (SPECT), and x-ray computed tomography (CT) is increasingly applied in conjunction with magnetic resonance imaging (MRI). In some cases, these systems are colocated within a common gantry system such that the animal is moved between modalities under scanner control. In contrast, where this is not possible, it is advantageous to hold the animal in a cradle that can be moved with the animal in situ such that the animal position within the cradle is constant and image registration is straightforward (1-3). Regardless of the scanner-specific cradle arrangements, it is essential that animals are actively provided with heat to avoid hypothermia that is a consequence of anesthesia (4, 5). It is also essential that the method used for providing thermoregulation is compatible with all of the imaging systems being used, and that it can operate within the physical and technical constraints of each system. MRI scanners, in particular, frequently operate with limited space owing to the loading requirements of radiofrequency (RF) coils (6) and this hinders the use of the most widely used heating systems that include heat lamps, circulating warmed fluids and air, prewarmed heat reservoirs, and exothermic chemical reaction pads (4, 5, 7-10). MRI scanners must avoid the use of large volumes of metal and even small amounts of ferromagnetic materials, while CT scanners, and by inference PET and SPECT scanners where CT-derived intensity corrections are made, must avoid materials of high atomic number in order to avoid image corruptions derived from severe x-ray attenuation (11). MRI must also avoid the formation of magnetic field inhomogeneities consequent to the delivery of electric current.

Compact magnetic resonance (MR)-compatible heaters for homeothermic maintenance in small animals have recently been described (7, 12). In one design, a resistive electrical heater was formed from a tightly-wound twisted pair wire, interfaced to a homeothermic maintenance controller. This heater can be implemented very easily on existing electrical heater systems, and it provided adequate heating performance without causing any significant distortion of the magnetic field or the images. Unfortunately, it is not robustly deformable, and any usage-related change in shape, resulting from normal wear and tear, can lead

ISSN 2379-1381 https://doi.org/10.18383/j.tom.2019.00008

to imperfect spatial cancellation of stray magnetic field. An alternative heater element was formed from a narrow-gauge wire connected to a high-frequency (99 kHz) alternating current (AC) power source. This frequency was chosen because its cycle time, 10.1 μs, was short enough that long-term field inhomogeneities, and consequent MR image distortions, were absent, while any sound resulting from the heater's use in a magnetic field was inaudible, even for small rodents (12). In contrast to the twisted pair wire, the use of temporal, rather than spatial, averaging of stray magnetic fields toward zero allowed the use of arbitrarily shaped resistors that could be deformable.

While both of these heater elements are compatible with MR, the presence of copper (atomic number, z = 29) leads to excessive x-ray attenuation and streak artifacts in CT images. This obscures anatomy and pathology, and it corrupts the CT-based attenuation maps used for quantification of PET and SPECT images. As such, these types of electrical heaters cannot be used with CT unless they can be formed from an electrically conductive, low-atomic-number element, such as lithium, beryllium, or carbon, as these do not cause attenuation-related image corruptions. Lithium is highly reactive in air; beryllium is very expensive and toxic; while carbon, in the form of resin-embedded carbon-fiber is chemically inert to air, cheap, non-toxic, and easy to work, and is widely used as a heating element in a range of applications. Here, we present a high-frequency AC-based heating resistor in which the metal wire has been replaced by a custom-shaped carbon-fiber sheet to effect a planar heater element that is both MR- and CT-compatible and which can, as a result, be used with CT-corrected PET and SPECT imaging. Improved stability of temperature control was achieved using a proportional–integral–derivative (PID) device that reduced the output power as the temperature approached its target. This is crucial to minimize temperature fluctuations, especially as the MRI system itself delivers an unspecified and variable amount of heat to the animal during operation.

In this report, we describe the use of a carbon-fiber heater, show its multimodal imaging compatibility, and show the generation of a multimodal image of the mouse abdomen formed using dynamic contrast-enhanced MRI (DCE-MRI), CT, ^{99m}Tc SPECT, and ^{18}F (PET)SPECT; (PET)SPECT describes the SPECT detection of 511-keV photons as used in conventional PET imaging and allows true simultaneous imaging of PET and SPECT isotopes.

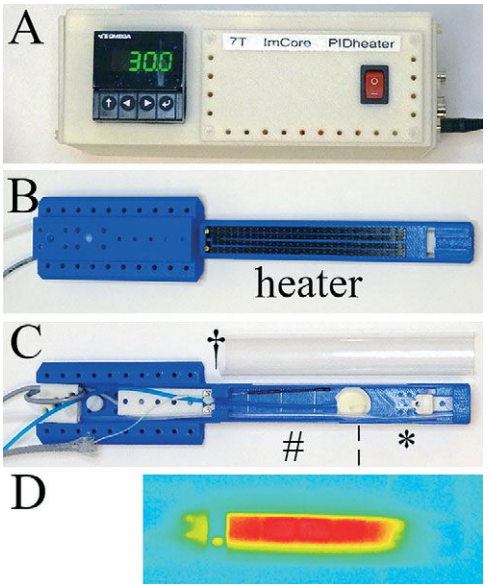

Figure 1. Carbon fiber sheet–resistive heater embedded in a 3D-printed, flat-base multimodal imaging cradle. Proportional–integral–derivative (PID) controller (A); bottom view of the cradle (B); top view of the cradle (C); and thermal image of the cradle surface (D). The cradle contains a heater and (*) a mouthpiece assembly consisting of a base block, a vertical and horizontal adjustable mouth bar, and an anesthetic gas delivery tube, (¦) is a pressure balloon for respiration monitoring, (#) is an optical fiber for temperature monitoring, and (†) is a cover sheet to contain anesthetic gas. The current wires and metal couplings to the carbon-fiber are located beyond the imaging field of view (FOV) so do not present image distortions.

MATERIALS AND METHODS

Ethics Statement

All animal studies were performed in full compliance with national legislation and with the approval of the Oxford University Animal Welfare and Ethical Review Body.

Imaging Cradle and Carbon Fiber Sheet-Resistive Heater Assembly

A flat-based MR- and CT-compatible animal support cradle was designed using computer-aided design (CAD) software (SolidWorks, Dassault Systèmes, Hammersmith, UK) and printed using acrylonitrile butadiene styrene (ABS) plastic, on a 3D printer (HP Designjet 3D, Bracknell, UK). A 250-Ω resistive heater element formed from a 0.75-mm-thick carbon-fiber sheet (764-8700, RS Components, Corby, UK) which was cut into 4- × 3-mm-wide legs, each 120-mm in length and 1 mm apart, and glued to the underside of the cradles as shown in Figure 1B. As such, the heater element was positioned 1.68 mm below the lowest part of the object to be imaged.

The heater volume was ~1.5 mL, occupying 3.05% of the volume of the small-diameter RF coil used for the validation studies reported in this work. The cradle was assembled with an anesthetic gas supply tube, a heater power cable, a fiber optic rectal temperature probe, and a pneumatic respiration monitor (Figure 1C). All services were supplied using "quick-fit" connectors so that the cradle could be disconnected from one imaging system and reconnected on the other quickly and without any risk of the animals recovering from the anesthetic depth used before disconnection.

AC Heating Control Units

Core body temperature was measured using an optical rectal temperature probe (OTP-M-X-62F2.5-1.5(PTFE/PVC)-XN-7GT-M1-PV0014a, Opsens Solutions, Québec, Canada) connected via

a 10-m fiber-optic extension to an AccuSens 4-channel Signal Conditioner (ACS-P4-N-62SC Opsens Solutions, Québec, Canada).

Temperature control was driven using a PID controller (CN16PT-305-DC, OMEGA Engineering Ltd., Manchester, UK; Figure 1A). This controller takes the analog output of the AccuSens unit as the temperature input signal, providing gain control signal to an AC power circuit, which comprises a Pierce oscillator operating at 99-kHz output and a power amplifier (LM1875, Texas Instruments, Dallas, Texas). The maximum output power was limited to ~2 W for the heating elements described, although this could be increased or decreased for other heating elements. The maximum temperature of the cradle surface was 37.0°C, when a maximum output gain was used indefinitely, and this was demonstrated using a thermal imaging camera (Testo 875-1i, RS Components, Corby, UK). This temperature was selected to ensure thermal burns could not result from the use of this heating apparatus. All animal service signal and power leads entering and leaving the magnet room were passed through RF filters (series 700 high-performance filtered connector, 4000 pF capacitance Pi filter type, part number SCI 56-715-005, API Technology Corp., Milton Keynes, UK). These animal services all operate at low frequencies (<101 kHz) and can pass through the filters, while higher frequencies, some of which could affect MR image quality, cannot.

Animal Preparation

Female 6- to 8-wk-old CBA/Crl mice (Charles-River, Harlow, UK) were housed in individual ventilated cages at constant temperature and humidity, and water and food were freely available. Anesthesia was induced and maintained using isoflurane (1%–4%) in air/oxygen (v/v 80/20); the animals recovered afterwards with no ill effect. Induction and recovery were performed in a heated unit with a base temperature of ~37°C. Rectal temperature was set at 36.0°C using the aforementioned heater driver. The depth of anesthesia was monitored using a pressure balloon system measuring the animal's respiration rate, which was maintained at 60–90 breaths/minute. Respiratory signals were processed for use in a gating control of the scanner to allow for respiratory synchronized MRI.

Assessment of Homeothermic Maintenance in Mice

For validation of thermal stability, mice (n = 4 for MRI; n = 4 for SPECT/(PET)SPECT/CT) were anaesthetized and placed on the imaging cradle in the MRI or SPECT/(PET)SPECT/CT scanner. Rectal temperature was monitored for 50 minutes in total after which the animals recovered.

For MRI, the additional heat load of high-duty cycle MRI scanning was included after the animals had reached their equilibrium temperature.

Assessment of MRI Compatibility

MR compatibility of the heater element was tested in a water gel phantom (Hydrogel, 70-01-5022, ClearH2O) by using single-shot Point-RESolved Spectroscopy (PRESS) spectroscopy and 2D fast low angle shot (FLASH) imaging, and in vivo in the mouse using respiratory-gated 2D FLASH and cardiorespiratory-gated 3D FLASH imaging. In all cases, the same acquisition was repeated for the heater turned on and off.

MRI was performed on a 7 T, 210-mm VNMRS horizontal bore preclinical imaging system equipped with a 120-mm bore gradient insert (Varian Inc., Palo Alto, California). RF transmission and reception were performed using a 26-mm-diameter, 100-mm-long RF coil for system validation purposes, and a 32-mm-diameter, 45-mm-long RF coil for multimodal imaging (Rapid Biomedical GmbH, Rimpar, Germany).

Single-shot PRESS spectra from a $2 \times 2 \times 2$ mm^3 voxel positioned at the bottom edge of the water gel phantom, closest to the heater (≈1.68 mm from the heater), were acquired with echo time (TE) = 15 milliseconds, bandwidth = 4 kHz, and complex points = 2048. Raw data were zero-filled to give a real spectrum of 8192 points with 2-Hz exponential line broadening. The full width at half maximum (FWHM) linewidth of this voxel was ~20 Hz. Spectra were acquired with the heater turned off and on. In addition, a difference spectrum for the heater turned on and off was compared with a spectrum acquired with the heater off. Ten repetitions of a multi-slice spoiled gradient echo scan were acquired on this gel phantom: repetition time (TR) = 100 milliseconds, TE = 10 milliseconds, thickness (THK) = 1 mm, field of view (FOV) = 100×25 mm^2, matrix = 384×96, flip angle (FA) = 30°. Dummy scanning was performed for 50 seconds before data acquisition to stabilize a steady state. The total scan time was 146 seconds for 10 repetitions, with each repetition alternating between the heater turned off and on.

In vivo, a multi-slice, constant TR, spoiled gradient echo with respiration-gating and reacquisition (13) was performed: TR = 1000 milliseconds, TE = 6 milliseconds, THK = 1 mm, FOV = 100×25 mm^2, matrix = 512×128, FA = 30°. The total scan time was 195 seconds. ImageJ was used to calculate the difference image between the heater turned off and on (14). Ten repetitions of a cardiorespiratory-gated 3D FLASH scan with reacquisition (15) were acquired, with each repetition alternating between the heater turned off and on, and 10 further repeats were acquired with the heater just turned on: TR = 3 milliseconds, TE = 1.28 milliseconds, FOV = $108 \times 27 \times 27$ mm^3, matrix = $512 \times 128 \times 128$, gradient spoiling with 167 mT/m for 0.85 milliseconds in all three axes, RF hard pulse duration = 16 μs, FA = 5°, and RF spoiling. The total scan time was <5 minutes for the 20 repetitions. Dummy scanning was performed for at least 20 seconds before data acquisition to stabilize a steady state. Image intensity as a function of the repetition number was determined in ImageJ, using a square ROI positioned proximal to the heater.

For multimodal imaging, respiratory-gated 3D FLASH imaging was performed repeatedly to effect DCE-MRI.

Signal-to-noise ratio (SNR) was tested using measurements of the pulse power required to generate a FA excitation pulse of 90°, and by acquisition of a nongated 3D FLASH scan (as per the DCE scan described above), using a postmortem animal (so as not to be affected by the cardiorespiratory motion) and in the presence and absence of the carbon-fiber heating element.

Assessment of CT Compatibility

CT compatibility was tested in vivo in the absence of any heater and in the presence of either a copper wire or a carbon-fiber sheet heater element. Whole-body CT was performed using the VECTor^{4}CT system (MILabs, Utrecht, The Netherlands). Images

were acquired at 50 kV and 0.24 mA using continuous rotation (40°/s) and were reconstructed using a cone-beam filtered back-projection (Feldkamp algorithm) on a 0.2-mm voxel grid. Beam hardening and ring artifacts were corrected, and the voxel numbers were converted into Hounsfield units by using a premeasured calibration factor.

Demonstration of Multimodal (PET)SPECT/SPECT/CT/MR Imaging

Multimodal MR-CT-(PET)SPECT-SPECT imaging of the abdomen, including the kidneys, was performed on animals that were held in the same cradle as for MRI and using anesthesia and physiological maintenance as described above.

(PET)SPECT and SPECT imaging was performed using the single-gantry VECTor^{4}CT system fitted with the HE-UHR-RM PET/SPECT collimator (1.8-mm pinholes); (PET)SPECT describes the SPECT detection of 511-keV photons as used in conventional PET imaging. CT, SPECT, and (PET)SPECT imaging were performed immediately before MRI; ^{111}In-citrate and ^{18}F-fluorodeoxyglucose (FDG) were used for SPECT and (PET)SPECT imaging, respectively. DCE was performed (scan details in Assessment of MRI Compatibility) with a scan time of ~10–15 s/frame. Contrast agent (100 μL, Gadospin, Viscover, Germany) was infused in the lateral tail vein over 17 seconds at the start of frame 11/50.

Data were acquired in list mode (0–1200 keV) using MILabs acquisition software v7.39. Triple energy window–based scatter correction was applied for each photon peak window (^{18}F: 460-562 keV with background windows set to 439.6–460 keV and 562–582.4 keV; ^{111}In: 155.7–190.3 keV and 222.3–271.7 keV with background windows set to 148.8-155.7 keV, 190.3–197.2 keV, 212.4–222.3 keV, and 271.7–281.6 keV). All images were reconstructed with MILabs reconstruction software v3.24 on 0.8-mm isotropic 3D voxel grids using dual matrix similarity regulated ordered-subset expectation maximization (dual matrix SROSEM) (8). After reconstruction, the (PET)SPECT, SPECT, and their corresponding CT data were coregistered and resampled to equivalent 200-μm voxel sizes. CT-based attenuation correction was applied. Reconstructed images were viewed and analyzed using PMOD v.3.37 (PMOD Technologies, Zurich, Switzerland). ^{111}In-citrate was produced as follows: 50 MBq of $^{111}InCl_3$ (Curium, UK) was incubated with 0.05M sodium citrate (Sigma-Aldrich, UK) in a total volume of 0.17 mL at 37°C for 1 h; pH was adjusted with 1M NaOH. ^{111}In-citrate (SPECT; 10.95 MBq) and ^{18}F-fluorodeoxyglucose (FDG, (PET)SPECT; 10.55 MBq) were coinjected through a cannula into the lateral tail vein, and data were acquired for 12 minutes (2 bed positions containing both kidneys; 21 frames of 35 seconds; injection during frame, 2/20, lasting for 2 frames; 0–1200 keV). Frames 16–21 were summed and reconstructed into 1 imaged (4 iterations). A CT image (scan details in Assessment of CT Compatibility) was acquired for anatomical referencing and to aid coregistration between CT, SPECT, (PET)SPECT, and DCE-MRI. Following CT, SPECT, and (PET)SPECT imaging, the cradle containing the mouse in situ was transferred to MRI for DCE-MRI (scan details in Assessment of MRI Compatibility). MR and CT images were aligned and overlaid using rigid-body registration. The resulting transformation matrix was used to overlay the SPECT and (PET)SPECT images onto the MR and CT images.

Further MR-CT-(PET)SPECT imaging has been performed using this heating system in several hundred mice undergoing study for other purposes.

RESULTS

Homeothermic Maintenance

Ambient room and magnet bore temperature was 19.3°C and 20.4°C, respectively, as measured with the fiber optic temperature probe.

For a set target temperature of 36.0°C, the core temperature equilibrated within 20 minutes and was maintained at 35.5°C ± 0.2°C in 8 CBA mice (Figure 2); the animals recovered quickly and without incident. The animal's initial heat loss upon induction of anesthesia recovered within 10 and 15 minutes for SPECT/(PET)SPECT/CT (Figure 2A) and MRI (Figure 2B), respectively. A stable core temperature of 35.6°C ± 0.1°C was reached for MRI when an additional heat load of high-duty-cycle scanning was applied (Figure 2B).

As the animals approached the target temperature of 36.0°C, the current delivered through the resistor was reduced by the PID to avoid any overheating. The PID also limited the maximum temperature of the upper surface of the cradle to ~37°C, even when the temperature controller is functioning continually at its maximum output. In addition, the thermal imaging camera showed a homogenous heat distribution along the cradle surface (Figure 1D).

MRI Compatibility

Spectral and imaging distortions resulting from the use of a current flow through the heater elements were not seen (Figures 3 and 4). The MR spectrum acquired from a PRESS voxel in a water gel phantom showed no line–shape distortions or frequency shifts attributable to the current flow through the heater (Figure 3A). A difference spectrum acquired with the heater turned on and off was compared with the spectrum acquired with the heater turned off; both are shown in Figure 3B. The latter spectrum is displayed in the absolute value mode, and the difference spectrum was magnified 10× to render the difference spectrum clearly. The spectra show that the current flowing through the heater has a negligible effect on the proton resonance frequency at distances exceeding 1.68 mm, the thickness of the cradle. We have not further tested the minimum operating distance at which distortions could occur. Similarly, no distortions attributable to the current were observed in the same water gel phantom in 2D FLASH imaging (Figure 3B), with the difference image showing negligible residual image intensity. In vivo imaging using respiratory-gated 2D FLASH (Figure 4A) and cardiorespiratory-gated 3D FLASH (Figure 4B) confirmed the gel phantom data as again no distortions attributable to the current flow were observed. In all cases, no differences were observed when the heater was turned off and turned on, which was further emphasized when the signal intensity was plotted against scan repetition (Figure 4C).

For a postmortem mouse with the heater pad in position, a 1.5-dB increase in reference pulse power was required. SNR for 5 × 5 voxel regions of interest positioned in the liver (centrally

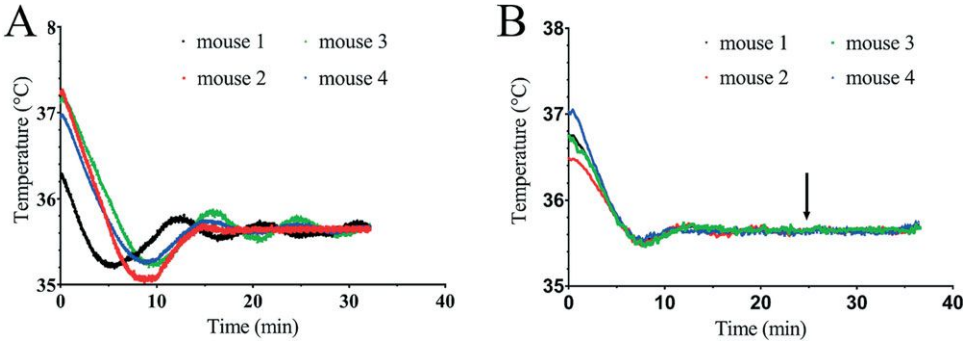

Figure 2. Homeothermic maintenance of core temperature in CBA mice using a carbon-fiber sheet resistor powered with high-frequency AC under PID control. The target rectal temperature was set to 36.0°C. Core temperature of 4 mice placed into the SPECT/(PET)SPECT/CT scanner (A). Core temperature of 4 mice placed into the MRI scanner (B). The arrow indicates when respiratory-gated balanced steady-state free-precession (bssfp) imaging was initiated to replicate the additional heat load of high-duty-cycle magnetic resonance imaging (MRI) scanning.

in the coil) and at the extreme edge of the z-FOV was reduced by ~20%, approximately in line with the increase in reference pulse power, as described elsewhere (6) (SNR = 12.52 and 10.25 for the absence and presence of the heater, respectively). The loss in SNR was a direct consequence of loading interactions with the tune/match circuits as the variable ranges of some of the tuning and matching capacitors were operated at their extremes. The size of the effect is dependent upon the exact position of the heater within the coil and its tune/match circuits and upon the size of both heater and coil.

CT Compatibility

Imaging distortions resulting from the presence of the carbon-fiber heater element were not seen (Figure 5B). The presence of the copper wire heater element produced severe image streaking (Figure 5A), organs were poorly defined, and CT intensities were poorly estimated.

Multimodal PET/SPECT/CT Imaging and MRI Imaging

A composite image formed from DCE-MRI, CT, ^{111}In SPECT, and ^{18}F (PET)SPECT is shown in Figure 6. The CT and MR images were used to drive the rigid-body registration.

Multimodal (PET)SPECT/SPECT/CT/DCE-MRI imaging was performed, and images could be easily coregistered, displayed, analyzed, and presented (Figure 6). The kidneys as rendered from the MRI image overlaid well with those rendered from the CT, (PET)SPECT, and SPECT images.

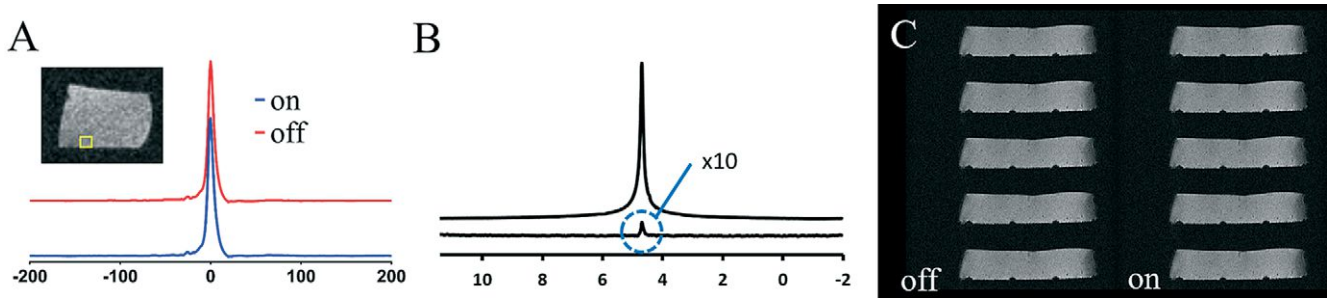

Figure 3. Impact of current flow through the carbon-fiber sheet heater element on MRI of a water gel phantom. PRESS pulse-acquire spectroscopy with the heater turned off and on (A). The image shows the placement of the 2-mm-cubic PRESS voxel that was located 3, 7, and 5 mm off-isocentre in the *z*, *y*, and *x* axes, respectively, such that it was positioned as close to one of the heater legs as possible; absolute value display of the spectrum showing the water resonance with the heater turned off (top trace) and the difference spectrum from acquisitions made with and without current flow through the heater (bottom trace) (B). The intensity of the difference spectrum is scaled 10× higher than the top trace and the absolute value display was used for clarity of display of the residual subtraction error. T1-weighted 2D FLASH MRI on a water gel phantom with the heater turned off (left column) and on (right column) (C).

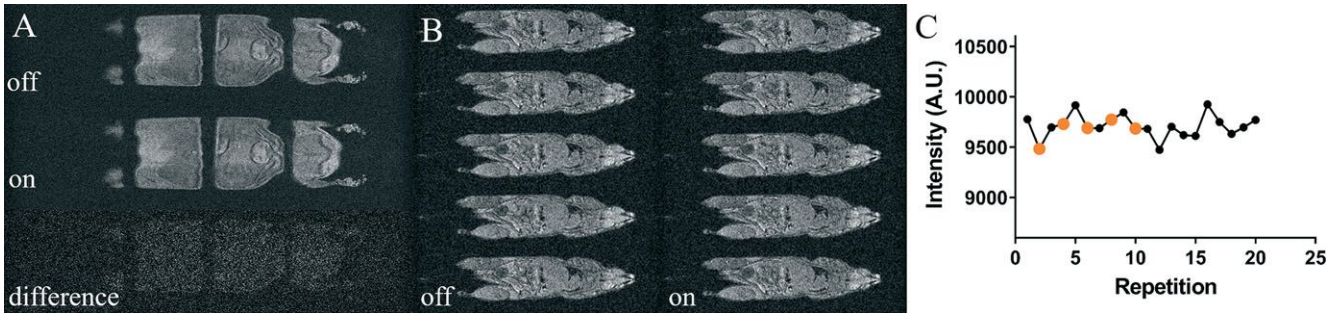

Figure 4. Impact of current flow through the carbon-fiber sheet heater element on in vivo MRI of the mouse. T1-weighted in vivo whole-body respiration-gated 2D FLASH MRI with the heater turned off (top) and on (middle) (A). The bottom image displays the difference image between both images. Cardiorespiratory-gated whole-body 3D FLASH MRI with the heater turned off (left column) and on (right column) (B). The average intensity over a square, placed close to the heater surface, was plotted for 20 repetitions with the heater turned on (black dots) or off (orange dots) (C).

DISCUSSION

The power dissipation of the carbon-fiber sheet heater allowed homeothermic maintenance of the animals. The maximum power delivery of ~2 W provided a maximum cradle temperature of ~37°C, thus avoiding any possibility of burns, and all animals recovered without incident. Animals entered the study with temperatures in the range of 36.3°–37.3°, presumably as a result of a different activity level ranges of the mice, local environment stability, and exact positioning of the rectal thermometer tip within the body. The homeothermic maintenance was performed using a custom-made PID-based temperature controller in conjunction with a standard commercial thermometer. This resulted in automated temperature maintenance for MR, (PET)SPECT/SPECT, and CT applications with a fluctuation of 0.1°C at ~0.5°C below the target temperature. Given that this heating system is used in imaging scanners that are both actively cooled and heated simultaneously, we accepted that this 0.5°C PID undershoot error was tolerable, especially as the temperatures were stable. The heat delivery, assessed with a thermal imaging camera (Figure 1D), was homogeneous when compared with that achieved with our previous versions of wire heater elements for which the wires ran markedly hotter than the average temperature of the heater pads (thermal images of the wire resistors not shown). Homeothermic control of the core temperature was shown, even in the presence of additional heat input from the scanner. The latter scan-induced heating can also be used to reduce the time necessary for the animal to recover from its initial heat loss following anesthetic induction.

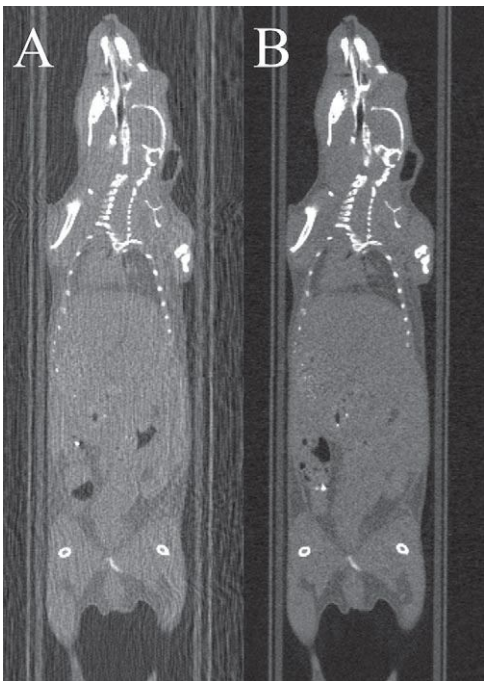

Figure 5. Impact of the heater material on computed tomography (CT) image quality. CT imaging using the 150-µm-diameter copper wire heater (A) or the carbon-fiber sheet heater (B). Streak artifacts owing to the presence of the heater are absent when using the carbon-fiber heater, and the image intensities remain intact.

MR compatibility of the AC-driven carbon-fiber heater was shown in localized spectroscopy and FLASH imaging (Figures 3 and 4). The equivalence of spectra and images acquired in the presence and absence of AC heating shows that the heater element delivers heat in a manner that does not corrupt the imaging process, and the carbon-fiber material does not lead to any marked image distortions.

CT-compatibility was shown in Figure 5. The absence of attenuation-derived streak artifacts provides good image quality that enables quantitative analysis of image intensities. This was not the case where the copper wire heater was used for which significantly streak artefacts were observed. As such, the carbon-fiber sheet heater performed favorably when compared with the copper wire heater.

Integration of the carbon-fiber heater into the imaging cradle was straightforward, and the low space requirement of

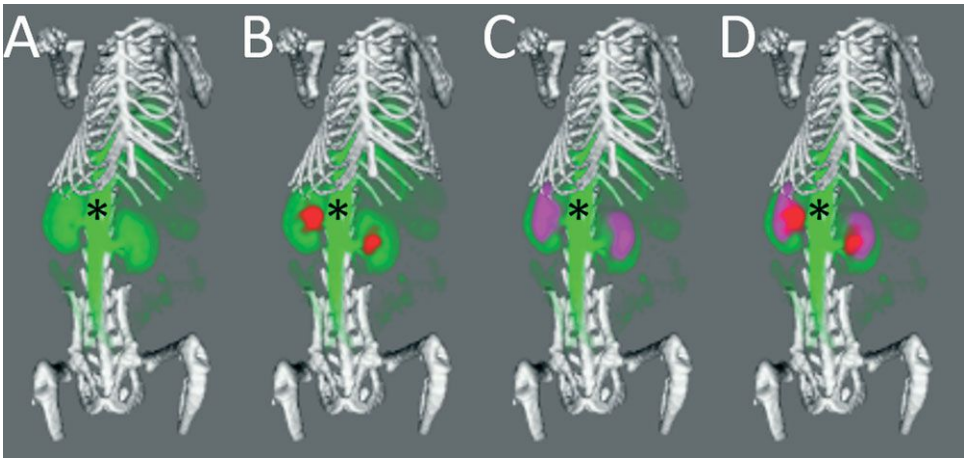

Figure 6. Multimodal imaging of a mouse using the carbon-fiber sheet–resistive heater embedded in a 3D-printed, flat-base, multimodal imaging cradle. The skeleton, kidneys, and major vessels to the kidneys (*) are marked up. The skeleton (white) was imaged by CT, while ^{111}In-citrate (red), ^{18}F-fluorodeoxyglucose (purple), and gadodiamide (green) were used for SPECT, (PET)SPECT, and DCE-MRI of the kidneys, respectively. Each panel shows an additional layer of the coregistered, segmented image: CT + MRI (A), CT + MRI + SPECT (B), CT + MRI + (PET)SPECT (C), CT + MRI + (PET)SPECT + SPECT (D).

the heater allowed the imaging to be performed in the smallest RF coil appropriate for whole-body imaging. The carbon-fiber heating element reduced SNR by ~15%–20%, equating to the use of an ~30-mm, rather than the 26-mm, diameter coil assuming that SNR is proportional to 1/coil volume (6). While the use of larger RF coils may allow temperature maintenance using circulating fluids in MRI, they are not necessarily an option in space-limited, small-bore collimators for PET and SPECT imaging, or when direct access to the animal is required. In such cases, the heating system described provides an elegant solution.

Moreover, by using CAD software in conjunction with a 3D plastic printer, it is very simple to design and deploy imaging cradles that feature integrated carbon-fiber heater elements. In our facility, we have produced many replicates of the heater element, which are then integrated into several different shapes and sizes of cradles, each of which has identical spaces and mounting points for the heater elements. The cradles also have integrated locating adaptors so that they can be easily positioned on scanners supplied by different manufacturers, each with their own bespoke mounting systems. Having performed the scans, the undistorted MR and CT images could be registered using a simple rigid-body registration. As the CT, SPECT, and (PET)SPECT images were generated within the same system, it was straightforward to overlay the SPECT and (PET)SPECT images onto the MR images and produce the composite image shown in Figure 6. This image shows, to a first approximation, blood volume from DCE-MRI, glucose distribution, and renal excretion to the bladder from FDG (PET)SPECT, renal excretion to the bladder of ^{111}In-citrate from SPECT, and anatomical definition of the skeleton from CT.

In conclusion, carbon-fiber sheet resistors powered with high-frequency AC allow homeothermic maintenance that is compatible with multimodality imaging using MR, CT, PET, and SPECT. The heater is small, and easy to produce, and integrate into cradles for multimodal imaging.

ACKNOWLEDGMENTS

Equal contribution: V.K. and S.G. contributed equally to this work.

We received funding from Cancer Research UK (Grant Number C5255/A12678), the CRUK/EPSRC Cancer Imaging Centre Oxford (Grant Number C2522/A10339), and the Medical Research Council (GB) (award to CRUK/MRC Oxford Institute for Radiation Oncology); the funders had no role in study design, data collection and analysis, decision to publish, or preparation of the manuscript.

We would like to acknowledge the Biomedical Sciences Unit team for the day-to-day welfare of the animals, the Mechanical Workshop Core group for production of the carbon-fiber heating elements, and the multimodal imaging cradle adaptors. Lastly, we wish to thank Fergus Gleeson and Paul Murphy at the Oxford University Hospitals NHS Foundation Trust for providing 18F-FDG.

Disclosures: No disclosures to report.

Conflict of Interest: The authors have no conflict of interest to declare.

REFERENCES

1. Kersemans V, Beech JS, Gilchrist S, Kinchesh P, Allen PD, Thompson J, Gomes AL, D'Costa Z, Bird L, Tullis IDC, Newman RG, Corroyer-Dulmont A, Falzone N, Azad A, Vallis KA, Sansom OJ, Muschel RJ, Vojnovic B, Hill MA, Fokas E, Smart SC. An efficient and robust MRI-guided radiotherapy planning approach for targeting abdominal organs and tumours in the mouse. PLoS One. 2017;12:e0176693.
2. Zhang M, Huang M, Le C, Zanzonico PB, Claus F, Kolbert KS, Martin K, Ling CC, Koutcher JA, Humm JL. Accuracy and reproducibility of tumor positioning during prolonged and multi-modality animal imaging studies. Phys Med Biol. 2008;53:5867–5882.
3. Thorek DL, Kramer RM, Chen Q, Jeong J, Lupu ME, Lee AM, Moynahan ME, Lowery M, Ulmert D, Zanzonico P, Deasy JO, Humm JL, Russell J. Reverse-contrast imaging and targeted radiation therapy of advanced pancreatic cancer models. Int J Radiat Oncol Biol Phys. 2015;93:444–4453.
4. Caro AC, Hankenson FC, Marx JO. Comparison of thermoregulatory devices used during anesthesia of C57BL/6 mice and correlations between body temperature and physiologic parameters. J Am Assoc Lab Anim Sci. 2013;52:577–583.
5. Torossian A, Ruehlmann S, Middeke M, Sessler DI, Lorenz W, Wulf HF, Bauhofer A. Mild preseptic hypothermia is detrimental in rats. Crit Care Med. 2004;32:1899–1903.
6. Doty FD, Entzminger G, Kulkarni J, Pamarthy K, Staab JP. Radio frequency coil technology for small-animal MRI. NMR Biomed. 2007;20:304–325.
7. Kersemans V, Gilchrist S, Allen PD, Beech JS, Kinchesh P, Vojnovic B, Smart SC. A resistive heating system for homeothermic maintenance in small animals. Magn Reson Imaging. 2015;33:847–851.
8. Vaissier PE, Beekman FJ, Goorden MC. Similarity-regulation of OS-EM for accelerated SPECT reconstruction. Phys Med Biol. 2016;61:4300–4315.
9. Slawson SE, Roman BB, Williams DS, Koretsky AP. Cardiac MRI of the normal and hypertrophied mouse heart. Magn Reson Med. 1998;39:980–987.
10. Schneider JE, Cassidy PJ, Lygate C, Tyler DJ, Wiesmann F, Grieve SM, Hulbert K, Clarke K, Neubauer S. Fast, high-resolution in vivo cine magnetic resonance imaging in normal and failing mouse hearts on a vertical 11.7 T system. J Magn Reson Imaging. 2003;18:691–701.
11. Barrett JF, Keat N. Artifacts in CT: recognition and avoidance. Radiographics. 2004;24:1679–1691.
12. Gilchrist S, Gomes AL, Kinchesh P, Kersemans V, Allen PD, Smart SC. An MRI-compatible high frequency AC resistive heating system for homeothermic maintenance in small animals. PLoS One. 2016;11:e0164920.
13. Kinchesh P, Allen P, Beech J, Fokas E, Gilchrist S, Kersemans V, Muschel R, Smart SC. editors. Dynamic reacquisition for respiratory gated, constant TR 2D multi-slice MRI. *23rd annual meeting International Society for Magnetic Resonance in Medicine 2015*. Toronto, Canada.
14. Schneider CA, Rasband WS, Eliceiri KW. NIH Image to ImageJ: 25 years of image analysis. Nat Methods. 2012;9:671–675.
15. Kinchesh P, Gilchrist S, Beech JS, Gomes AL, Kersemans V, Newman RG, Vojnovic B, Allen PD, Brady M, Muschel RJ, Smart SC. Prospective gating control for highly efficient cardio-respiratory synchronised short and constant TR MRI in the mouse. Magn Reson Imaging. 2018;53:20–27.

Publish today in Tomography

Scope

Tomography publishes basic (technical and pre-clinical) and clinical scientific articles which involve the advancement of imaging technologies. Tomography encompasses studies that use single or multiple imaging modalities including for example CT, US, PET, SPECT, MR and hyperpolarization technologies, as well as optical modalities (i.e. bioluminescence, photoacoustic, endomicroscopy, fiber optic imaging and optical computed tomography) in basic sciences, engineering, preclinical and clinical medicine. Studies involving hardware and software advances along with chemical and molecular probe developments are also of high interest for publication in Tomography.

Submission

Submission of manuscripts can be accomplished through the web site www.Tomography.org using our online submission system.

Open Access Compliance

Funding Agencies and Article Repositories

Certain funders, including the NIH, members of the Research Councils UK (RCUK), and Wellcome Trust require deposit of the Accepted Version in a repository after an embargo period. Tomography allows all of its authors to deposit their articles on such repositories immediately upon publication.

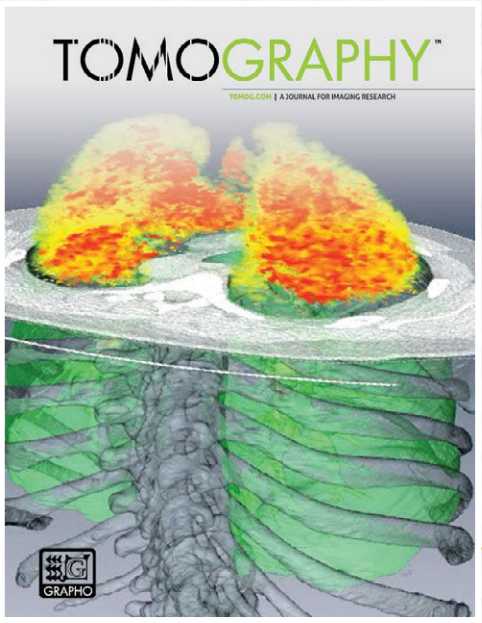

Instructions for Authors

Research Articles

Original studies considered for publication will provide the field of imaging with significant advances in basic, preclinical, clinical, hardware and software using single or multi-modal imaging technologies. In addition, studies that use imaging technologies to advance basic and clinical medicine through interrogation of biological and pathological processes are also of interest.

Advances in Brief

Advances in Brief are timely high impact contributions on a topic important to imaging researchers. These Advances will undergo an accelerated review process. Papers submitted as Advances in Brief may combine the Results and Discussion sections.

Reviews

Tomography will publish Reviews which are timely and important to imaging researchers. Reviews should be written as concisely as possible. All Review articles will be subject to peer review. The parameters for this category are provide below but serve only as guidelines as longer reviews will be considered if the topic warrants additional space in the journal.

Perspectives

Tomography will publish Perspectives which are used to present new insights on an active or emerging area of imaging research or application of imaging technologies in the preclinical or clinical setting along with the author's personal viewpoint on the area including unresolved areas for future research along with key issues facing development and/or deployment.

Image Reports

Image Reports are discrete Reports (approximately 1,500 words) that provide significant advances and offer unique insights into the application of imaging technologies for the further advancement of preclinical or clinical diagnosis or treatment response. No specific limits are place on overall numbers of figures or tables but up to 4 would be reasonable.

Consensus Papers

Papers which provide a broad consensus on a timely topic related to imaging which is sponsored from investigators participating at a national meeting or meeting sponsored by a government funding agency. Authors are encouraged to contact the editorial office prior to submission.

TOMOGRAPHY®

AN INTERNATIONAL JOURNAL FOR IMAGING RESEARCH

gehealthcare.com

SIGNA™ Returns.

For more than 30 years, SIGNA has stood for quality, trust, and innovation. This year, SIGNA Returns with the introduction of a family of new products that bring you the trusted performance you've relied on for over three decades, plus powerful forward-thinking technologies to help enhance your clinical confidence.

Visit gehealthcare.com for more information.

BRUKER

Welcome to the World of Preclinical Imaging

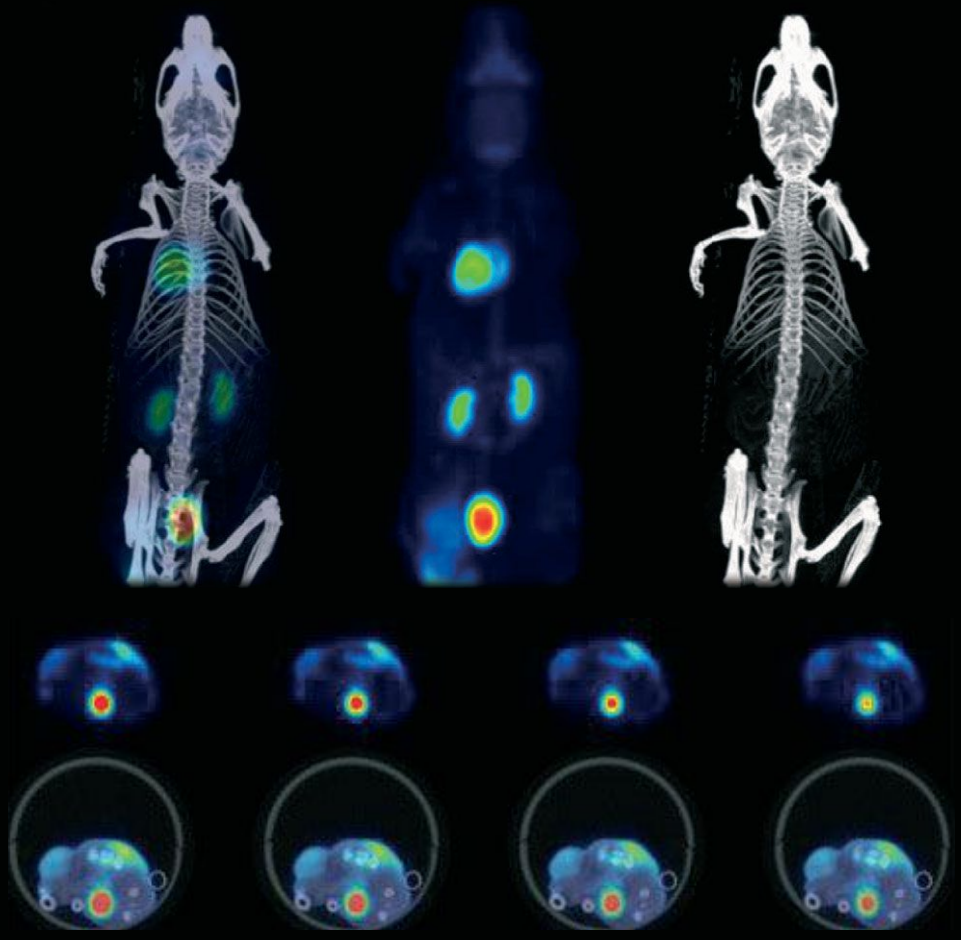

Finest Detail in Every Organ

Accurate Quantification

Low Dose Fat Scan Times

Total Body FOV 80x200mm

- Introducing the PET/CT Si78 high performance PET and CT
- Total body PET for mice and rats
- Powered by ParaVision 360
- Simplified workflow
- Supports a wide range of applications

Discover more at: www.bruker.com/pci

Innovation with Integrity